A microfluidic sensing system for simultaneous monitoring of extracellular Ca(II) and insulin secretion

By

Weikun Huang

THE UNIVERSITY of ADELAIDE

A thesis submitted for the degree of

Master of Philosophy

Faculty of Science

School of Physical Sciences

July, 2019

Declaration of Authorship

I certify that this work contains no material which has been accepted for the award of any other degree or diploma in my name, in any university or other tertiary institution and, to the best of my knowledge and belief, contains no material previously published or written by another person, except where due reference has been made in the text. In addition, I certify that no part of this work will, in the future, be used in a submission in my name, for any other degree or diploma in any university or other tertiary institution without the prior approval of the University of Adelaide and where applicable, any partner institution responsible for the joint-award of this degree.

I give permission for the digital version of my thesis to be made available on the web, via the University's digital research repository, the Library Search and also through web search engines, unless permission has been granted by the University to restrict access for a period of time.

Signed: _____

Date: _____

Table of Contents

Abstract

Extracellular Ca^{2+} ($[Ca^{2+}]_{ex}$) is increasingly recognised as an important messenger for intercellular communications. Recent evidence suggests that $[Ca^{2+}]_{ex}$ plays a critical role in mediating the pulsatile insulin secretion from the pancreatic β cells, the impairment of which often represents an early pathological defect in the development of type 2 diabetes mellitus (T2DM). The underlying mechanisms for the latter remain to be elucidated, but are constrained by the lack of sensors suitable for the measurement of $[Ca^{2+}]_{ex}$ in the extracellular environment. To enable the investigation on dynamic $[Ca^{2+}]_{ex}$ and insulin secretion, two fluorescent indicators, Calcein and Rhodamine-5N (Rhod-5N), were systematically evaluated for measuring $[Ca^{2+}]_{ex}$. Under the optimised conditions, both of the two indicators showed robust fluorescent signals and high selectivity to $[Ca^{2+}]_{ex}$. Compared with previous studies, the fluorescence-based methods established for $[Ca^{2+}]_{ex}$ in this thesis are easily accessible and inexpensive. Polydimethylsiloxane (PDMS) chip was then designed, fabricated and characterised to be capable of immobilising the biological tissues and manipulating their extracellular environment. Subsequently, a microfluidic sensing system was developed by integrating the optimised fluorescent indicator, microfluidic chip, laser-induced fluorescence (LIF) detection system and enzyme-linked immunosorbent assay (ELISA). The microfluidic sensing system, for the first time, enabled the simultaneous monitoring of the dynamic $[Ca^{2+}]_{ex}$ and insulin concentrations in biological samples. The sensing system presented in this work can be used as a novel tool to gain fundamental insights as to how $[Ca^{2+}]_{ex}$ is involved in the regulation of the pulsatile insulin secretion in both health and T2DM. The future work in this area may identify novel therapeutic targets for the prevention and treatment of T2DM.

Acknowledgements

This thesis represents the scientific work that I have accomplished in the last two years and marks my journey of transition from studies in molecular biology into a multi-disciplinary research programme. It would not have been possible without the support and encouragement I have received from many people.

First of all, I would like to sincerely thank my supervisors Professor Heike Ebendorff-Heidepriem, and Dr. Jiangbo (Tim) Zhao and Dr. Tongzhi Wu for their constant advice and encouragement. My training has benefited from their complementary expertise in photonics, fundamental physics and medical science, which made the project possible. With their guidance, I have developed solid skills to identify and address essential biological questions. Their passion and dedication to science also stimulated my interests in pursuing an academic career in the future.

I gratefully acknowledge my collaborators Dr. Alliaa Shallan and Associate Professor Craig Priest in the Future Industries Institute, the University of South Australia, for their valuable support on the chip design and fabrication.

My gratitude extends to the members in fibre fabrication and sensing group, particularly Dr. Roman Kostecki for assisting me to set up the fluorescence sensing system, Dr. Yinlan Ruan for technical support in measuring fluorescence. I am also grateful for the friendship and support from my fellow co-workers, Mr. Yunle Wei, Mr. Xuanzhao Pan and Ms. Mengke Han.

I would also like to thank the Australian National Fabrication Facility (ANFF) staff at the University of Adelaide. Special mention goes to Mr. Evan Johnson for fabricating the aluminium frame and Mr. Alson Kwun Leung Ng for technical support. Many thanks to the ANFF South Australia node for hosting the Microengineering Winter School, which extended my knowledge in the area of microfluidics.

Finally and most importantly, I would like to express my deepest gratitude to my mother Yanfang Zhang. It was her unconditional love and trust that allowed me to realise my dream to study overseas. I would also like to appreciate the support from my sister Jing Huang and her husband Lu Qi. It has been my greatest fortune to have them in my life.

Abbreviations

T2DM – type 2 diabetes mellitus

$[Ca^{2+}]_{ex}$ – extracellular Ca^{2+} concentration

PDMS – polydimethylsiloxane

LIF – laser-induced fluorescence

ELISA – enzyme-linked immunosorbent assay

ATP – adenosine triphosphate

K_{ATP} channel – ATP-sensitive potassium channel

VGCC – voltage-gated Ca^{2+} channel

VDCC – voltage-dependent Ca^{2+} channel

$[Ca^{2+}]$ – Ca^{2+} concentration

$[Ca^{2+}]_c$ – cytosolic Ca^{2+} concentration

GSIS – glucose-stimulated insulin secretion

GLUT – glucose transporter

Mito – mitochondria

MCU – mitochondrial Ca^{2+} uniporter

TCA cycle – tricarboxylic acid cycle

IP_3R – inositol 1, 4, 5 trisphosphate receptor

ER – endoplasmic reticulum

SECRA – sacro-endoplasmic reticulum Ca^{2+}-ATPase

CaSR – Ca^{2+}-sensing receptor

MMP – mitochondrial membrane potential

$[Ca^{2+}]_{mito}$ – mitochondrial Ca^{2+} concentration

$[Ca^{2+}]_{ER}$ – endoplasmic reticulum Ca^{2+} concentration

GJ – gap conjunction

Aeq – aequorin

PET – photo-induced electron transfer

ICT – internal charge transfer

FRET – Förster resonance energy transfer

K_d – dissociation constant

HOMO – highest occupied molecular orbital

LUMO – lowest unoccupied molecular orbital

cAMP – cyclic adenosine monophosphate

AM – acetoxymethyl

GECI – genetically encoded Ca^{2+} indicator

GFP – green fluorescent protein

BRET – bioluminescence resonance energy transfer

YFP – yellow fluorescent protein

CaM – Ca^{2+}-binding peptide calmodulin

ISM – ion-selective microelectrode

CSM – Ca^{2+}-selective microelectrode

PI – pseudoislet

MPS – microfluidic perfusion system

CEI – capillary electrophoresis immunoassay

GLP-1 – glucagon-like peptide-1

BAPTA – 1, 2- bis(o-aminophenoxy)ethane-N, N, N', N'-tetraacetic acid

TPE – tetraphenylethene

PAA – polyacrylic acid (PAA)

BODIPY – boron-dipyrromethene

PBS – phosphate-buffered saline (PBS)

DI – deionised

DMEM – Dulbecco's modified eagle medium

Re – Reynolds number

CAD – computer-aided design

CFD – computational fluid dynamic

PE – polyethylene

FITC-insulin – isothiocyanate-labelled insulin

Ab – antibody

BSA – bovine serum albumin

OD – optical density

Symbols

λ – wavelength

F – fluorescence intensity

Qu – quencher

n – the number of the bound indicator molecule

γ_i – the activity coefficient

φ – proportionality factor

ε – dielectric constant

z_i – the valence of an ion

I – ionic strength

K_{SV} – Stern-Volmer quenching constant

T – temperature

ρ – the mass density of the fluid

v – the average flow velocity

D_h – the hydraulic diameter of a channel

μ – the viscosity of the fluid

A – the area of a cross-section of a channel

U – the wetted perimeter of a channel

d – the travelling distance of molecules

D – diffusion coefficient

t – the travelling time of molecules

k – Boltzmann constant

R_C – radius of the cross-section shape of a channel

r – the hydrodynamic radius of molecules

w – the width of a channel

h – the height of a channel

τ – the required mixing time for two co-flow solution

Q – the volumetric flow rate

L – the channel length

V – volume

List of Figures

List of Tables

Chapter 1

The roles of Ca^{2+} in insulin secretion and the development of Ca^{2+} sensors for pancreatic islet study

There is compelling evidence showing that both intracellular and extracellular Ca^{2+} signallings are coupled to insulin release from the pancreatic β cells, and are likely to be involved in the pathogenesis of β cell dysfunction and the progression of T2DM. Understanding of Ca^{2+} dynamics in relation to the endocrine function of the pancreatic islets has been predominantly facilitated by the development of Ca^{2+} sensing techniques and novel platforms (e.g. microfluidic devices). This chapter provides a comprehensive overview of the current understanding on: 1) the role of Ca^{2+} signalling in insulin secretion and the development of Ca^{2+} sensors for pancreatic islet study; 2) knowledge gaps in the understanding of the role of Ca^{2+} in insulin secretion; 3) the critical capabilities of Ca^{2+} sensors necessary for this area of research; 4) the rationale for the development of a sensing platform for simultaneous monitoring of Ca^{2+} and insulin.

1.1 Background

Diabetes is one of the most prevalent chronic diseases worldwide, affecting more than 400 million people in 2014 (about 8.5 % of the adult population) [1] and resulting in over 827 billion USD direct medical expenditure [2]. Over 90% of diabetes patients suffer from T2DM, which is commonly characterised as relative or absolute insufficiency of insulin secretion from the pancreatic β cells in the context of insulin resistance and, therefore, the elevation of blood glucose concentrations. Accordingly, tremendous efforts have been put into the understanding of the mechanism(s) underlying insulin secretion [3-5].

Among various regulatory factors, Ca^{2+} has been reported to account for both initial fast insulin release from the stored insulin granules within the β cells and the late-phase insulin synthesis and secretion [6]. To this end, a number of tools have been developed for recording the dynamic changes of intracellular Ca^{2+}. However, few sensing methods are established to monitor the $[Ca^{2+}]_{ex}$, which is likely to mediate intercellular communications and synchronising the secretive activity of individual β cells [7,8]. Accordingly, development of a tool capable of simultaneous monitoring of $[Ca^{2+}]_{ex}$ and insulin secretion from the pancreatic islets represents a critical step for improved understanding of insulin secretion in health and T2DM.

1.2 Roles of Ca^{2+} signalling in insulin secretion

Pancreatic islet, also known as the islet of Langerhans, is a group of organised endocrine cells (hormone-producing cells) in the pancreas, which contains approximately 10^6 islets [9]. A pancreatic islet typically consists of three major endocrine cells, α cells (20%), β cells (70%) and δ cells (<10%), secreting glucagon, insulin and somatostatin respectively. As shown in Fig. 1.1a & b, the cellular distributions and ratios of these endocrine cells differ substantially between mice and human. β cells are typically condensed around the core of a mouse islet (Fig. 1.1b), while they are distributed globally within a human islet (Fig. 1.1a) [10,11]. Although the differences in cellular distributions are substantial, pancreatic islets of different species exhibit a similar low level of basal insulin secretion at non-stimulatory blood glucose levels (< 3mM in human, < 6mM in mouse) and the stimulated insulin secretion as the glucose level increases [3]. Moreover, insulin secretions recorded from either isolated islets or from the peripheral circulation in humans, mice and dogs are pulsatile [12-20], with a typical frequency of ~5 minutes per pulse (Fig. 1.1e) [21]. That the *in vivo* insulin curve pattern (corrected for amplitude) is coherent to that of the *in vitro* secretory bursts from individual islets suggests that the *in vivo* pulse is a reflection of coordinated secretion of insulin from different islets [22]. Of note, the pulsatility of plasma insulin is diminished in patients with T2DM and their first-degree relatives [23-25]. The latter suggests that impaired pulsatility of insulin release may predispose to any substantial loss of β cells function in T2DM. Accordingly, the understanding of the mechanism(s) underlying the pulsatile secretion pattern of insulin and its impairment in patients with T2DM or individuals with high risks is of major clinical relevance to both the prevention and the intervention of this metabolic disorder.

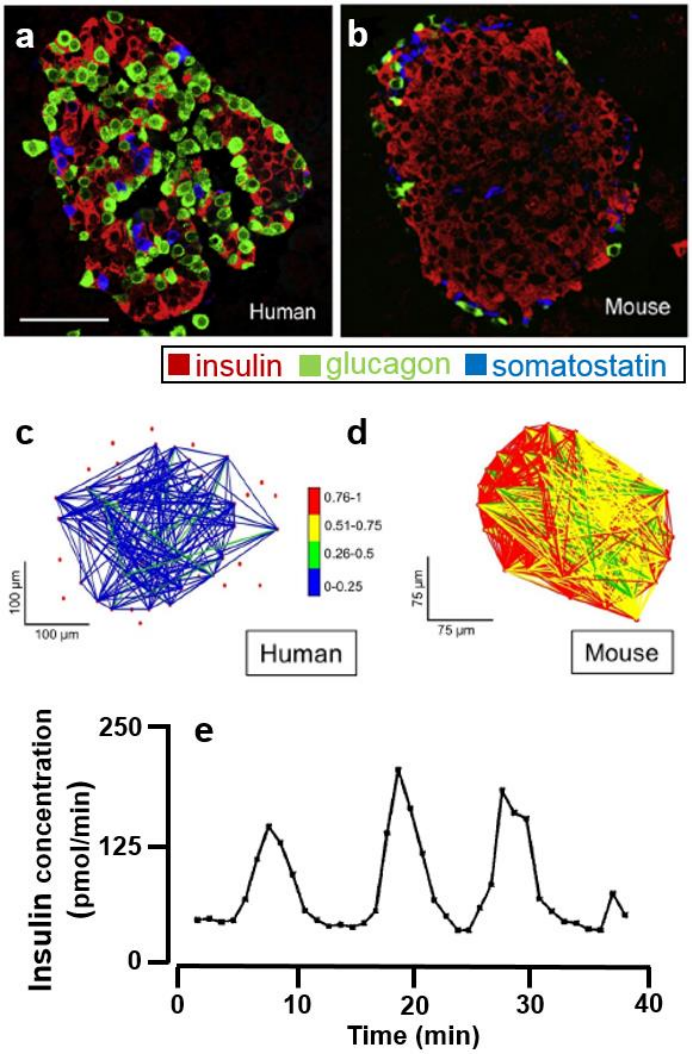

Figure 1.1 | The structural differences of pancreatic islets and the common pulsatility of insulin secretion observed in different species. a & b | Confocal images of pancreatic islets from a human and a mouse with immunostained for insulin (red), glucagon (green) and somatostatin (blue). (Scale bar = 50µm) [11]**; c & d** | Functional connectivity (FC) map indicating the distribution and connection strength of correlated β cells in an intact human and mouse islet during glucose stimulation. (Colour bar: 0 – 0.25 [blue] = lowest, 0.76 – 1 [red] = highest) [26]; **e |** The representative insulin releases pattern indicated by the insulin concentration in the circulating system with a frequency of 4~6mins in mammals [22].

1.2.1 Intracellular Ca^{2+} signalling: a trigger of insulin secretion

The secretion of insulin from pancreatic islets is coupled with glucose metabolism (i.e. the production of adenosine triphosphate, ATP), electrical excitation and intracellular Ca^{2+} signalling (Fig. 1.2). When blood glucose reaches stimulatory concentration, the increased ATP production in β cells leads to the closure of ATP-sensitive potassium channel (K_{ATP} channel)

[27,28], which causes the reduction of the hyperpolarizing K_{ATP} current and induces a depolarizing current [29,30]. The latter subsequently gives rise to the opening of voltage-gated Ca^{2+} channels (VGCC, also known as voltage-dependent Ca^{2+} channel, VDCC) [31]. The influx of Ca^{2+} triggers the firing of action potential (at -50mV) and the fusion of insulin-containing granules with membrane for exocytosis [32]. It is noteworthy that the secretion of insulin in response to an intravenous glucose challenge usually consists of two distinctive phases, an initial rapid phase (first phase) and subsequently slower and stable phase (second phase) [33]. The first phase secretion is predominantly accounted for the readily release pool from the granules [31], while the second phase secretion results from the continuous insulin production in the β cells.

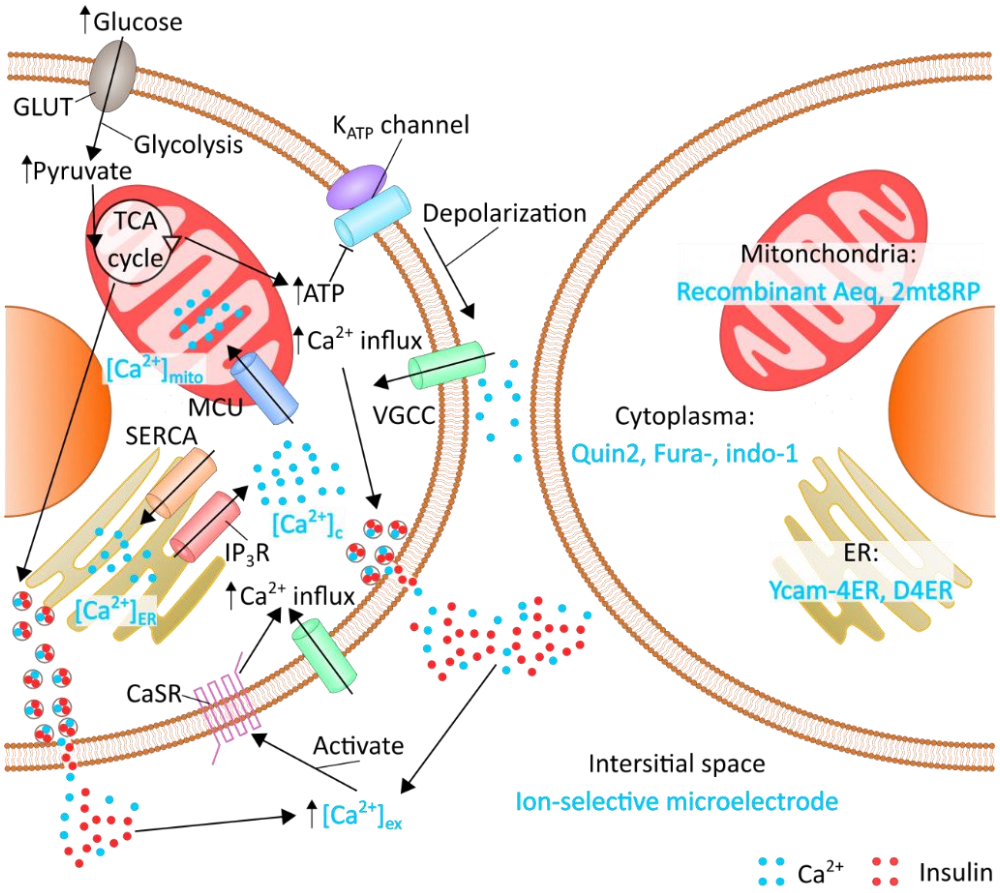

Figure 1.2 | The Ca^{2+} signalling pathways in insulin secretion (*left*) identified by various Ca^{2+} probes in islet study (*right*). *Left* | Ca^{2+} signalling involved in glucose-stimulated insulin secretion (GSIS). The transport pathway of Ca^{2+} is indicated with black arrows. Abbreviation: GLUT, glucose transporter; Mito: mitochondria; MCU, mitochondrial Ca^{2+} uniporter; TCA cycle, tricarboxylic acid cycle; IP_3R inositol 1,4,5 trisphosphate receptor; ER: endoplasmic reticulum; SERCAs, sacro-endoplasmic reticulum Ca^{2+}-ATPases. CaSR, Ca^{2+}-sensing receptor. ***Right*** **|** Ca^{2+} probes used in islet study for identifying and monitoring the corresponding cellular compartment. Blue text: Ca^{2+} in varying compartments and corresponding probes for different Ca^{2+}.

During the second phase, insulin is typically secreted in the pulsatile pattern [13,34]. While the mechanism(s) underlying this phenomenon has not been fully understood, the intracellularly distributed Ca^{2+} has been regarded as the major driving factor, including cytoplasmic Ca^{2+} ($[Ca^{2+}]_c$), mitochondrial Ca^{2+} ($[Ca^{2+}]_{mito}$) and endoplasmic reticulum Ca^{2+} ($[Ca^{2+}]_{ER}$) [33,35,36]. The $[Ca^{2+}]_c$ directly facilitates the fusion of insulin-containing granule with the cell membrane. As a result, $[Ca^{2+}]_c$ in the β cells have been observed to oscillate in parallel with the secretion of insulin from the isolated islet of mice and humans [37-40]. Moreover, limiting the rises in $[Ca^{2+}]_c$ by removing extracellular Ca^{2+} or blocking the VGCC attenuates the glucose-stimulated insulin secretion (GSIS) [41], further suggesting the direct effect of $[Ca^{2+}]_c$ on GSIS.

$[Ca^{2+}]_{mito}$ and $[Ca^{2+}]_{ER}$ also oscillate in pace with $[Ca^{2+}]_c$ during GSIS [42-46] and participate in the regulation of insulin secretion by modulating the ATP production and $[Ca^{2+}]_c$, respectively. In response to glucose stimulation, when $[Ca^{2+}]_c$ increases, the mitochondria stores more Ca^{2+} through the mitochondrial Ca^{2+} uniporter (MCU) [44,47]. The increased $[Ca^{2+}]_{mito}$ facilitates the production of ATP [48-51], which provides energy for insulin synthesis and secretion. It has been shown that silencing MCU by utilising small interference RNA [52] or buffering the Ca^{2+} in the mitochondrial matrix space [53] attenuates insulin secretion at the second phase [54,55]. Meanwhile, endoplasmic reticulum (ER) recruits Ca^{2+} through sacro-endoplasmic reticulum Ca^{2+}-ATPases (SERCAs) [56,57], followed by a slow release of Ca^{2+} at end of the oscillatory period. As a result, silencing *SERCA3* or blocking SERCA channels gives rise to amplified $[Ca^{2+}]_c$ oscillation and (hence) insulin secretion [56,58].

By applying fluorescent Ca^{2+} probes, the dynamic variations of $[Ca^{2+}]$ in each compartment of β cells have been successfully tracked from glycolysis to insulin secretion. However, the observations hitherto have not identified the intrinsic pacemaker for glucose-induced $[Ca^{2+}]$ oscillation. Likewise, it remains unclear as to the relative importance of each component to the maintenance of β cell function. Nonetheless, the virtually identical insulin secretory pattern from purified β cells, isolated islets, and the whole endocrine pancreas suggests effective communication within and between the islets for synchronising the secretion of insulin.

1.2.2 Extracellular Ca^{2+} signalling: an integrator of secretion

Due to the differences in cellular distribution and composition, the mechanisms underlying the intercellular communication would intuitively be expected to vary between mice and human islets. In mice, β cells are electrically connected by gap conjunctions (GJs), which spread the membrane depolarisation and thereby transmit the stimulatory signals between the neighbouring β cells for the synchronised secretion action [59]. In this way, β cells in mice islets display a high strength of correlation during GSIS (Fig. 1.1d). The disruption of GJs impairs both synchronised $[Ca^{2+}]_c$ oscillation and glucose-induced pulsatile insulin secretion [60,61]. As discussed above, the mechanism of GJs in mice predominantly influences adjacent β cells. By contrast, human islets have a much weaker cellular network (Fig. 1.1c), such that the function of GJs would be limited or ineffective. In humans, the diffusible factors, including extracellular Ca^{2+}, neurotransmitter [62], intra-islet hormones and gut-derived incretin hormones [26], are often considered for intra- and inter-islet communication and coordination.

$[Ca^{2+}]_{ex}$ is recently reported to mediate intercellular communication through the extracellular Ca^{2+}-sensing receptor (CaSR) [63]. CaSR was initially found to be the regulator for serum Ca^{2+} concentrations in the body. When the $[Ca^{2+}]_{ex}$ fluctuates in the local environment, CaSR senses the local $[Ca^{2+}]$ and regulates parathyroid hormone secretion to adjust serum Ca^{2+} concentrations [64]. More recently, the CaSR sensing pathway has been suggested to account for intercellular communication [63]. In an *ex vivo* model, Hofer, M. A. et al. co-cultured non-CaSR-expressing BHK-21 cells as 'donors' with CaSR-expressing HEK293 cells (HEK-CaSR) ('sensor'). They observed that the agonist-induced $[Ca^{2+}]_c$ changes in the 'donor' cells generated a Ca^{2+} extrusion, which could be detected by the nearby 'sensor' cells and further triggered the alterations in $[Ca^{2+}]_c$ of 'sensor' cells. This propagation of $[Ca^{2+}]_c$ signal is CaSR-dependent, indicating the intercellular communication could be achieved by local $[Ca^{2+}]_{ex}$-activating CaSR [65]. Accordingly, by using the specific fluorescent probe, a rise of local $[Ca^{2+}]_{ex}$ was observed when CaSR was activated. The rise in $[Ca^{2+}]_{ex}$ could further activate the CaSR expressed on the neighbouring cells [66].

As the Ca^{2+} is co-released with insulin from the secreting-granules, $[Ca^{2+}]_{ex}$ in the intercellular space has been shown to increase in response to glucose stimulation [67]. Activation of CaSR by Ca^{2+} (e.g. 10 mM) increases the insulin secretion from both MIN6 pseudoislets [68] and human islets [69] – such effect attenuated when $[Ca^{2+}]_{ex}$ is removed [69]. Moreover, stimulating insulin secretion through this pathway can be independent of glucose, leading to the secretion of

insulin from the cells that have not been exposed to glucose. In addition, activation of CaSR up-regulates the expression of VGCCs, which could further augment the GSIS [70]. Given the abundant expression of CaSR on both mouse and human β cells [68,71,72], the CaSR-signalling pathway has been proposed to coordinate insulin secretion within islets [73], where $[Ca^{2+}]_{ex}$ might serve as a potential synchroniser of insulin secretion [74]. However, due to the lack of an effective sensing tool for tracking $[Ca^{2+}]_{ex}$, it remains unclear on how $[Ca^{2+}]_{ex}$ changes in the interstitial fluid and whether it indeed synchronises the pulsatile insulin secretion in intact human islets.

1.3 Development of Ca^{2+} sensing techniques in secretion analysis

The study concerning the roles of Ca^{2+} in insulin secretion can be dated back to 1966, when the presence of Ca^{2+} in the extracellular environment was recognised as a prerequisite for insulin secretion from the pancreatic β cells [75]. In the next year, the luminescent protein aequorin (Aeq) isolated from jellyfish was firstly reported to reliably record the fluctuations of intracellular Ca^{2+} [76]. The last 50 years have witnessed a rapid evolution of Ca^{2+} sensing techniques and how they have advanced the understanding of Ca^{2+} signalling in the biology of pancreatic islets. The timeline below summarises the milestone events relating to the development of advanced sensing techniques (including the emergence of both new-generation sensors and functional sensing platforms) and the progressive understanding of Ca^{2+} signalling pathways underlying insulin secretion.

Timeline--Milestones on Ca^{2+} sensing and insulin secretion study

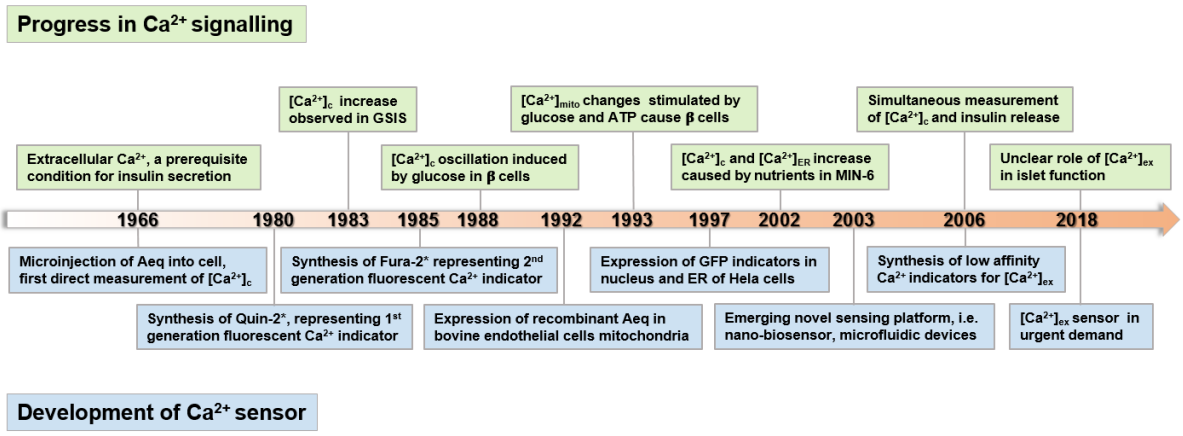

(* refers to one selected example in reported serial indicators)

1.3.1 Synthetic fluorescent Ca^{2+} indicators

With a large available tool library, synthetic fluorescent Ca^{2+} indicators are currently the most widely used Ca^{2+} sensing tools in islet study (selected indicators for islet study are summarised in Table 1.1). These Ca^{2+} indicators typically consist of three components: fluorophore, Ca^{2+} chelator and linker. While the fluorophore accounts for the changes in fluorescent signals, the Ca^{2+} chelator recognises and interact with Ca^{2+} and, therefore, determines the sensitivity and selectivity of the indicators. To reflect the change in Ca^{2+} concentration ($[Ca^{2+}]$), the interaction between Ca^{2+} and chelator induces the changes of fluorescent signals of the fluorophore in response to the fluctuation of $[Ca^{2+}]$. In terms of ion indicators, there are generally four mechanisms underlying the fluorescent processes, including photo-induced electron transfer (PET), internal charge transfer (ICT), formation or disappearance of excimer and Förster resonance energy transfer (FRET) [77]. This section focuses on PET and ICT (FRET in the next section), as these mechanisms are predominantly used to develop fluorescent Ca^{2+} probes.

In the processes of PET and ICT, the Ca^{2+} binding-induced electron movement is the key trigger of the fluorescent signal switch. For PET-based off-on indicators, the electron-rich chelator is spatially separated from the fluorophore by a linker (on-off PET indicator is not commonly used in Ca^{2+} sensing, details can be found in another review [78]). On excitation of the fluorophore, an electron of the highest occupied molecular orbital (HOMO) is excited to the lowest unoccupied molecular orbital (LUMO). The PET from the Ca^{2+}-free chelator competes with the relaxation of the excited electron of the fluorophore and therefore quenches the fluorescence intensity of the excited fluorophore (Fig. 1.3a, i). When bound to Ca^{2+}, the redox potential of the chelator increases, leading to lower HOMO energy (less likely to remove an electron from the orbital). Thus, PET-induced fluorescence quenching is inhibited and the Ca^{2+} concentration will be indicated by the enhancement of the fluorescence intensity (Fig. 1.3a, ii). For example, when excited by at 488nm, Fluo-3 display significant fluorescence enhancement in response to increasing $[Ca^{2+}]$ at around 525nm (Fig. 1.3a, iii) [79].

Table 1.1 | Fluorescent Ca^{2+} indicators for cytosolic calcium in β cells and islets

Indicator	Subject	K_d	Absorption wavelength, nm		Emission wavelength, nm		F_{max}/F_{min} (R_{max}/R_{min})	Note	Reference
			Ca^{2+} free	Ca^{2+} bound	Ca^{2+} free	Ca^{2+} bound			
Quin-2	1, 6	60nM	355	330	495	495	5-8	a.	[80,81]
Fura-2	1, 2, 3, 4	224nM	363	335	510	505	(13-25)	b.	[36,38,82-85]
Indo-1	2	230nM	346	330	475	400	(20-80)	c.	[86]
Fura-PE3	2	250nM	364	334	508	500	(18)	d.	[87,88]
Fluo-3	4	390nM	503	506	525	525	40-100	e.	[89]
Fura-red	1,2, 4, 5	140nM	470	435	660	660	(5-12)	f.	[90-92]

Apart from the journal references given in the table, the data above is also referred to *The Handbook: A Guide to Fluorescent Probes and Labeling Technologies* (11 ed.) by Molecular Probes™ [79]. K_d, the dissociation constant of indicator; Ca^{2+} free, no Ca^{2+}; Ca^{2+} bound, binding occurred between indicator and Ca^{2+}; F_{max}/F_{min}, the ratio of maximum fluorescence to minimum fluorescence of indicator; R_{max}/R_{min}, the ratio of maximum fluorescence ratio to minimum fluorescence ratio

Subjects: 1. Isolated mouse β cells

2. Intact mouse islet
3. Isolated human β cells
4. Intact human islet
5. MIN6 β cells (highly differentiated and glucose-responsive murine β cell line) [93]
6. Clonal insulin-releasing cell line RINm5F

Note: a. Quin-2: The first generation of fluorescent Ca^{2+} indicators. Both the absorption coefficient and the quantum efficiency are relatively low for Quin-2 in comparison to later developed fluorescent indicators [94,95].

b. Fura-2: A ratiometric indicator by dual-excitation (340/380nm). High compartmentalisation and strong binding to proteins.

c. Indo-1: A ratiometric indicator with dual emissions (405/485nm) and high affinities for Zn^{2+} and Mg^{2+}. [86]

d. Fura-PE3: Derivative of Fura-2, designed for leakage resistance from the cytoplasm, high Ca^{2+}-induced fluorescence change.

e. Fluo-3: Enhanced fluorescence with visible excitation light [89].

f. Fura-red: A ratiometric measurement by dual-excitation (420/480nm). A long emission wavelength in the red spectrum, compatible with other ion-sensitive fluorescent indicators for multiplexing measurement.

Unlike the three components of the PET sensing system, where the electron donor and acceptor are charged-separated, the electron transfer in the ICT-based indicators occurs within an integrated electronic system as the two components are conjugated. As we see in Fig. 1.3b, i, an electron donor (e.g. dialkylamino-) and an electron acceptor (e.g. carbonyl) is attached to the two sides of the fluorophore respectively. Then, an ion chelator is integrated into the donor- or acceptor-side of the fluorophore. The introductions of electron donor and acceptor induce the polarisation of the π-electronic system, leading to the change in the intermolecular interaction between the fluorophore and the surrounding environment. For both ground and excited state of the fluorophore, its energy is affected by the degree of the interaction with the local environment, where a stronger intermolecular interaction, such as intermolecular hydrogen bonding [96], resulting in a lower energy scale and, therefore, a spectral shift to a longer wavelength, vice versa (Fig. 1.3b, ii). When the Ca^{2+} chelator is integrated into the indicator, the presence of Ca^{2+} modulates the polarity of the electronic system, depending on which electron group is bound to Ca^{2+}. For example, the binding of Ca^{2+} to the chelator (donor) of Fura-2 suppresses the electron-donating effect of the donor group, leading to a lower polarity of the molecule and, therefore, a reduced intermolecular interaction. As a result, the excitation wavelength shifts from 490nm to around 430nm and excitation wavelength-ratiometric measurement is achieved by collecting the ratio of the excitation intensities at these two wavelengths (Fig. 1.3b, iii) [79]. There are also indicators enable emission wavelength-ratiometric measurement, such as Indo-1.

The selection on either an intensity-based or ratiometric indicator requires to consider the aims of the study and accessible facilities in a specific scenario. For non-ratiometric indicators (intensity-based), the binding of Ca^{2+} causes concentration-dependent changes in fluorescence. Upon a certain excitation light, fluctuations in Ca^{2+} are reflected by the dynamic fluorescence intensities at a fixed emission wavelength. Thus, the task of monitoring Ca^{2+} through the intensity-based indicator can be accomplished by a simple spectrometer system, for which both excitation and emission light can be delivered and collected with the wavelength of interest. However, non-ratiometric indicators are not suitable for a quantitative study. Firstly, the optical signal strength of these indicators varies in different concentrations of indicators as well as the excitation conditions. Given that it is difficult to precisely identify the indicator's concentration within the cells, it would cause significant errors when correlating the observed fluorescence intensity with [Ca^{2+}]. Moreover, the leakage and photobleaching of the molecular dyes

undermine the prediction on the cellular [Ca^{2+}] via reading out fluorescence intensity scales. By contrast, the ratiometric indicators are featured with the capability of self-calibrating the recorded signals in ratio instead of only acquiring the absolute fluorescence intensity. Therefore, ratiometric indicators remove the interferences caused by the aforementioned factors: indicator concentration, indicator leakage, heterogeneous distribution, weak fluorescent signals and different optical settings.

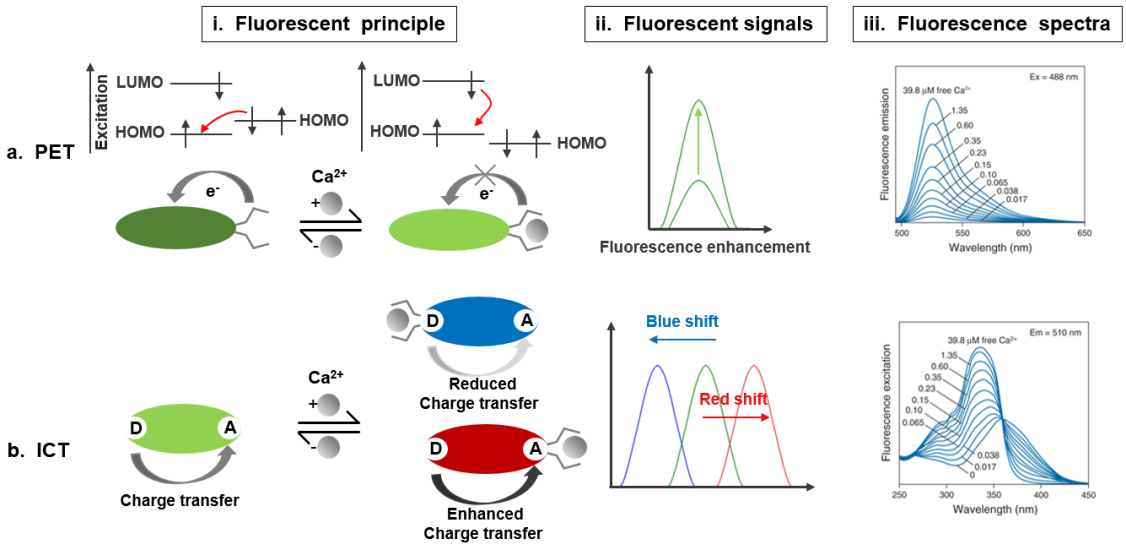

Figure 1.3 | Fluorescent principles and signal spectra of the synthetic fluorescent indicator. a | Fluorescent principle and example of fluorescent indicators based on PET: **i |** Schematic of Ca^{2+} binding-induced fluorescence enhancement via suppressing PET; **ii |** The fluorescent signal of PET-based indicator is the change in fluorescence intensity without spectral shift; **iii |** Fluorescence emission spectra of Ca^{2+} indicator, Fluo-3, which is based on PET [79]; **b |** Fluorescent principle and example of internal charge transfer (ICT) -based fluorescent indicators: **i |** Schematic of Ca^{2+}-binding modulates ICT, where the position of Ca^{2+}-binding chelator could exert the opposite effect on the ICT. When the chelator links to the charge donor (negatively charged), the binding of Ca^{2+} suppresses the electron transfer from the donor to acceptor; on the contrary, the Ca^{2+}-binding with the chelator linked to the acceptor will enhance the internal electron transfer; **ii |** The reduced charge transfer leads to a blue shift of fluorescent spectrum, while the enhanced charge transfer results in a redshift; **iii |** Excitation spectra shift of an ICT-based fluorescent indicator, Fura-2 [79].

Apart from the fluorescent mechanism, dissociation constant (K_d) of the indicator is also essential when determining the proper fluorescent indicator. As an intrinsic feature of chelator, K_d reflects the interaction between the recognition/binding unit and target ligand at equilibrium which therefore defines the effective range of an indicator capable of sensing [95]. Based on the

mass action law, a target concentration of 0.1~10 K_d is considered as the analytically practical range for a monovalent reversible binding. This is because that in the range of 0.1~10 K_d concentration, approximate 20 – 80% of the indicators are bound and the fluorescent signal of these bounded indicators show a relatively linear response to the change of target ions [97]. It demands that indicator with appropriate K_d be considered for varying studies targeting at different concentrations of ions. For example, in isolated islets, the glucose-induced $[Ca^{2+}]_c$ fluctuations were firstly recorded by Quin-2. In this experiment, it was observed that the glucose stimulates an initial decrease of $[Ca^{2+}]_c$, followed by a marked increase in $[Ca^{2+}]_c$ [80]. However, as the upper limit of Quin-2 in sensing Ca^{2+} is around 600nM (~10×K_d, Table 1.1) and $[Ca^{2+}]_c$ in β cells fluctuates between 40 and 1000nM, Quin-2 was not the optimal indicator for monitoring $[Ca^{2+}]_c$, particularly for the higher $[Ca^{2+}]_c$. To accurately monitor $[Ca^{2+}]_c$, the synthetic fluorescent Ca^{2+} indicators with both larger K_d of 100-400nm and a higher optical strength were developed (Table 1.1). Furthermore, Ca^{2+} indicators with even higher K_d (e.g. Rhod-2) were developed to monitor $[Ca^{2+}]$ in organelles, where $[Ca^{2+}]$ could be at much higher concentrations than it in the cytoplasm.

As discussed earlier, the secretion of insulin from the pancreatic islets involves multiple, dynamic regulatory pathways. A complete understanding of these complex processes relies on concurrent monitoring of multiple factors, including $[Ca^{2+}]$ in different compartments and other regulatory factors involving in the process. The expanding pool of fluorescent indicators with varying spectral features render the multiplexed sensing in a single experiment. As illustrated in Table 1.2, the multi-targets measurements have been advancing the understanding of the signalling and regulatory pathways in dynamic insulin release. In parallel, the development of multiplexed sensing work poses increasing demand on new-generation sensing platforms to be compatible with the multiple sensing techniques, thereby simplifying the experiment operations, minimising the undesired interference, and picturing the image towards comprehensive understanding on the mechanism of insulin secretion.

Table 1.2 | Multi-targets monitor in insulin secretion study

Targets	Indicators	Findings
1. $[Ca^{2+}]_c$ 2. NADH 3. MMP	Fura-red Auto-fluorescence Rh123	1. Slow oscillatory islet respiration induced by glucose depends on the interaction between ionic and metabolic events in β cells, which potentially comprise the pulsatile insulin secretion [90].
1. $[Ca^{2+}]_c$ 2. ATP 3. pH	Fura-red Perceval BCECF	1. Glucose-induced cytoplasmic ATP oscillation negatively regulated by $[Ca^{2+}]_c$; 2. The interaction between ATP and $[Ca^{2+}]_c$ underlying the pulsatile insulin secretion [98].
1. $[Ca^{2+}]_c$ 2. cAMP	Fura-2, Fura-red Translocation protein indicator	1. Glucose induces the cyclic adenosine monophosphate (cAMP) oscillation in β cells, which regulates the pulsatile insulin secretion [92]; 2. $[Ca^{2+}]_c$ enhances the cAMP oscillation, suggesting a Ca^{2+}-independent pathway for regulating insulin secretion [99].

*MMP, mitochondrial membrane potential.

The ever-evolving synthetic Ca^{2+} indicators are highly successful in monitoring Ca^{2+} in different pathways, but several inherent drawbacks of these indicators are noted. Firstly, for UV-excited indicators, the photobleaching is unavoidable. A severe fluorescence intensity drop was observed for the indicators under UV light exposure as short as 5 minutes [100], preventing the long-term real-time tracking the ions of interest [107]. Since photobleaching might occur at various wavelengths to different extents, the UV-excited ratiometric indicators become inaccurate for quantitative measurement [101]. Secondly, the exposure of cells or tissues to UV lights may affect their biological functions adversely. For example, the proportion of Ca^{2+} oscillation in β cells was substantially diminished after exposure to UV light for 30 minutes [38]. Although the Vis-excited Ca^{2+} indicators would circumvent the aforementioned issues caused by the UV light excitation, only a handful of such indicators have been developed, with limited K_d options and non-ratiometric fluorescent properties. Notably, both UV- and Vis-excited Ca^{2+} indicators are unable to be localised and retained around the targeted organelles and are therefore not suitable to monitor subcellular Ca^{2+}. Moreover, the by-products during the acetoxymethyl (AM) ester-assisted loading process, including formaldehyde and acetic acid, are potentially toxic and may impair insulin secretion from the β cells or islets. Finally, synthetic Ca^{2+} indictors commonly confront pitfalls including compartmentalisation, leakage, and incomplete hydrolysis [95].

1.3.2 Protein-based Ca^{2+} indicators

Originated from *Aequorea Victoria* jellyfish, protein-based Ca^{2+} indicators are classified as luminescent protein indicators and genetically encoded Ca^{2+} indicators (GECIs), represented by aequorin and green fluorescent protein (GFP), respectively. Historically, the bioluminescent Ca^{2+}-binding photoproteins were the first-generation indicators used for recoding intracellular Ca^{2+} changes via microinjection into cytoplasm [76,102]. Although the indicators facilitated the early studies on the importance of neuronal events [103,104], the microinjection requests the invasive loading, which has restricted the indicators' implementations on giant and robust cell types. In the 1990s, the renaissance of photoprotein aequorin was in line with the development of genetic engineering technology, permitting that recombinant aequorin was successfully expressed in mitochondria [95,105], which enabled the tracking of Ca^{2+} dynamics in the subcellular compartments. Soon after, the developed protein-based GECIs were put into the investigation of subcellular Ca^{2+} signalling. The early GECIs consist of two fluorescent proteins variants connected by a Ca^{2+}-responsive peptide calmodulin (CaM), and a calmodulin-binding peptide M13 [106]. Compared with the bioluminescent photoprotein, GECIs have a number of the inherent advantages, including higher brightness, no cofactors requirement, etc. [107-109].

The photoprotein aequorin is composed of an apoprotein apoaequorin and a chromophore, consisting of coelenterazine and oxygen molecule (Fig. 1.4a, i). In the presence of Ca^{2+}, the binding of Ca^{2+} to the indicators induces the intramolecular oxidation of coelenterazine to coelenteramide. The coelenteramide is further released from aequorin. As the coelenteramide decays from excited to the ground state, the process is coupled with the emission of a photon [110,111]. In the case of GECIs, there are three typical structures of these indicators: FRET-based GECIs, single-fluorophore GECIs and BRET-based GECIs. For FRET-based GECIs, the binding to Ca^{2+} induces the conformational changes of calmodulin and M13, which reduces the distance between the two fluorophores. FRET is subsequently permitted between the two fluorophores with a shorter distance, resulting in distinctive optical signal [112] (Fig. 1.4a, ii). For the single-fluorophore indicator, the conformational changes of the binding units alter the protonation state of the chromophore and (hence) the fluorescence intensity of the protein [107,109] (Fig. 1.4a, iii). Similar to the FRET-based GECIs, bioluminescence resonance energy transfer (BRET) – based GECIs have also been developed, which consist of a photoprotein aequorin and a fluorescent protein (Fig. 1.4a, iv) [113-115].

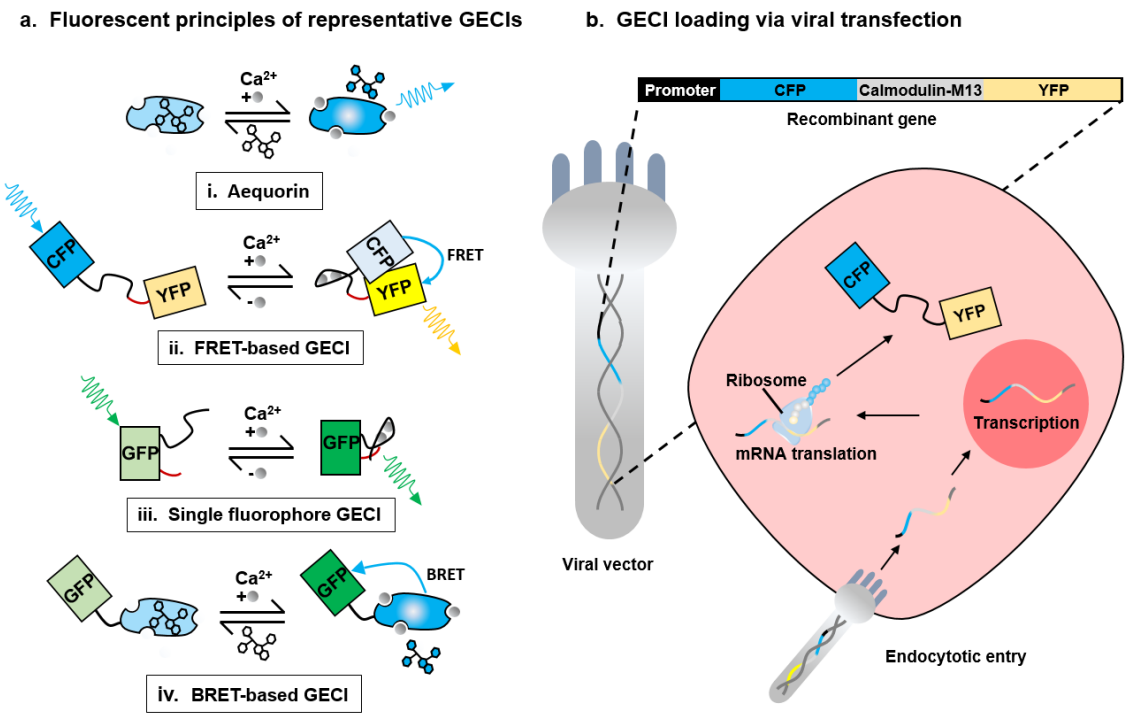

Figure 1.4 | Schematic of viral transfection loading and sensing principles of representative GECIs. a | Fluorescent principle of representative GECIs: i | In the presence of Ca^{2+}, aequorin undergoes internal oxidation of coelenterazine to coelenteramide, leading to the release of a coelenteramide and the emission of a photon of 470 nm. The re-functionalisation of aequorin requires the supplement of coelenterazine; **ii |** A GECIs based on FRET typically consists of a CFP, a YFP, a CaM (linker in "black") and a CaM-binding peptide M13 (linker in red). The Ca^{2+} binding-induced conformational changes CaM and M13 lead to a reduced distance between CFP and YFP. As a result, the fluorescence decreases in CFP while increases in YFP due to the increased FRET; **iii |** A representative example of GECI based on single GFP, where the binding of Ca^{2+} induces the conformational changes of CaM and M13. Such conformational changes affect the absorption spectra or fluorescence quantum yield of the fluorophore, which further displays an enhanced or decreased fluorescence intensity; **iv |** A single GFP can also be connected with aequorin. In the presence of Ca^{2+}, the fluorescence emitted by aequorin can excite the GFP via BRET. Therefore, the BRET-based GECIs enable the fluorescent measurement without an external light source; **b |** Schematic of viral transfection loading of GECIs into target cells. The vector virus carrying the fusion recombinant gene transfects the host cell and releases fused DNA into the host cell. With the help of integrase, the indicator DNA was integrated into the host gene and subsequently expressed in the target compartment after DNA transcription and mRNA translation.

Unlike the synthetic chemical indicators, which suffer from the inaccurate localisation and poor retainment of the indicators in the targets of interest over time [116,117,118], GECIs can be precisely localised in a target area through viral vectors introduction. Briefly, the cDNA sequence of the protein indicators is fused with a tag sequence from the target compartment. The encoded genes

are then integrated into the host DNA with the assistance of integrase of the vector. Depending on the origin of the tag sequence, the indicator is expressed in a specific compartment (Fig. 1.4b). When recombinant aequorin was first time introduced into insulin-secreting cells, glucose-induced oscillations of $[Ca^{2+}]_{mito}$ were recorded in MIN6 cell line and isolated rat islets [42,119]. To date, a number of GECIs have been utilised in islet study and are becoming essential tools for understanding the dynamic $[Ca^{2+}]$ in the subcellular compartment (Table 1.3).

From the first intracellular Ca^{2+} recording to the measurements of subcellular Ca^{2+}, the development of protein-based Ca^{2+} has facilitated the understanding of the microdomain Ca^{2+} signalling underlying biological events. Nevertheless, protein-based indicators have several limitations. For example, bioluminescent protein, although it does not require external excitation light, is not suitable to be used in the small or single-cell study. This results from the low light quantum yield of such protein [120], leading to a weak fluorescent signal. Another drawback concerning the application of aequorin is the requirement of cofactor coelenterazine in the culture medium to re-functionalise the aequorin after oxidation. For GECIs, they suffer from high sensitivity to pH and low fluorescence intensity [95,121]. Although cytosolic pH is under tight control in normal conditions, the pH fluctuations can still take place in response to inflammation and in the process of programmed cell death [122]. Additionally, the optical signal strength of protein indicators is often much smaller compared with that of chemical indicators. By comparing the Table 1.1 and Table 1.3, it shows that F_{max}/F_{min} or R_{max}/R_{min} of most protein-based Ca^{2+} indicators is < 10 (Table 1.3), while those of synthetic Ca^{2+} indicators are generally larger than 20, up to 100 (Table 1.1).

Table 1.3 | Fluorescent properties of protein-based Ca^{2+} indicators in islet research

Protein	Version	Cell Type	Targeting	K_d (μM)	λ_{ex} (nm)	λ_{em}(nm)	F_{max}/F_{min} (R_{max}/R_{min})	Note	Ref.
Aequorin	recombinant	1, 3, 4	mito	0.2-50	/	/		a	42,95,123
Pericam	2mt8RP	2	mito	1.7	415/490	535	(10)	b	44,55,124
Cameleon	Ycam-4ER	4	ER	100-1000	440	535/480	(1.4)	c	125,126
Cameleon	D4ER	2	ER	65	435	540/475	(3.8)	a	56,127

Subject:

1. INS-1 (insulin-secreting insulinoma cell line)
2. Isolated mouse β cells
3. MIN6 β cells
4. RINm5F cell lines

Note:

a. Recombinant aequorin: The low photon emission limits the application of aequorin on cell population study, requiring high sensitivity photomultiplier and amplifying the process. By combining it with Fura-2, the $[Ca^{2+}]_c$ and $[Ca^{2+}]_{mito}$ can be measured in parallel.

b. Pericam: It provides a ratiometric measurement. Simultaneously detect the $[Ca^{2+}]_{mito}$, $[Ca^{2+}]_c$ and $[ATP/ADP]_c$ with a combination of Fura-red and Perceval

c. Cameleon: Ycam-4ER has a low Ca^{2+} affinity and ratio-metric feature. Thus it is suitable to be used in a compartment with a high $[Ca^{2+}]$ like the ER.

d. Cameleon: Compared with Ycam-4ER, D4ER has a higher affinity to Ca^{2+} and the fluorescence intensity on Ca^{2+} binding.

1.3.3 Ion-selective microelectrode (ISM)

Based on the conventional microelectrode, which was used for measuring cell membrane potentials, resistance and net ion transport, the development of ISM has enabled the recording of specific ion flux across the membrane [128]. In principle, ISM converts the electrical currents relating the variations in specific ion concentrations into amplified dynamic electrical voltage signals. Typically, the ISM kit is composed of a sensing and a reference electrode, an amplifier and a voltmeter. In a liquid membrane ISM (Fig. 1.5a), the tip of the measuring electrode is filled with ion-selective ionophore (represented by ion carriers in membrane ISM) followed by internal electrolyte [129], while the reference electrode contains electrolyte like KCl. The ionophores reversibly bind to target ions and transport the ions from the aqueous sample bathing the microelectrode to the electrolyte within the microelectrode. The process of ion transport alters the electrochemical equilibrium of the electrolyte, leading to a variation in the potential between measuring and reference microelectrode. Accordingly, the ion concentration can be calculated based on the amplified voltage, which is proportional to the logarithm of the target ion activity. To date, a wide range of the ion-selective ionophores has been developed and measured with ISM for a number of ions, including Ca^{2+}, Na^{+}, K^{+}, H^{+}, Cl^{-} et al.

Compared with synthetic fluorescent indicators, the ISMs offer broader sensing range and longer measurement duration. For fluorescent Ca^{2+} indicators, they generally respond to $[Ca^{2+}]$ from nano- to micromole, while Ca^{2+}-selective microelectrodes (CSMs) shows the linear responses to $[Ca^{2+}]$ ranging from $10^{-7.5}$ to 10^{-1}M [130]; the latter fully cover the dynamic range of $[Ca^{2+}]_c$ as well as $[Ca^{2+}]_{ex}$. The ISMs are free from photobleaching and diffusion, which enables a stable and long-term recording of $[Ca^{2+}]_{ex}$ by being statically implanted in the extracellular fluid. Thus, the ISMs have been successful in revealing the dynamic $[Ca^{2+}]_c$ and $[Ca^{2+}]_{ex}$ in a variety of biological setups, including neural tissue [131,132], bone fragment [133], cardiac muscle [134], gastric mucosa [135] as well in islet study [67,136,137].

The first application of ISM on islet study dates back to 1986, when Perez-Armendariz and Atwater measured $[Ca^{2+}]_{ex}$ around β cells of a mouse islet with CSM [136]. They found that a 0.5mM depletion in $[Ca^{2}]_{ex}$ was induced by 11mM glucose stimulation and the $[Ca^{2}]_{ex}$ returned to basal level followed by this depletion; the reversible fluctuations repeated during the measurement. Although the measurement only lasted for ~1 minute, the results, to a certain degree, projected the profile of fast oscillatory activity of Ca^{2+} under stimulation. Similar depletion of Ca^{2+} efflux stimulated by the same glucose concentration was observed when

Moura, A. implanted the microelectrode tip nearby the cytoplasm membrane in β cells. Efflux of Ca^{2+} rose back but oscillated in phase with the membrane potential. The oscillation pattern ceased immediately as the glucose stimulation was removed [137]. However, as the measuring microelectrode was impaled within the cytoplasm membrane, the oscillatory pattern was more likely to be attributed to the dynamic $[Ca^{2+}]_c$ fluctuations induced by glucose rather than the result of dynamic $[Ca^{2+}]_{ex}$. The most recent and reliable $[Ca^{2+}]_{ex}$ measurement in islet study was conducted by Gerbino, A. et al, in which CSM was positioned in the intercellular cavity within the INS-1E pseudoislet (PI) (Fig. 1.5b) [138]. The glucose-evoked $[Ca^{2+}]_{ex}$ reduction was confirmed in this study. Moreover, a significant increase in $[Ca^{2+}]_{ex}$ was observed following the reduction, suggesting that insulin secretion from granules alters local $[Ca^{2+}]_{ex}$. However, as the electrode was set in a relatively restricted space, its position may affect the response time and sensitivity (amplitude), which blurs the spatial and temporal resolutions.

As discussed in section 1.2.2, $[Ca^{2+}]_{ex}$ plays a critical role in mediating intercellular communication and synchronising β cells and islet activities for the pulsatile secretion of insulin. Therefore, the robust detection of both $[Ca^{2+}]_{ex}$ and the pulses of insulin secretion is intriguing. Though currently employed Ca^{2+} sensing techniques allow to picture the transient Ca^{2+} events within the islets, correlation of the varying interstitial $[Ca^{2+}]$ with insulin secretion utilizing the currently available sensors remains an extremely challenging task (Table 1.4). The interstitial $[Ca^{2+}]$ is at the concentration of ~1.2mM, which is over three orders magnitude higher than the $[Ca^{2+}]_c$ [139]. At this level of Ca^{2+}, fluorescence-based indicators are generally saturated and would, therefore, be problematic to show genuine dynamics of interstitial $[Ca^{2+}]$ by monitoring the fluorescence changes, unless the $[Ca^{2+}]$ is intentionally maintained at an unrealistic low level. However, the latter setting misses the true events *in vivo*, so that the relevance and significance of the results are limited [74]. In terms of ISM, the protocol is only effective in recording the Ca^{2+} activity around the detection tip, typically limited around 1μm, which is insufficient to reveal the dynamic $[Ca^{2+}]$ change in a multicellular or tissue level [140,141].

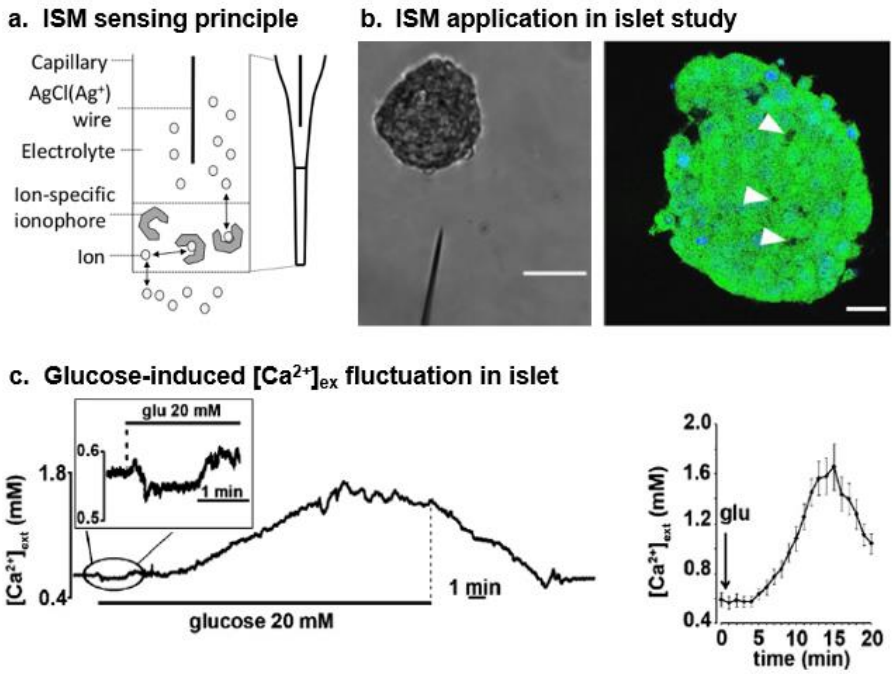

Figure 1.5 | Sensing principle and applications of ISM in islet study. a | Schematic of the ISM tip structure and sensing mechanism. The ionophore at the tip of the detection probe can reversibly convert the ions from the working environment to the inner electrolyte [129]. As the ionic component changes in the electrolyte, the potential varies between the detection probe and reference probe, which contains solution such as KCl without ionophore. The changes in the target ion concentration will be read out by a voltage meter; **b |** Illustration of the placement of ISM tip in measuring $[Ca^{2+}]_{ex}$ of INS-1E pseudoislet [138]. Optical microscope image shows a double-barrelled selective microelectrode in the proximity of the PI ***(left)***. Scale bar, 100μm. A confocal microscopy picture exhibits an entire PI stained by BCFCF (green) and Hoechst (blue), showing the cytoplasm and nuclei respectively ***(right)***. The white triangles point out the cavity for positioning the tip of ISM; **c |** The Ca^{2+} changes in the intercellular space within an INS-1E pseudoislet in response to 20mM glucose *(left)*. Time course of dynamic $[Ca^{2+}]_{ex}$ under 20mM glucose stimulation ***(right)***.

In order to probe $[Ca^{2+}]_{ex}$ at multicellular or tissue-level, such as intra-islet $[Ca^{2+}]_{ex}$, the sensors are expected to be capable of : (i) generating signal changes in response to sub-millimolar Ca^{2+} fluctuations in the high background of intra-islet Ca^{2+} (1mM); (ii) correlating multicellular $[Ca^{2+}]_{ex}$ with the dynamic insulin secretion, instead of the localised measurement; (iii) measuring the Ca^{2+} dynamics in a highly preserved *in vivo* secretion conditions. In this regard, there is no established method that is capable of distinguishing the small fluctuations of $[Ca^{2+}]_{ex}$ in the context of high background and, in the meantime, correlating the dynamic $[Ca^{2+}]_{ex}$ with the insulin secretion. Fortunately, the fast-evolving microfluidic devices are being a promising platform to overcome the long-standing challenges towards comprehensive secretion analysis.

Table 1.4 | Summary of Ca^{2+} sensors for islet studies

	Synthetic indicator	Protein-based probes		ISM
		Recombinant Aeq	GECIs	
Interest of sensing	Cytosolic Ca^{2+}	Endoplasmic reticulum and mitochondria Ca^{2+}		Extracellular Ca^{2+}
Corresponding [Ca^{2+}]	0.04 – 1μM [36,142,143]	50 – 500μM or 0.1 – 70μM [30]		500 – 1500μM [138]
Sensing principle	Binding-induced spectroscopic properties changes (intensity, wavelength, etc.)	Intramolecular oxidative reaction-induced luminescence emission	Ion-dependent conformational changes-induced fluorescent signal	Ion-selective transport-induced electrical signal
Loading method	AM-ester loading	Plasmid transfection		Physical implantation
K_d	0.06 – 0.39μM [79]	0.2 – 50μM [144,145]	1.7 – 1000μM [95,146]	10^{-4} – 10^{2}μM [147,148]
Signal strength scale	+ + + + +	+	+ + +	
Advantages	- ratiometric measurement - high S/N ratio - large available library - biocompatible loading method	- no excitation required - non-photobleaching - precise localisation to targets	- ratiometric measurement - precise localisation to targets	- stable electrical signal reading - high ion selectivity
Limitations	- photobleaching - interference by other metal ions - cytotoxicity concerns - compartmentalisation	- non-ratiometric measurement - ultralow emission intensity - transfected loading via viral vector	- pH-sensitive spectrum - photobleaching - transfected loading via virus vector	- limited to electrode point (no mapping) - complicated calibration - longer response time

S/N, signal to noise ratio. The fluorescent indicators generally show linear fluorescence changes to Ca^{2+} ranging from 0.1 × K_d to 10 × K_d; [Ca^{2+}] refers to the Ca^{2+} concentration in each compartment of pancreatic β cells

1.4 Microfluidic devices for secretion analysis

With the increasing demands in the physiological relevance of experimental setup, dynamic control on the cell culture environment to well mimic *in vivo* scenarios is emerging as a fundamental requirement in the biological study, which can hardly be achieved by traditional culture techniques. The conventional cell culture is generally conducted in a flat cell culture dish/plate, where cells are statically immersed in the cell culture medium. The changes in cell culture environment are achieved by manually replacing the medium or supplementing specific stimulus into the medium. Therefore, conventional cell culture suffers from the inconvenience in sample manipulation. It is time/labour- consuming to achieve the physiological culture environment which changes dynamically in accordance with the *in vivo* conditions [149]. Secondly, highly frequent sampling is required to monitor the dynamic secretory activity. This is not only a labour-intensive process, but also would change the cell culture environment as the medium is continuously collected from the well for analysis [150]. Thirdly, it is extremely challenging to study the dynamic secretory interactions between cells or tissues by conventional culture method due to its static and isolated nature. To highly replicate the experimental culture as the *in vivo* conditions, the microfluidic devices based on microfluidic perfusion system (MPS) are emerging as invaluable tools for investigating the fingerprint of islet secretion [151,152].

The microfluidic devices designed for islet secretion analysis typically consist of three key components, including perfusion controller, cell/tissue culture chamber and analytical apparatus (Fig. 1.6a) [153]. The perfusion controller is used to manage the flow rates and dynamic gradients of the purpose-designed medium that is applied to cultured islets in the chamber. Therefore, the constant flow of culture medium not only provides the necessary refreshing nutrients for maintaining cell viability, but also dynamically controls the stimulatory components in the extracellular environment. To evaluate the islet function under hypoxia condition, Eddington, D. T. et al. designed on-chip MPS with the capability to adjust the oxygen content in the microenvironment of islets [154,155]. Following the same principle, Roper, M. G. et al. successfully manipulated the dynamic glucose delivered to islets, with manageable amplitude and periodicity [156-158]. As the perfusion fluid is pumped into the culture chamber, the insulin level in the flowing samples is a dynamic indicator of the secretion activity of β cells or intact islet. To stabilise the cells/tissues in a flowing condition, four trapping mechanisms are currently applied on MPS in islet studies, including dam-wall like traps (Fig. 1.6b, i) [159,160],

tissue nozzle (Fig. 1.6b, ii) [161], U-shape cups islet arrays (Fig. 1.6b, iii) [162] and circular wells at the bottom of a chamber (Fig. 1.6b, iv) [163]. A recently designed microfluidic device is capable of mounting up to 100 islets [162]. However, the limitation of applying MPS is the longevity of the culturing pancreatic islets isolated from the pancreas. So far, the maximum culture period in microfluidic device lasts up to 48 hours, which is much shorter than the *in vitro* culture of primary cells (a few weeks) [164].

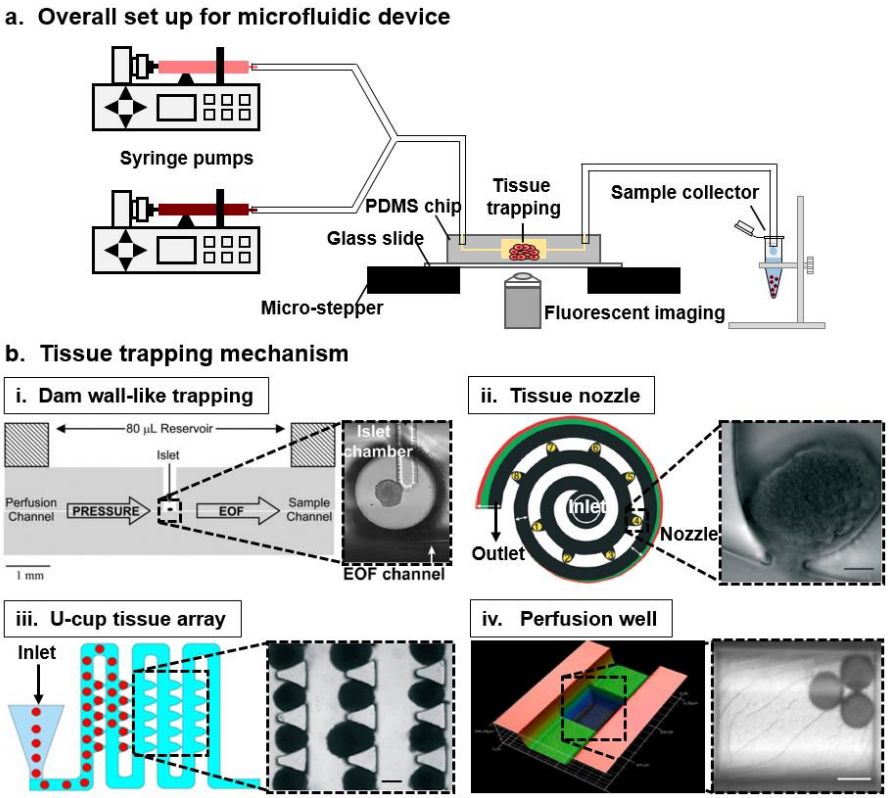

Figure 1.6 | Schematics of general MPS set up and tissue trapping mechanism for islet study. a | A typical microfluidic set up for pancreatic islet study; b | Representative mechanisms for tissue immobilisation: **i |** Dam wall-like islet trap in microfluidic chips for simultaneous monitoring for $[Ca^{2+}]_c$ and insulin secretion [159,160]; the electro-osmotic flow (EOF) channel shows the pathway of samples for insulin quantification; **ii |** Nozzle-like traps in a microfluidic chip for highly efficient viral transduction of pancreatic islets [161]. The microfluidic channel was designed into a spiral shape, which significantly enhanced the efficiency of interstitial exchange within the islets; **iii |** A U-shape cups tissue array in a microfluidic chip for real-time imaging of multiple islets [162]. The tissue array was shown to capture pancreatic islets without clogging in the perfusion channel; **iv |** A 3D perfusion well in a microfluidic chip for multi-parametric measurements of pancreatic islet physiology [163].

By incorporating the different analytical tools into the MPS, the multi-parametric devices have been invented and work as multiplexed sensors in studying islet. To date, optical sensing technique and capillary electrophoresis immunoassay (CEI), are two major protocols that are applied on MPS for islet study [159,165-174], both of which permit a number of key factors (Table 1.5) influencing the insulin secretion to be monitored in parallel. The major advantages of using microfluidic devices include: (i) the high-degree automation for multiplexing measurement against independent fluorescent imaging and protein analysis [163], leading to the significantly increased working efficiency and reproducibility [150,175,176]; (ii) the high reproduction of the microenvironment of the cell interplay *in vivo* by dynamically controlling *in vitro* culture, which is promising for studies on intercellular communication and interaction between different tissues. For example, the MPS platform has been utilised to investigate the effect of the interaction between gut and islet on GSIS [164]; (iii) the high compatibility of MPS with a number of emerging techniques, such as the patch clamp, amperometry and surface plasmon resonance [151], displaying the potential for being modified into a multiplexed sensor.

Table 1.5 | The versatile MPS-based devices for islet study

Targets	Analytical Tools	Subject	Aim / Finding
NAD(P)H $[Ca^{2+}]_c$ O_2 consumption Insulin	Auto-fluorescence Fura-2 Commercial O_2 Sensor ELISA	MIN6 cells; mouse islets	Established a multiparametric MPS for investigating the metabolic activity underlying the regulation of insulin secretion via paralleled measurement of oxygen consumption, NAD(P)H, $[Ca^{2+}]_c$ and insulin release [163].
$[Ca^{2+}]_c$ Insulin	Fura-2/Fura-PE-3 CEI	Single murine islet	Constructed a dual detection system that can simultaneously measure the intracellular factor and extracellular release [160].
$[Ca^{2+}]_c$ MMP Insulin	Fura-2 Rh123 ELISA	Mouse/human islet	Fabricated a pumpless MPS, providing a simplified microfluidic device for islet study [177].
$[Ca^{2+}]_c$ MMP Tissue Viability	Fura-2 Rh123 CMFDA/PI	Mouse/human islet	Largely improved the spatiotemporal resolution, enabling the monitor of the viability and activity of a large cell population at the single islet level [162].
Amino acid	Derivatisation and electrophoretic separation	Mouse/human islet	Measured secretion rate of 9 amino acid secreted from pancreatic islets in real-time [178].

Although MPS is currently promising for the reconstruction of *in vivo* model by recapitulating the complex feature of a biological system, further improvements are required before the MPS can be promoted as a common method. Firstly, the microfluidic devices so far require sophisticated skills and facilities from design to on-bench application. Simplification,

particularly the experiment set up, is necessary for those devices to achieve widespread use, ideally a daily benchtop analyser. Secondly, the MPS devices are expected to enable the simultaneous tracking of a variety of biomarkers, i.e. ions, hormones and neurotransmitters in the interstitial space. With the capability of multiplexed sensing, the microfluidic devices will significantly accelerate the analysis procedure and provide insightful results for complex biological events.

1.5 Research objectives

The aim of the thesis is to develop an advanced microfluidic sensing platform that can be used for simultaneously monitoring the dynamic changes of Ca^{2+} in the extracellular environment and the secretion of insulin (and perhaps other metabolic hormones) from the islets or endocrine pancreas, which involves:

1. Establishment of a fluorescence-based method capable of quantitatively and selectively measuring dynamic sub-millimolar [Ca^{2+}] fluctuations against a high [Ca^{2+}] background (around 1mM).

2. To design, fabricate and characterise a microfluidic device capable of immobilizing pancreatic islet while providing dynamically controllable nutrient and stimulation to regenerate the *in vivo* secretion environment.

3. Demonstration of the capacity of the sensor for simultaneous measurement of the dynamic [Ca^{2+}] and hormone levels in biological samples.

Chapter 2

Evaluation of synthetic fluorescent Ca^{2+} indicator for $[Ca^{2+}]_{ex}$ sensing

The work of this chapter has systematically evaluated the feasibility of utilising Calcein and Rhod-5N as fluorescent sensors for monitoring $[Ca^{2+}]_{ex}$ in the biological system. This evaluation covers the critical optical properties of the indicators, fluorometric responses in the presence of Ca^{2+}, and their selectivity profiles. By comparing the performance of these two indicators, the indicator, Rhod-5N, was identified to be suitable for use in the following microfluidic platform.

2.1 Background

2.1.1 Fluorescent Ca^{2+} indicator with low binding affinity

As aforementioned, the $[Ca^{2+}]_{ex}$ is generally two orders magnitude higher than the $[Ca^{2+}]_c$. This fact prevents the direct transition of fluorescent Ca^{2+} indicators for intracellular applications to extracellular events, as the Ca^{2+} indicators for the intracellular environment are easily saturated in the extracellular fluid. The saturation means that the binding sites of the intracellular indicator molecules are fully occupied by Ca^{2+} even with a concentration lower than basal extracellular Ca^{2+} level. These saturated indicators are inert to the changes of $[Ca^{2+}]$ and unable to reflect the dynamic changes of $[Ca^{2+}]$ during physiological events. Therefore, fluorescent Ca^{2+} indicator with low binding affinity, referring to the indicators that are turned on and display distinctive fluorescent signal in the presence of a high concentration of Ca^{2+}, is a prerequisite for $[Ca^{2+}]_{ex}$ study. Currently, two types of fluorescent indicators with low binding affinity and thus high dissociation constant (K_d, 0.1~10 K_d is the general sensing range of the

indicator) have been developed: one is based on the well-known 1, 2- bis(o-aminophenoxy)ethane-N, N, N', N'-tetraacetic acid (BAPTA) [179,180], and the other based on tetraphenylethene (TPE)-appended polyacrylic acid (PAA) [181]. Both high-K_d indicators are capable of sensing [Ca^{2+}] around 1mM and are competent for Ca^{2+} in the highly ionic environment of extracellular fluid.

The production of the low-affinity indicators is principally based on the strategy that alters the ratio of Ca^{2+} binding domain (i.e. the carboxylic group) to the fluorophore molecule. Due to the excellent ion selectivity of BAPTA-based fluorescent indicator, many efforts are made to modify these fluorescent indicators to tune up the range of sensing capability to [Ca^{2+}]. For BAPTA-based fluorescent indicators (unmodified), they are typically composed of four carboxylic groups as the Ca^{2+} binding units [79]. By truncating the carboxylic groups into half, the Ca^{2+}-binding strength of the indicators is reduced [182,183]. He, H. et al synthesised the indicator based on anisine-N, N-diacetic acid, which consists of fluorophore and half of the binding units of BAPTA (Fig. 2.1a, *left*). By weakening the binding strength, their modified indicator exhibited a 34%/mM fluorescence change in the Ca^{2+} range of 0.3-2.2mM (Fig. 2.1a, *right*). This modified BAPTA-based indicator showed excellence for $[Ca^{2+}]_{ex}$ measurement with outstanding selectivity to Ca^{2+} over Mg^{2+}, but also performed highly stable in aqueous solution[179]. Although Mg^{2+} is often regarded as one of the major interference ions for $[Ca^{2+}]_{ex}$ sensing, the general use of this indicator in complex physiological conditions is pending without the evaluation on the selectivity of the indicator to Ca^{2+} versus other physiological metal ions, e.g., Na^+, K^+ and Fe^{2+} at physiological concentrations.

In another study, Kevin and his colleagues developed the indicator utilizing truncated BAPTA as the Ca^{2+} recognition unit, and the fluorophore, boron-dipyrromethene (BODYPY) (Fig. 2.1b, *left*) [180]. With the weakened Ca^{2+} recognition site, the indicator displayed a K_d around 0.92mM to Ca^{2+} (Fig. 2.1b, *right*) and on average 9 times higher selectivity to Ca^{2+} over other metal ions in physiological condition. The results gained from cell experiment demonstrated this cell-impermeable indicator was qualified to track $[Ca^{2+}]_{ex}$ in a cellular environment.

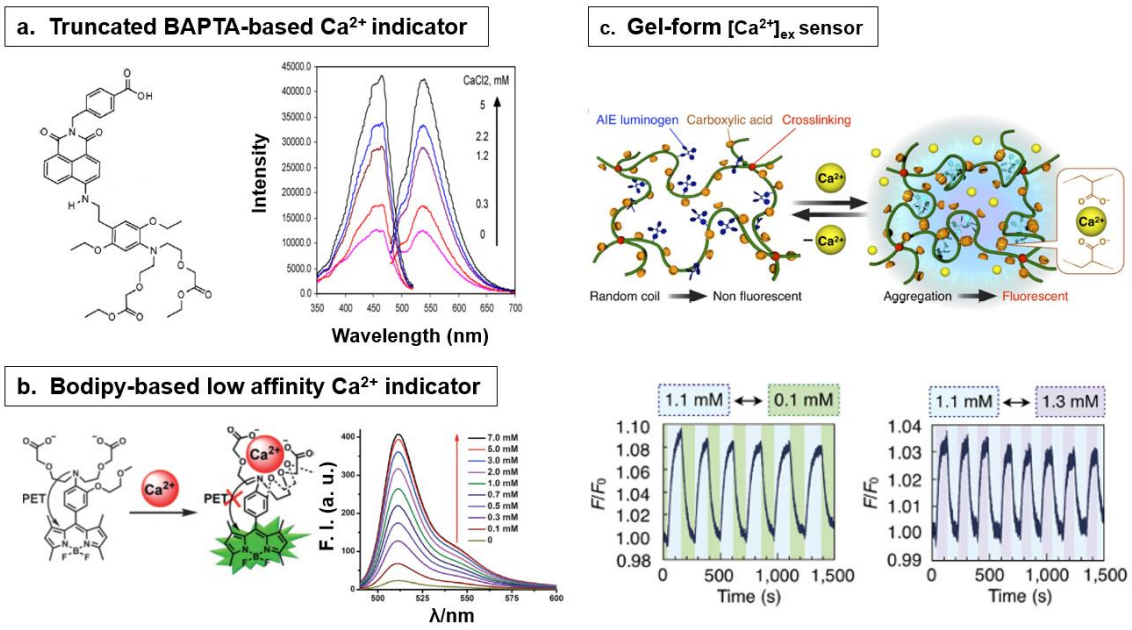

Figure 2.1 | Emerging low-affinity Ca^{2+} indicators for measuring the high concentration of Ca^{2+}. a | A low-affinity Ca^{2+} indicator was designed based on truncated BAPTA [179]. The indicator consisted of a BAPTA-based Ca^{2+} recognition unit and a fluorophore ***(left)***. The indicator exhibited significant fluorescence changes in presence of Ca^{2+} from 0 to 5mM ***(right)***; **b |** A BODYPY-based low-affinity Ca^{2+} indicator was synthesised for Ca^{2+} quantification in blood sample [180]. The fluorescent principle mediated by PET ***(left)***. The fluorescence changes in response to increasing Ca^{2+} concentrations ***(right)***; **c |** A gel form Ca^{2+} sensor based on PAA-TPE [181]. Fluorescent principle of the AIE-induced fluorescence within g-PAA-TPE in sensing Ca^{2+} **(*top*)**; the fluorescence changes in response to the alteration in $[Ca^{2+}]$ presented by an artificial flowing system **(*bottom*)**.

However, it is found that the application of these modified BAPTA-based Ca^{2+} indicators with low-affinity is still limited. This is likely because the boundary-free extracellular environment poses challenges to the applications of these small molecule-based indicators. As the molecule-based indicators tend to aggregate or diffuse away from the place of interest, the unstable concentration of the indicators would significantly interfere with the accuracy of the long-term recording. To overcome this issue, Ishiwari, F. et al. synthesised a polymer gel-based sensor, which was composed of Ca^{2+} binding backbone polyacrylic acid (PAA) and luminogen tetraphenylethene (TPE) [181]. When the functional carboxylic acid bound with Ca^{2+}, the chemically-crosslinked PAA experienced a single-chain aggregation. As the aggregation-induced emission (AIE) luminogenic TPE was attached to the PAA backbone, the conformational changes from isolated form to aggregation state was translated into fluorescent signals, which was dependent on the $[Ca^{2+}]$ (Fig. 2.1c, *top*) [184]. Similar to the BAPTA indicators, the ratio of the fluorophore and binding domain in PAA-TPE could be tuned by

adjusting the ratio between the backbone PAA and the pendants TPE (containing the Ca^{2+} binding carboxylic groups). The consequent sensors displayed varying binding efficiency [185], resulting in a serial K_d ranging from 0.43 – 13mM, which was a comparable range to the fluctuation of $[Ca^{2+}]_{ex}$. Moreover, this indicator showed at least 4 times higher selectivity to Ca^{2+} than that to other metal ions at physiological concentrations. In order to test the temporal resolution, the indicator had been integrated into a micro-perfusing system, where the gel-form indicators showed fluorescent signal changes in response to pseudo extracellular fluids with oscillating concentrations of Ca^{2+} (Fig. 2.1c, *bottom*). However, the maximum fluorescence intensity induced by Ca^{2+} was approximated only 110% of the background fluorescence in the absence of Ca^{2+}. The limited signal to background ratio prevents the application of the indicator on recording minor fluctuations of $[Ca^{2+}]$.

2.1.2 Calcein and Rhod-5N

Although much attention has been paid to the development of novel fluorescent indicators for sensing $[Ca^{2+}]_{ex}$, the evaluation of commercially available indicators for monitoring $[Ca^{2+}]_{ex}$ is largely neglected. With a comprehensive literature review, two fluorescent Ca^{2+} indicators, Calcein and Rhod-5N, are identified to be potentially competent candidates.

Calcein is a versatile fluorescent indicator in terms of its fluorometric properties and applications. As shown in the top panel of Fig. 2.2a, Calcein consists of one fluorescein and two methyleneiminodiacetic acid groups attached to the xanthene portion of the fluorescein. Theses methyleneiminodiacetic groups serve as ion chelators, which interact with ions and significantly affect the fluorescence of the molecule (Fig. 2.2a, *top*) [79]. First introduced in 1956, Calcein displayed a remarkable yellow-green fluorescence in the presence of metal ions, most notably Ca^{2+} [186] (Fig. 2.2a, *middle*). These useful fluorometric properties were soon utilised to develop quantitative methods for analysing serum Ca^{2+} concentrations in an alkaline environment (Fig. 2.2a, *bottom*)[187-189]. Owing to the pH- and concentration-dependent fluorometric properties of fluorescein, the fluorescence of Calcein is directly influenced by the pH of the working environment and the concentration of applied Calcein [190]. As a result, dependent on the working environment (alkaline or neutral solutions), Calcein can exhibit both fluorescence enhancement and quenching in response to the ions of interest. For example, the enhanced optical signal was observed in the presence of Cd^{2+} via the formation of Cd^{2+}-Calcein

fluorescent complex at high pH [191], while the fluorescence of Calcein was quenched by Fe^{2+}, Cu^{2+}, UO_2^{2+}, rare earth ions under about neutral pH conditions [192-196].

Rhod-5N is another promising fluorescent indicator for measuring $[Ca^{2+}]_{ex}$. As far as the best of our knowledge, Rhod-5N provides the lowest binding affinity with Ca^{2+} (K_d = 320μM) among the commercially available fluorescence-based Ca^{2+} indicator. Rhod-5N, a derivative of rhodamine-based indicator, is featured by high fluorescent efficiency with emission peak around 580nm (Fig. 2.2b, *top* and *middle*). In the absence of Ca^{2+}, Rhod-5N is essentially non-fluorescent; in contrast, the presence of Ca^{2+} switches on the indicator with two orders of magnitude fluorescence enhancement. In the previous study, 3mM Rhod-5N was filled in a micro-droplet (a concentric glass shell) in junction with a micro-pipette to form a probe. The microprobe was placed in the interstitial fluid of neural cells around which the $[Ca^{2+}]_{ex}$ dynamics was recorded by the micro-pipette probe. As shown in the bottom panel of Fig. 2.2b, the micro-probe displayed a linear response to 0 – 2mM of Ca^{2+}.[197] Besides the extracellular Ca^{2+}, Rhod-5N was used for monitoring the dynamic $[Ca^{2+}]$ changes in the intracellular compartments with a high $[Ca^{2+}]$, e.g., mitochondria [198,199]. Compared with Calcein that is sensitive to the pH of the environment or the indicator concentration, Rhod-5N is relatively independent of these factors, but it is noteworthy that the ionic strength could influence the sensitivity of Rhod-5N to Ca^{2+}. [200]

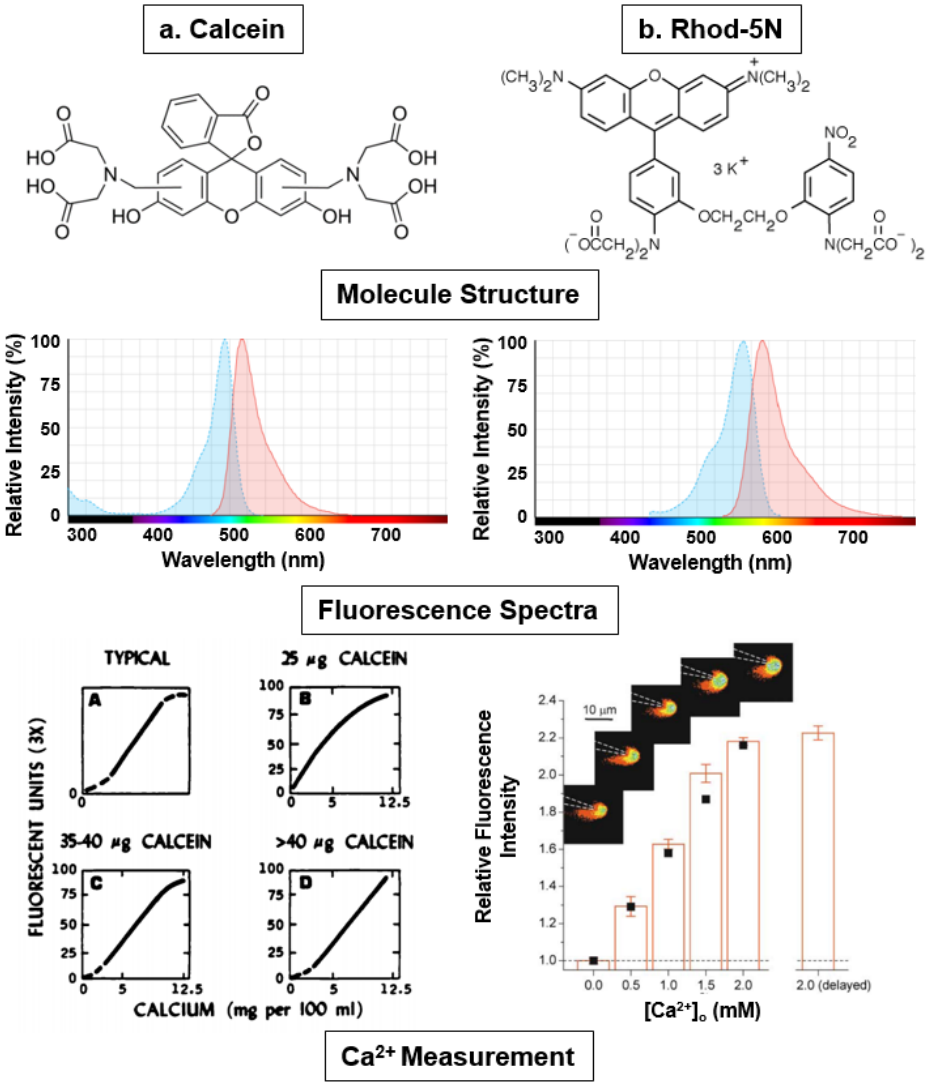

Figure 2.2 | Introduction to Calcein and Rhod-5N. a | The molecular structure of Calcein in AM ester form **(*top*)**; the fluorescent excitation (blue) and emission (red) spectra of Calcein **(*middle*)**; The application of Calcein in quantifying the Ca^{2+} concentration in serum **(*bottom*)** [187]; **b |** The molecular structure of Rhod-5N in AM ester form (***top***); the excitation (blue) and emission (red) spectra of Rhod-5N **(*middle*)**; the application of Rhod-5N in measuring $[Ca^{2+}]_{ex}$ in proximity to a neural cell **(*bottom*)** [201].

2.2 Sample preparations, data acquisitions and analysis methods

2.2.1 Apparatus and reagents

The spectroscopic profiles of both Calcein and Rhod-5N were measured by Synergy H4 Hybrid Multi-Mode Microplate Reader (BioTek, USA) in 96-well assay plate (black plate, clear bottom, Corning, USA) at room temperature. The scanning speed was set as 2nm with the bandpass at 9nm. The sample volume for all samples was fixed at 100μL in each well for

quantitative comparison. For higher accuracy in a quantitative study, all spectra here were recorded with duplicate measurements at room temperature.

The pH of all samples was pre-adjusted accordingly by a pH metre (827 pH lab Metrohm, NSW, Australia). The pH metre was calibrated with buffer solutions pH 4, 7 and 9 (Metrohm, NSW, Australia) before the first measurement in the day.

All glassware used throughout the experiment was cleaned by washing with detergent, sonicating for 15 minutes, followed by rinsing with distilled water. Then the glassware was flushed three times with acetone (Chem Supply, Australia) and blow dried. After that, the glassware was rinsed with deionised (DI) water (Milli-Q, Australia) before drying.

Ca^{2+}, Mg^{2+}, K^{+}, and Na^{+} ions were provided in the form of chlorate salts (Chem-Supply, Adelaide, Australia). Other metal ions, such as Fe^{2+}, Cu^{2+}, Zn^{2+}, and Al^{3+} were provided in the form of perchlorate salts (Sigma-Aldrich, St. Louis, USA). The reagents (shown in Table 2.1) for the preparation of phosphate-buffered saline (PBS) were purchased from Chem-Supply (Adelaide, Australia). All the salts were in analytical grade and used without further purification.

The fluorescent indicator Calcein (>93%) was purchased from Sigma-Aldrich (Sydney, NSW, Australia) and Rhod-5N (tripotassium salt, cell impermeant) was purchased from Life Technologies (Mulgrave, VIC, Australia). Both indicators were supplied in crystalline solid and directly dissolved in a freshly prepared solvent before use.

2.2.2 Fluorometric characterisation of Calcein as a function of Calcein concentration (pH 7.4)

As fluorometric properties of Calcein are significantly affected by the Calcein concentration and pH of the working environment, its excitation and emission spectra as a function of Calcein concentration were first studied at pH 7.4. Taking into account the slight solubility of Calcein in water and the following biological demonstrations, PBS was used as the solvent to dissolve Calcein in this experiment.

Considering the strong acidifying effect of Calcein, a 500ml pH 12 PBS buffer was prepared and used to directly dissolve Calcein as the stock solution, and a 500ml pH 7.4 PBS buffer was

prepared to dilute Calcein into serial concentrations. Both of the PBS buffers were freshly prepared prior to the preparation of Calcein solution. The compositions of PBS buffer (shown in Table 2.1) were dissolved in DI water and the pH was adjusted to 12 and 7.4 with 2 M NaOH and 3% HCl respectively.

Table 2.1 | The composition of PBS

Salt	Molar Concentration (mM)	Mass Concentration (g/L)	Weight (g)
NaCl	137	8.0	4
KCl	2.7	0.2	0.1
Na_2HPO_4	10	1.42	0.71
KH_2PO_4	1.8	0.24	0.12

A 20mM stock solution of Calcein was prepared by dissolving 622.5mg Calcein (MW = 622.53) in pH 12 PBS buffer. Before use, the stock solution was pre-adjusted to pH 7.4 and subsequently diluted into serial concentrations of Calcein from 0.5μM to 18mM by pH 7.4 PBS buffer.

Regarding the optical measurements, excitation spectra were obtained from 250 to 550nm with the emission fixed at 580nm. The gain rate was set as 50 % with a read height of 8mm. Emission spectra were obtained between 490 and 700nm with the excitation fixed at 470nm. The gain rate was set as 50 % with a read height of 8mm.

2.2.3 Fluorometric characterisation of Calcein (3mM) as a function of pH

In order to investigate the fluorometric properties of Calcein in various pH environments, the fluorescent excitation and emission of Calcein were measured in a range of pH between 3 and 12. A 3mM Calcein solution was prepared by dissolving 62.25 mg Calcein in 50mL pH 7.4 PBS. The pH of the solution was subsequently adjusted into 3, 4, 5, 6, 7, 8, 9, 10, 11, 12 with 2M NaOH and 3% HCl. Excitation and emission spectra were obtained with the identical setting as described in 2.2.2.

2.2.4 Fluorescent characterisation of Calcein in response to Ca^{2+} at pH of 12 and 7.4

As abovementioned in 2.1.2, previous studies suggested that Calcein showed significant fluorescent signals in response to Ca^{2+} in serum samples in an alkaline environment (pH 12). However, the final concentrations of both Calcein and Ca^{2+} were around 10μM and the serum samples were diluted. As the previous reports provided hints on the pH condition, it is worthwhile to investigate the feasibility of using Calcein to quantify high [Ca^{2+}] without dilution at pH 12. Therefore, the Ca^{2+}-induced fluorometric response of Calcein was systematically evaluated in the presence of 0-2mM Ca^{2+} at pH 12 in this work to examine the feasibility of utilising Calcein for $[Ca^{2+}]_{ex}$ detection. In addition, the sensing environment was adjusted to pH 7.4 to explore whether Calcein is capable to detect $[Ca^{2+}]_{ex}$ at a biologically relevant pH.

A stock solution of 20mM Calcein was prepared by dissolving 622.5mg Calcein in 50mL pH 12 PBS and the pH of the stock solution was adjusted to 12. The Calcein stock solution was subsequently diluted into 0.1, 0.2, 1, 2, 4 and 6mM with pH 12 PBS buffer. A stock solution of 200mM Ca^{2+} was prepared by dissolving 588.08mg $CaCl_2 \cdot 2H_2O$ (MW=147.02, Chem-Supply, Adelaide) into 20ml DI water. The Ca^{2+} stock solution was subsequently diluted with DI water into 0-4mM with an interval of 0.5mM as well as 5, 6, 10, 14, 20mM, respectively. Sample for measurement was prepared by adding 50μL Calcein solution and 50μL Ca^{2+} solution into one well with proper mixing. Emission spectra were obtained between 490 and 700nm with the excitation fixed at 470nm. The gain rate set as 50 % with a read height of 8mm.

Additionally, to investigate the applicability of Calcein in a physiological environment, the Calcein emission spectra were measured in the presence of Ca^{2+} at pH 7.4. The 20mM Calcein stock solution was diluted into 0.5, 1, 1.5, 2mM with pH 7.4 PBS buffer, followed by adjusting the final pH to 7.4. The emission spectra were obtained with the identical setting as described above (for pH 12 case).

The fluorescent profiles of Calcein in varying conditions were compared to determine the optimal concentration and working environment for Calcein, where Calcein displayed the most significant fluorescence changes in response to the increasing Ca^{2+} concentration. Similarly, the optimal concentrations and working environment for Rhod-5N were identified based on the results from section 2.2.5. The optimised conditions for these two indicators were used in

section 2.2.6 and 2.2.7 for further characterisations on the selectivity and fluorescent response to Ca^{2+} in biological samples.

2.2.5 Fluorescent characterisation of Rhod-5N in response to Ca^{2+} at pH 7.4

To identify the optimal concentration and solvent for Rhod-5N as an $[Ca^{2+}]_{ex}$ indicator, the emission spectra of serial concentrations of Rhod-5N dissolved in DI water and pH 7.4 PBS buffer were measured in the presence of Ca^{2+}, respectively.

For Rhod-5N in DI water, a stock solution of 0.1mM Rhod-5N was prepared by dissolving 500μg Rhod-5N into 5.56mL DI water. The 0.1mM Rhod-5N stock solution was subsequently diluted into 5μM and 50μM with DI water. The Ca^{2+} solutions were prepared as described in 2.2.4. Sample for measurement was prepared by adding 50μL Rhod-5N solution and 50μL Ca^{2+} solution into one well with proper mixing. Emission spectra were obtained between 555 and 700nm with the excitation fixed at 535nm. The gain rate set as 50 % with a read height of 8mm.

For Rhod-5N in PBS solution, a stock solution of 1mM Rhod-5N was prepared by dissolving 500μg Rhod-5N into 0.556mL pH7.4 PBS buffer. The 1mM Rhod-5N stock solution was further diluted into 5, 10, 20, 50, 100, 250μM with pH 7.4 PBS. The sample preparation and emission spectra measurement were performed as above mentioned.

2.2.6 Fluorescent characterisations of Calcein and Rhod-5N in response to other metal ions

To study the selectivity of Calcein and Rhod-5N towards Ca^{2+}, the emission spectra of Calcein and Rhod-5N were recorded in response to various metal ions in the extracellular environment in the absence and presence of Ca^{2+}.

As shown in Table 2.2, the stock solutions of various metal ions were prepared by dissolving the corresponding salts in DI water. The stock solutions were further diluted into the sample concentrations with DI water. It is worth noting that the sample concentrations were intentionally prepared as 2 times of the ion concentrations in the extracellular environment. As the sample is 1:1 mixed with the indicator solution in the 96-well plate for fluorescence measurement, the final concentrations of ions would be the physiological concentrations in the

extracellular fluid. The fluorescence measurements were performed as described in section 2.2.4 for Calcein and 2.2.2 for Rhod-5N.

Table 2.2 | The preparation of metal ion stock solutions for investigating selectivities of Calcein and Rhod-5N to Ca^{2+}

Component	Molecular weight (g/mol)	Stock Concentration (mM)	Sample Concentration (mM)
$CaCl_2 \cdot 2H_2O$	147.02	10	2
$AlK(SO_4)_2 \cdot 12H_2O$	474.21	10	0.1
KCl	74.55	100	10
$MgCl_2 \cdot 6H_2O$	203.3	10	2
NaCl	58.44	500	300
Cl_2FeO_8	254.75	10	0.1
$Zn(ClO_4)_2 \cdot 6H_2O$	372.38	10	0.1
$MnSO_4 \cdot 4H_2O$	273.06	10	0.1
$Cu(ClO_4)_2 \cdot 6H_2O$	370.54	10	0.1

2.2.7 Fluorescent characterisations of Calcein and Rhod-5N in the presence of Ca^{2+} in cell culture medium

To confirm the sensing performance of Calcein and Rhod-5N in a physiologically relevant environment, the fluorescence of Calcein and Rhod-5N were measured in the presence of Ca^{2+} dissolved in cell culture medium at 37°C to characterise the sensing performance of the two indicators.

To prepare the Ca^{2+} solution in the cell culture medium, the 200mM Ca^{2+} stock solution was diluted into 0-4mM with Ca^{2+}-free Dulbecco's Modified Eagle Medium (DMEM) (Life Technologies, Australia). DMEM is a basal medium used in cellular biology for supporting the growth of a variety of mammalian cells and it contains various ions and nutrients such as glucose, amino acid and vitamins. The fluorescence measurements were performed as described in section 2.2.4 for Calcein and 2.2.2 for Rhod-5N

2.2.8 Data analysis

Excitation and emission spectra of indicators were averaged in duplicate measurements. The peak value of fluorescence intensities of the emission spectra was used for fluorescence analysis. Specifically, fluorescence intensities at 530nm and 580nm were determined for Calcein and Rhod-5N respectively.

The fluorescent characterisation indicated that the target concentrations of Ca^{2+} (0-2mM) induced the fluorescence quenching of Calcein (section 2.3.3) and fluorescence enhancement of Rhod-5N (2.3.4), respectively. To quantitatively characterise the fluorescent responses of the indicators, the Ca^{2+}-induced fluorescence quenching of Calcein was described by the Stern-Volmer relationship, while the K_d of Rhod-5N-Ca^{2+} interaction was computed. The Stern-Volmer relationship formulates the ratio of background fluorescence in the absence of Ca^{2+} to the fluorescence in response to Ca^{2+} (F_0/F) and the concentration of the quencher ([Qu], which is Ca^{2+} in this case). For Rhod-5N, K_d was computed with [Ca^{2+}], fluorescence in the presence of Ca^{2+} (F) and the Ca^{2+}-induced maximum fluorescence (F_{max}).

2.2.8.1 Stern-Volmer relationship for Calcein

The fluorescence quenching of a fluorophore as a function of [Qu] can be described by the Stern-Volmer equation [202]:

$$\frac{F_0}{F} = 1 + K_{SV}[Qu] \quad (Eq.\ 2.1)$$

where F_0 and F are the fluorescence intensity of a fluorophore in the absence and presence of the quencher, respectively, and K_{SV} is the Stern-Volmer quenching constant [202]. By plotting the ratio of F_0 and F of Calcein as a function of [Ca^{2+}], the quenching constant K_{SV} could be determined from the slope of the linear fitting of the graph. It is useful to note that the K_{SV}^{-1} indicates the quencher concentration at which 50% of the fluorescence is quenched (F_0/F=2).

2.2.8.2 Ionic calibration and dissociation constant of Rhod-5N - Ca^{2+} binding

The dynamic interaction between the ligand Ca^{2+} (Ca^{2+}), receptor Rhod-5N (N) and their complexed (CaN) can be expressed as:

$$CaN \Leftrightarrow Ca^{2+} + N \quad (Eq.\ 2.2)$$

According to the mass law, the equilibrium concentrations of the Ca^{2+}, [Ca^{2+}], of the Rhod-5N, [N] and of their complex [CaN] are related by K_d :

$$K_d = \frac{[Ca^{2+}] \times [N]}{[CaN]} \quad (Eq.\ 2.3)$$

In fluorescent sensing, the fluorescent signal F is proportional to the number n of bound Rhod-5N molecules (same as the bound Ca^{2+}). The value of F can be expressed as:

$$F = \varphi n \quad (Eq. 2.4)$$

where φ is the proportionality factor. At saturation, $F=F_{max}$. Therefore, the concentration of Ca^{2+} can be further expressed as:

$$[Ca^{2+}] = K_d \frac{F}{F_{max} - F} \quad (Eq. 2.5)$$

Generally, the ion concentration in fluorescent sensing refers to the ionised concentration ($[Ca^{2+}]_i$ in this case) in the solution. However, due to the shielding effect posed by the ionic environment, the available ion for binding, called effective concentration ($[Ca^{2+}]_e$), is smaller than the ionised concentration. The effective concentrations of Ca^{2+} can be calibrated with the activity coefficient in order to precisely characterise the dissociation equilibrium between Rhod-5N and Ca^{2+}. The relationship between $[Ca^{2+}]_e$ and $[Ca^{2+}]_i$ can be presented as:

$$[Ca^{2+}]_e = \gamma_i \times [Ca^{2+}]_i \quad (Eq. 2.6)$$

where γ_i is the activity coefficient, which describes the relationship between the effective concentration and the ionised concentration of an ion species under certain conditions. In an ionic solution, γ_i of a specific ion is determined by the ionic strength of the solution and the temperature of the environment. γ_i can be calculated the Davis formula [203].

$$\log(\gamma_i) = -a \times z_i^2 \left(\frac{\sqrt{I}}{1 + \sqrt{I}} - 0.3 \times I \right) \quad (Eq. 2.7)$$

where a is the coefficient constant, z_i is the valence of the ion and I is the ionic strength of the solution. The coefficient constant can be determined as:

$$a = 1.82 \times 10^6 \times (\varepsilon T)^{-3/2} \quad (Eq. 2.8)$$

where the temperature T is in Kelvin and the dielectric constant ε of water at 37°C is 74.123 [204]. Therefore, a is calculated to be 0.523. The ionic strength of the solution is expressed as [205]:

$$I = \frac{1}{2} \sum c_i z_i^2 \quad (Eq. 2.9)$$

where c_i is the ionised concentration of an ion. The ionic strength of the sample was determined to be 167.217mM based on the ionic species in the solvent for Ca^{2+} (cell culture medium) and for Rhod-5N (PBS). The final concentrations of the ionic components were listed in Table 2.3 based on the gradients of cell culture medium and PBS.

Table 2.3 | The concentrations of the ionic components

Components	Concentration (mM)
$MgSO_4$	0.407
KCl	4.017
NaH_2PO_4	0.4528
Na_2HPO_4	5.0
NaCl	123.2
$NaHCO_3$	22.02
KH_2PO_4	0.9

With the calculated a and c_i, γ_i was further calculated to be 0.3145 based on Eq. 2.7. The effective concentration of Ca^{2+} in the sample was expressed as:

$$[Ca^{2+}]_e = 0.3145 \times [Ca^{2+}]_i \quad (Eq. 2.10)$$

Therefore, Eq. 2.5 was further written as

$$F = F_{max} \times \frac{[Ca^{2+}]_e}{K_d + [Ca^{2+}]_e} \quad (Eq. 2.11)$$

The Eq. 2.11 correlates the measured fluorescence intensity F against the effective concentration of Ca^{2+}. The plot according to Eq. 2.11 was analysed by 'Hill' function under the Growth/Sigmoidal category. The model was formulated as:

$$y = V_{max} \times \frac{x^n}{k^n + x^n} \quad (Eq. 2.12)$$

where y, V_{max}, x and k correspond to F, F_{max}, $[Ca^{2+}]_e$ and K_d, respectively. n is equal to 1 for a monomer binding reaction without cooperativity to another binding site. If n is greater than 1, it indicates that there are multiple binding sites with positive cooperativity [206]

2.3 Results

2.3.1 Excitation and emission spectra of Calcein as a function of Calcein concentration at pH 7.4

The fluorometric spectra of Calcein have been reported to be significantly affected by the concentration of Calcein. Therefore, the excitation and emission spectra of Calcein were firstly examined as a function of Calcein concentration from 0.5μM to 20mM.

The excitation spectra of different concentrations of Calcein at the pH of 7.4 are shown in Fig. 2.3. It is clear that the overall excitation intensity enhanced as the concentration of Calcein increased from 0.5μM to 2mM. The excitation intensity began to drop after the concentration of Calcein was higher than 4mM (Fig. 2.3a). At low concentrations of Calcein (<5μM), the excitation spectra consisted of a major band peaking at around 495nm with a distinct shoulder on the left of the peak at around 480nm. A few minor bands were also observed at around 320nm (Fig. 2.3b).

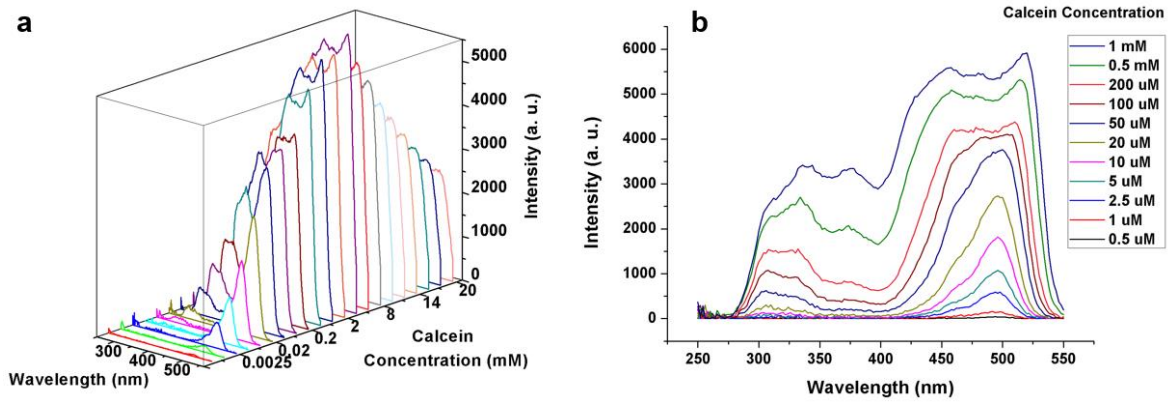

Figure 2.3 | The excitation spectra of Calcein in PBS as a function of Calcein concentration at pH 7.4. (λ_{ex} = 250-550nm, λ_{em} = 580nm) **a |** 3D plot of Calcein excitation spectra as a function of Calcein concentration; **b |** 2D plot of the excitation spectra of serial concentrations of Calcein.

The emission spectra of Calcein at pH 7.4 are shown in Fig. 2.4a, displaying a consistent overall trend of the fluorescence intensity. The spectra consisted of a single major band and a shoulder on the right of the peak at around 530nm. To further study the effect of Calcein concentration on its fluorescence, the peak fluorescence of Calcein at 530nm was plotted against the concentration of Calcein as shown in Fig. 2.4b. For the serial concentrations of Calcein at the

pH of 7.4, the fluorescence intensity of the Calcein at peak wavelength increased as the concentration increased from 0.5μM to 4mM, followed by decreasing fluorescence when the concentration increased over 4mM to 20Mm (Fig. 2.4b). Therefore, 3mM was selected for further analysis on the effect of pH on the fluorescence of Calcein to take advantage of the high fluorescence.

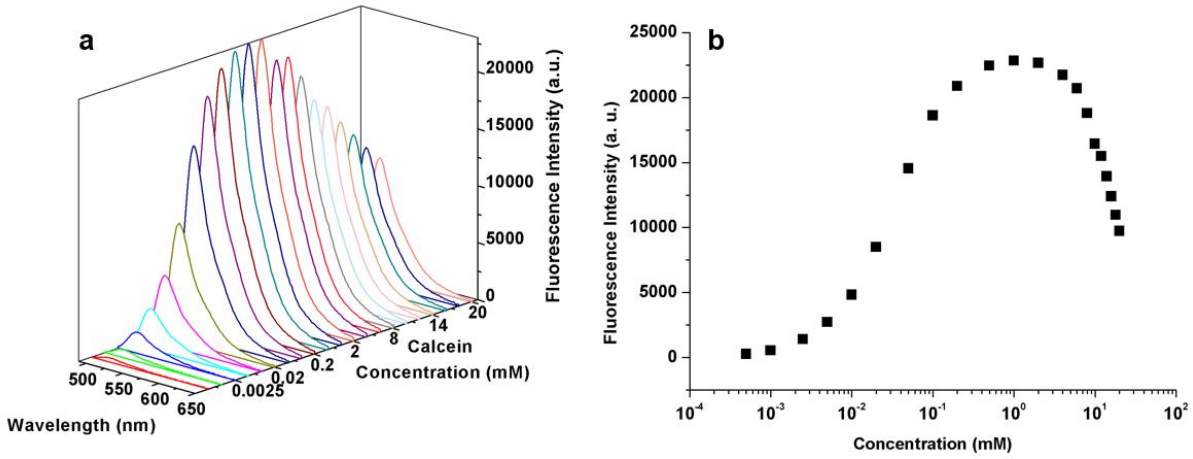

Figure 2.4 | The emission spectra of Calcein in PBS as a function of Calcein concentration at pH 7.4. **a |** 3D plot of Calcein emission spectra as a function of Calcein concentrations(λ_{ex} = 470nm, λ_{em} = 490-700nm); **b |** Fluorescence intensity of Calcein as a function of Calcein concentration (pH7.4, λ_{ex} = 470nm, λ_{em} = 530nm).

2.3.2 Excitation and emission spectra of Calcein (3mM) as a function of pH

In order to understand the effect of pH on the fluorometric properties of Calcein, the excitation and emission spectra of 3mM Calcein were measured from 250-550nm and 490-700nm, respectively, for a range of pH from 3 to 12.

The excitation spectra of 3 mM Calcein in PBS buffer are shown in Fig. 2.5 as a function of pH. The overall excitation intensity slightly increased as the pH increases from 3 to 4. The intensities remained constant between pH 4 and 10 with a redshift from 504 to 524nm. The excitation underwent a sharp drop as the pH increased from 10 to 12 and the intensity at 12 was around 6% of the intensity at pH 7 (Fig. 2.5a). It is clear in the 2D plot that 3mM of Calcein displayed a broad excitation from 300nm to 520nm and the increasing pH induced the blue shift of the peak (Fig. 2.5b).

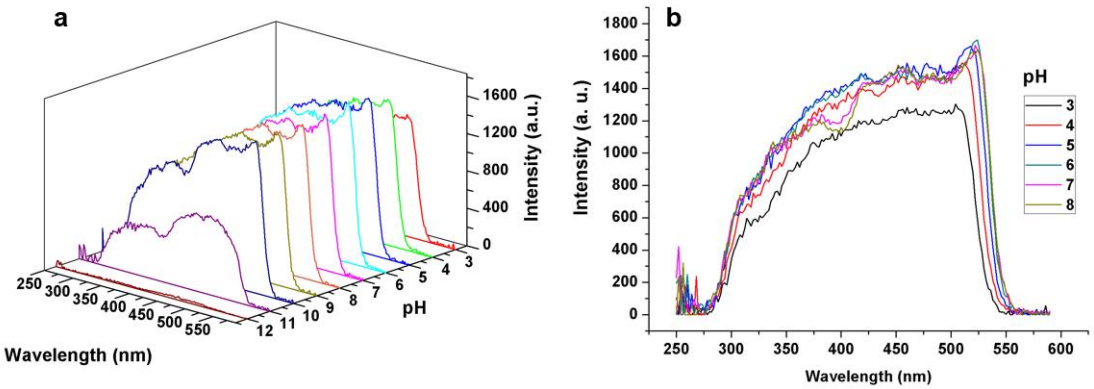

Figure 2.5 | The excitation spectra of 3mM Calcein in PBS as a function of pH. (λ_{ex} = 250-550nm, λ_{em} = 580nm) **a |** 3D plot of Calcein excitation spectra as a function of pH (3-12); **b |** 2D plot of the excitation spectra of Calcein at pH 3-8.

The emission spectra of 3mM Calcein were plotted as a function of pH as shown in Fig. 2.6. The overall trend of fluorescence intensity was slightly different from the excitation spectra. The emitted fluorescence of Calcein enhanced as the pH increased from 3 to7. From pH 8 to 10, the emission strength slightly decreased, followed by tremendous decreases in the fluorescence from at pH 11 and 12 (Fig. 2.6a). The 2D plot of the spectra shows that the peak emission of Calcein experienced blue shift with the increasing pH. Although the autofluorescence of Calcein was significantly lower at pH 12, the addition of Ca^{2+} might induce substantial change to the fluorescence at this pH condition as discussed in section 2.1.2 and 2.2.4. Therefore, it is worthwhile to investigate the Ca^{2+}-induced fluorescent response of Calcein at pH 12 in the following study.

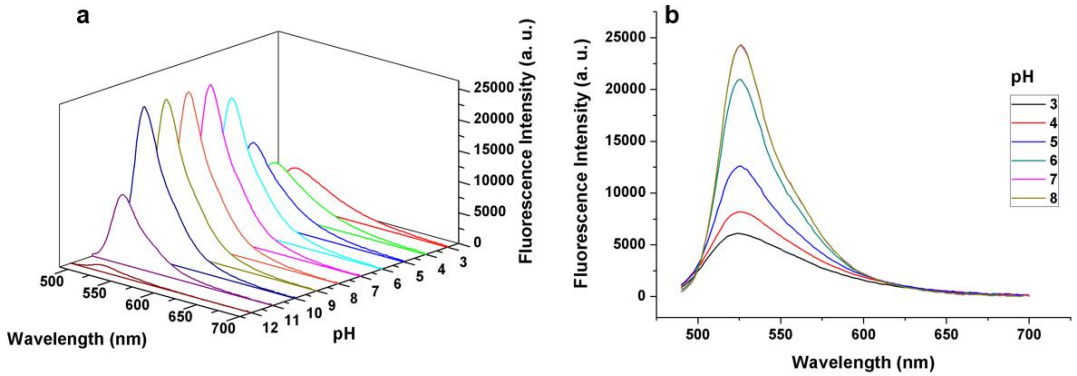

Figure 2.6 | The emission spectra of 3mM Calcein in PBS as a function of pH. (λ_{ex} = 470nm, λ_{em} = 490-700nm) **a |** 3D plot of Calcein emission spectra as a function of pH (3-12); **b |** 2D plot of the emission spectra of Calcein from pH 3-8.

2.3.3 Effect of indicator concentration, pH and temperature on the fluorescence of Calcein in response to Ca^{2+}

To determine an optimal working condition for Calcein as an indicator for extracellular Ca^{2+}, the fluorescence of serial concentrations of Calcein was measured in the presence of 0-2mM Ca^{2+} in an alkaline environment (pH 12) and physiologically relevant environment (pH 7.4), respectively.

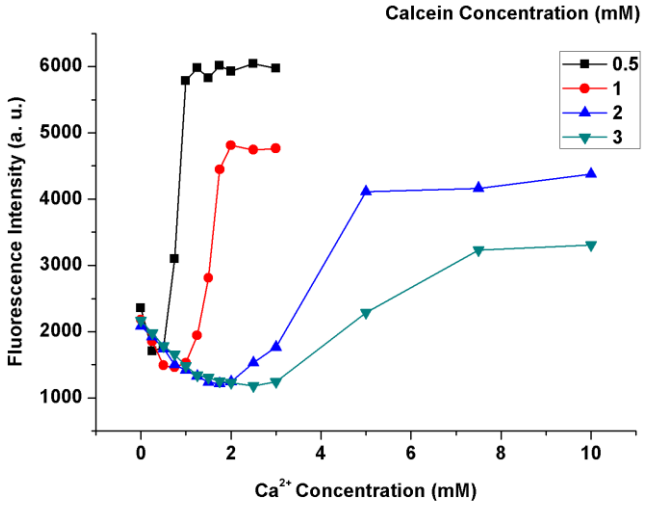

Figure 2.7 | The fluorescence intensity of serial concentrations of Calcein as a function of Ca^{2+} concentration at pH 12. (λ_{ex} = 470nm, λ_{em} = 530nm)

As discussed in the previous sections, the ratio between Calcein and Ca^{2+} was set approximately as 1:1. Considering the fluorescence quenching shown in the higher Calcein concentration might affect its sensitivity to Ca^{2+}, the Ca^{2+}-induced fluorometric response of Calcein was investigated with a wider range of Calcein (0.5-3mM) instead of only using 3mM to determine the optimal concentration of Calcein. In this context, the emission profiles of 0.5, 1, 2 and 3mM Calcein were examined with addition of increasing Ca^{2+} at pH 12. As shown in Fig. 2.7, Calcein at pH 12 exhibited ratio-dependent fluorescent signals in response to Ca^{2+}. The fluorescence of Calcein (pH 12) decreased when the ratio of Ca^{2+} to Calcein increased from 0 to 1 and the fluorescence increased when the ratio increased over 1. The fluorescence of Calcein reached a plateau when the ratio was between 2-2.5. Consequently, the lower concentration of Calcein (<2mM) showed reversed fluorescence signals from fluorescence quenching to

fluorescence enhancement in the presence of target Ca^{2+} (0-2mM), which justified the necessity to use higher concentrations of Calcein (>2mM). It is worth noting that 2mM Calcein displayed fluorescence quenching in response to 0-1.5mM Ca^{2+} and reached to a minimum fluorescence between 1.5-2mM Ca^{2+}. Compared with 2mM of Calcein, the 3mM Calcein was more responsive to the target Ca^{2+} by showing continuous fluorescence quenching in response to 0-2mM Ca^{2+}. Therefore, 3mM Calcein was selected for the following experiments without further investigation on a higher Calcein concentration (>3mM), which might compromise the sensitivity of Calcein to Ca^{2+} due to enhanced self-quenching.

The temperature has been shown to be an important factor for fluorescence quenching [207]. As most preliminary fluorescence measurements were carried out in plate reader at room temperature, varying from the physiological conditions, i.e., 37°C in the body, the fluorescence of 3mM Calcein at room temperature (23°C) and 37°C in the presence of various [Ca^{2+}] were compared at pH 12. As shown in Fig. 2.8, although the fluorescence intensities at 37°C were lower than that of at room temperature, the Ca^{2+}-induced fluorescence quenching of Calcein was retained at both temperatures with almost identical quenching tendency as the increase of [Ca^{2+}]. This comparison demonstrates that the evaluation results on Calcein at room temperature are meaningful.

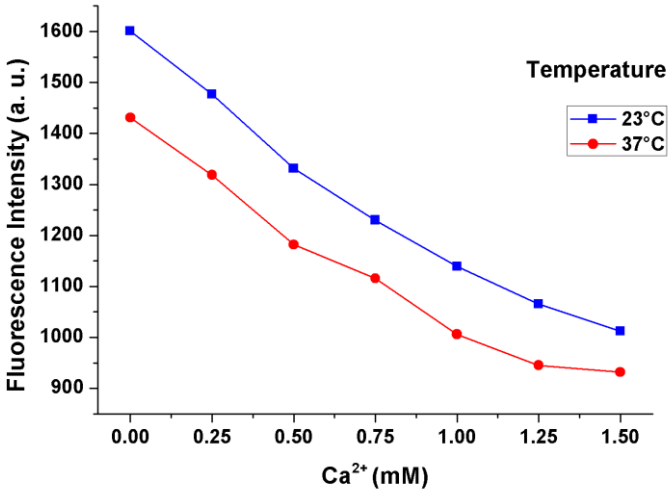

Figure 2.8 | The Ca^{2+}-induced fluorescence quenching of 3mM Calcein at room temperature and 37°C at pH 12. (λ_{ex} = 470nm, λ_{em} = 530nm)

As the Calcein is expected to be used in the biological environment, the fluorescence measurements of serial concentrations of Calcein were measured at pH 7.4 in the presence of various [Ca^{2+}]. As shown in Fig. 2.9, the emission spectra of 5μM Calcein displayed undistinguishable change with the addition of Ca^{2+} in terms of the intensity and peak wavelength; for the spectra of 50μM, 0.5mM and 2mM Calcein, the slight intensity drop and minor blue shift of peak wavelength were observed with increasing [Ca^{2+}]. For example, for 2mM Calcein at pH 7.4, the largest fluorescence quenching caused by 2mM Ca^{2+} was less than 8% on the basis of the background fluorescence in the absence of Ca^{2+} at around 526nm emission. These results confirm that the use of Ca^{2+}-induced quenching of Calcein indicator is only feasible at the alkaline environment (pH 12) instead of the physiologically relevant environment (pH 7.4).

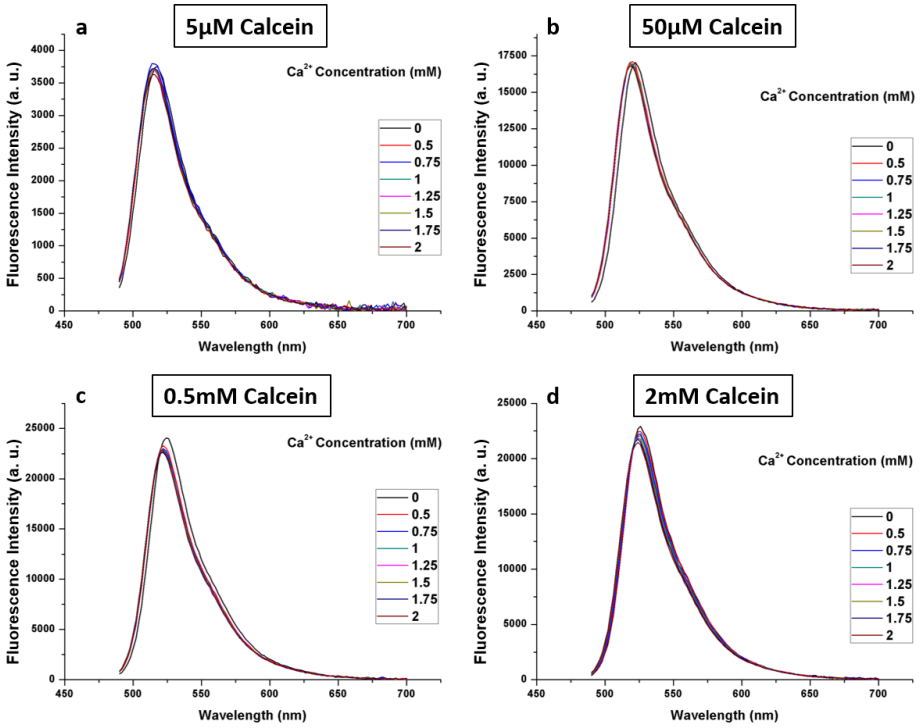

Figure 2.9 | The emission spectra of 5μM, 50μM, 0.5mM and 2mM Calcein in the presence of Ca^{2+} at pH 7.4. (λ_{ex} = 470nm, λ_{em} = 490-700nm)

2.3.4 Stern-Volmer relationship between the fluorescence of Calcein and Ca^{2+} concentration

As discussed in 2.2.8, the Stern-Volmer relationship provides insight into the quenching degree of Calcein by [Ca^{2+}]. In this work, the Stern-Volmer relationship of F_0/F versus [Ca^{2+}] was

plotted for 3mM Calcein in the presence of 0-1.5mM Ca^{2+}, where F_0 and F were the fluorescence intensities in the absence and presence of Ca^{2+}, respectively, dissolving in the cell culture medium at 37°C. As shown in Fig. 2.10, the Stern-Volmer quenching constant K_{SV}, revealed by the slop of the linear fitting of the data points, was 0.413L/mM. The K_{SV} indicated that the addition of 0.1mM Ca^{2+} induces a 3.94% fluorescence drop and 2.43mM Ca^{2+} would cause about 50% fluorescence quenching of Calcein, where F_0/F was equal to 2. However, as the concentration of Ca^{2+} increased over 2mM, the fluorescence quenching of 3mM Calcein was reversed. Therefore, the Ca^{2+}-induced fluorescence quenching of 3mM Calcein was expressed as Eq. 2.13 (applicable for [Ca^{2+}] below 1.5mM). The maximum fluorescence quenching of 3mM Calcein was around 50% in this experiment.

$$\frac{F_0}{F} = 1 + 0.413L/mmol \times [Ca^{2+}] \quad (Eq.\,2.13)$$

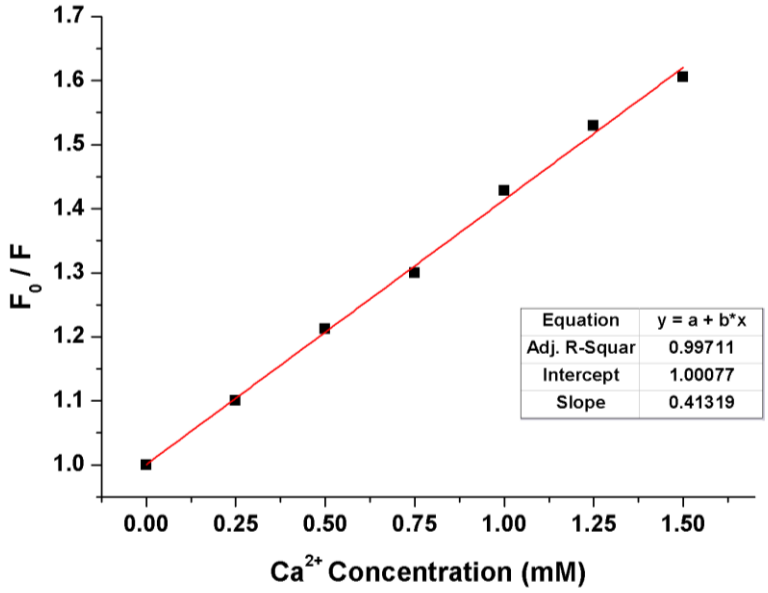

Figure 2.10 | Ca^{2+} Stern-Volmer plot for Calcein as a function of Ca^{2+} concentration. (λ_{ex} = 470nm, λ_{em} = 530nm) F_0 and F were the fluorescence of Calcein in the absence and presence of Ca^{2+}, respectively.

2.3.5 Effect of solvent and indicator concentration on the fluorescence of Rhod-5N in response to Ca^{2+}

As demonstrated in 2.1.2 section, in comparison to Calcein indicator, the fluorometric properties of Rhod-5N are stable at different pH [95]. Moreover, Rhod-5N indicator is essentially

non-fluorescent in the absence of Ca^{2+}. However, it was reported that the binding affinity of Rhod-5N to Ca^{2+} was significantly affected by the ionic strength of the solution. Thus, the effective Ca^{2+} sensing range could be influenced by the concentration of Rhod-5N and the ionic strength of the solvent used in the experiment.

The emission spectra of Rhod-5N (2.5μM and 25μM Rhod-5N dissolved in DI water, respectively) were first measured in the presence of various [Ca^{2+}]. As shown in Fig. 2.11a, the emission of Rhod-5N consisted of a major band peaking at around 580nm, accompanied by a shoulder around 610 to 640nm. With the addition of Ca^{2+} from 0.25mM to 2.5mM, the fluorescence intensities at peak wavelength were amplified up to over 100 times of the background fluorescence. Fig. 2.11b shows that the fluorescence intensity reached a plateau as the Ca^{2+} increased over 0.25mM for 2.5μM Rhod-5N and 1.25mM for 25μM Rhod-5N, suggesting the concentration of Rhod-5N positively correlated with the sensing range of Ca^{2+} in a certain indicator range.

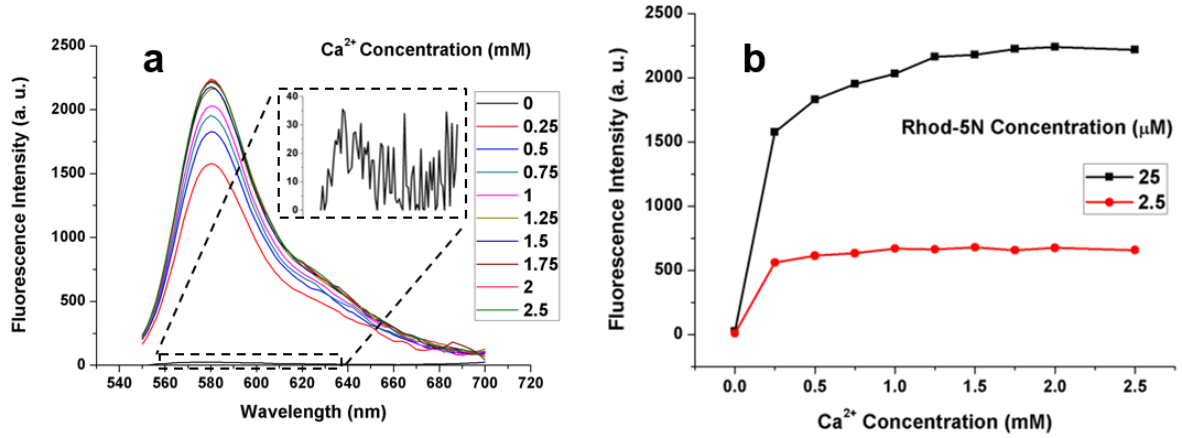

Figure 2.11 | The fluorescence of Rhod-5N in water in response to Ca^{2+}. a | The emission spectra of 25μM Rhod-5N in the presence of Ca^{2+}. The inset shows the background fluorescence of Rhod-5N in the absence of Ca^{2+} (λ_{ex} = 535nm, λ_{em} = 555-700nm); **b |** The Ca^{2+}-induced fluorescence enhancement of 2.5μM and 25μM Rhod-5N in DI water (λ_{ex} = 535nm, λ_{em} = 580nm).

To understand the effect of ionic strength of the solution on the fluorescence of Rhod-5N, the spectra of 25μM Rhod-5N dissolved in pH 7.4 PBS buffer and DI water were compared. As shown in Fig. 2.12a, with the same indicator concentration, the Rhod-5N dissolved in PBS displayed a suppressed fluorescence increment, which suggested that the ionic strength of the solution negatively correlated with the Ca^{2+}-Rhod-5N binding. Furthermore, to identify the

optimal concentration of Rhod-5N for [Ca^{2+}] measurement, the emission spectra of a large range concentration of Rhod-5N were examined as a function of various [Ca^{2+}]. As shown in Fig. 2.12b, for Rhod-5N around 50-100μM, there was the largest fluorescence enhancement for the target [Ca^{2+}] (0-2mM). Therefore, 50μM Rhod-5N would be used as the final concentration in the sample.

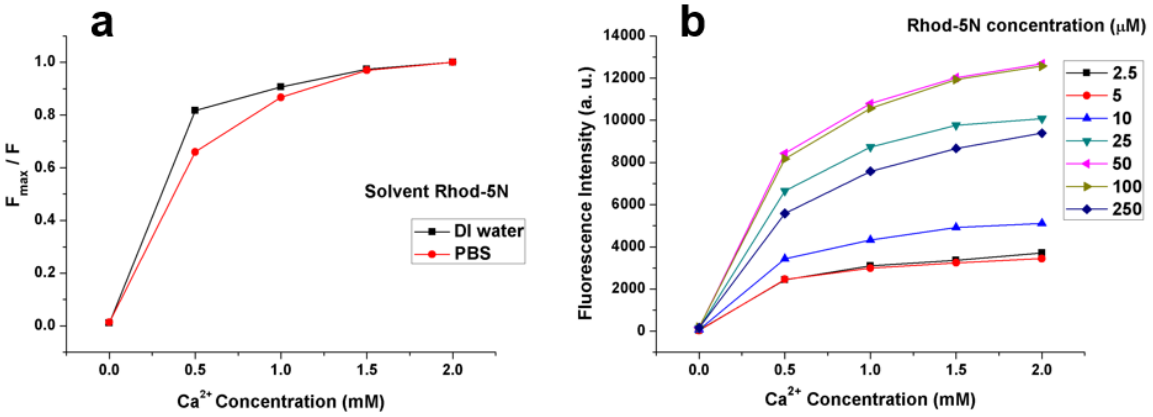

Figure 2.12 | The fluorescence of Rhod-5N in pH 7.4 PBS solution in the presence of Ca^{2+}. (λ_{ex} = 535nm, λ_{em} = 580nm) **a |** The fluorescence intensities of 25μM Rhod-5N dissolved in DI water and PBS, respectively, in the presence of various [Ca^{2+}] (0-2mM). (F_{max} was the maximum fluorescence intensity of Rhod-5N induced by Ca^{2+} (2mM) and F was the fluorescence intensity at a specific concentration of Ca^{2+}); **b |** The fluorescence enhancement profiles for serial concentrations of Rhod-5N (from 2.5μM to 250μM) as a function of [Ca^{2+}].

2.3.6 Selectivity of Calcein and Rhod-5N to Ca^{2+} over other metal ions in extracellular fluid

Fig. 2.13a indicates that Ca^{2+} induces a major fluorescence quenching of Calcein under physiological conditions (first column labelled with Ca^{2+}). The Ca^{2+}-induced fluorescence quenching was more than 3 times higher than that by Mg^{2+}, K^{+}, Fe^{2+}, Cu^{2+} and Al^{3+} ions. While the presence of Na^{+} or Zn^{2+} led to an increase in fluorescence intensity, the addition of 1mM Ca^{2+} led to the dominant fluorescence reductions.

Fig. 2.13b shows that Rhod-5N exhibited a high selectivity to Ca^{2+}. The 50μM Rhod-5N was non-fluorescent in the presence of Mg^{2+}, Na^{+}, K^{+}, Fe^{2+} and Al^{3+} and the addition of 1mM Ca^{2+} induced the increase of the fluorescence intensity over 40 times. Nevertheless, the presence of

Cu^{2+} and Zn^{2+} induced a minor increase of the fluorescence, and more importantly, their existence significantly suppressed the Ca^{2+}-induced fluorescence enhancement.

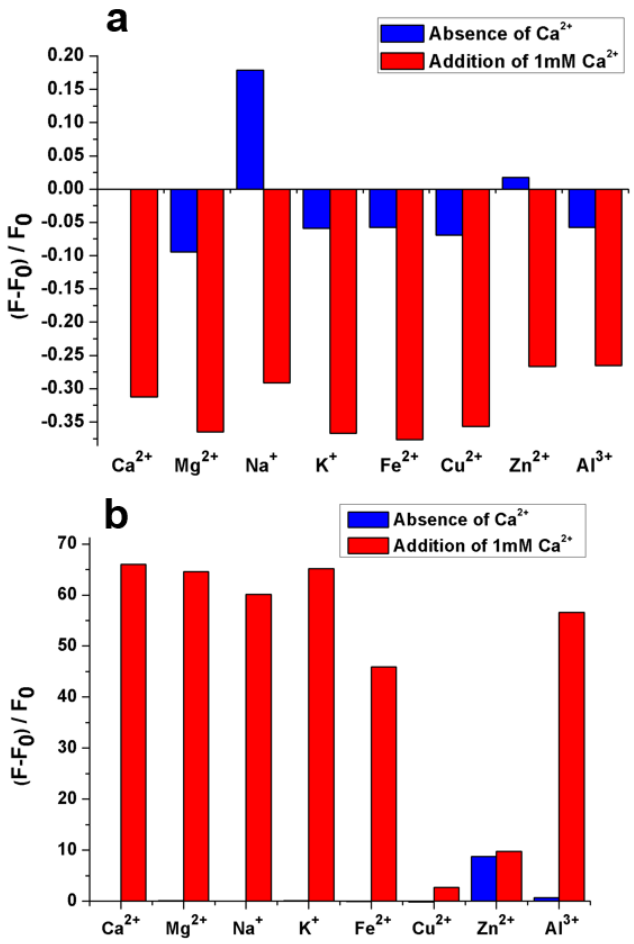

Figure 2.13 | The fluorescence of Calcein and Rhod-5N in the presence of Ca^{2+} and other metal ions in extracellular fluid. a | The selectivity profile of 3mM Calcein in pH 12 PBS buffer (λ_{ex} = 470nm, λ_{em} = 530nm); **b |** The selectivity profile of 50μM Rhod-5N in pH 7.4 PBS buffer (λ_{ex} = 535nm, λ_{em} = 580nm). F_0 and F were the fluorescence of the indicators in the absence and presence of Ca^{2+}, respectively. The blue bar shows the fluorescence of the indicator in the presence of the single ion without Ca^{2+} and the red bar shows the fluorescence with the addition of 1mM Ca^{2+}. The concentrations of each ion were set as their approximate concentrations in extracellular environment (Ca^{2+} 1mM, Mg^{2+} 1mM, Na^{+} 150mM, K^{+} 5mM, Fe^{2+} 50μM, Cu^{2+} 50μM, Zn^{2+} 50μM, Al^{3+} 50μM).

To investigate whether the presence of Zn^{2+} and Cu^{2+} would affect the Ca^{2+} sensing capability of Rhod-5N, the full-ion solution containing all the above mentioned physiologically relevant metal ions were prepared with the corresponding concentrations. The concentrations of Ca^{2+} in the full-ion solution were adjusted to 0, 1, 2, 3, and 4mM, respectively. As the prepared Ca^{2+}

solution was 1:1 mixed with Rhod-5N solution (100μM), the final concentration of Rhod-5N was 50μM and the concentrations of Ca^{2+} were 0, 0.5, 1, 1.5 and 2mM, respectively, in the measurement. As shown in Fig. 2.14a, in the presence of physiologically relevant metal ions, 50μM Rhod-5N showed the fluorescence increment in response to increasing concentration of Ca^{2+} from 0 to 2mM. Moreover, by dissolving Ca^{2+} in full-ion solution, the fluorescence change in response to Ca^{2+} variations turned out to display higher linearity, improving from 0.714 (nonlinear, Ca^{2+} dissolved in DI water) to 0.978 (linear). Due to the presence of Cu^{2+} and Zn^{2+}, the fluorescence enhancement factors of Rhod-5N in response to varying [Ca^{2+}] was reduced, but Cu^{2+} and Zn^{2+} did not affect the excellent capability of Rhod-5N sensing Ca^{2+} (Fig. 2.14b).

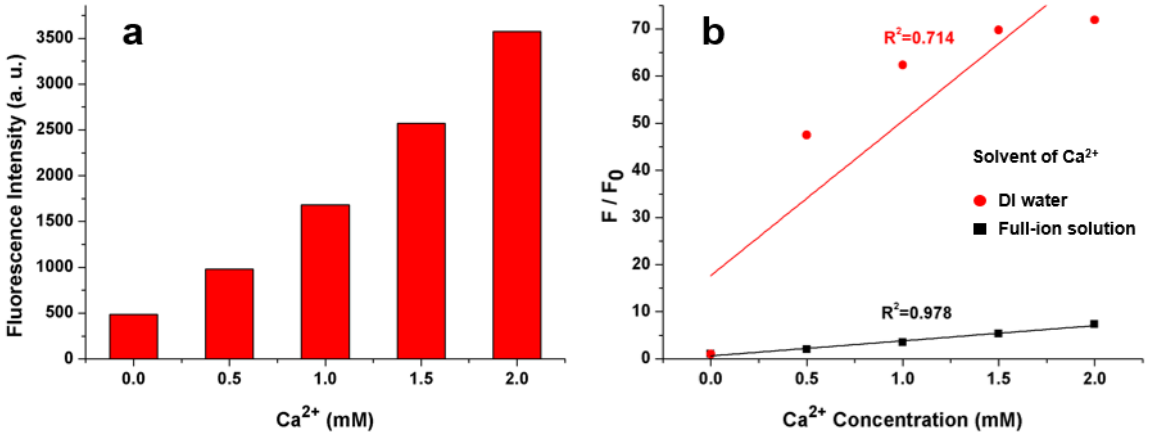

Figure 2.14 | The effect of metal ions the fluorescence enhancement of Rhod-5N in response to Ca^{2+}. (λ_{ex} = 535nm, λ_{em} = 580nm) **a |** The fluorescence of 50μM Rhod-5N in the presence of Ca^{2+} in full-ion solution; **b |** The linearity of the fluorescence intensity of 50μM Rhod-5N in response to Ca^{2+} DI water (red) and in full-ion solution (black). F_0 and F were the fluorescence of the indicators in the absence and presence of Ca^{2+}, respectively.

2.3.7 Dissociation constant of Rhod-5N – Ca^{2+} binding

As discussed in 2.2.8, the dissociation constant (K_d) of Rhod-5N to Ca^{2+} can be determined by modelling the correlation between Ca^{2+}-induced fluorescence intensity and the corresponding [Ca^{2+}]. In this experiment, the fluorescence intensities of Rhod-5N were plotted against the corresponding effective [Ca^{2+}] from 0.3145nM to 0.3145 M. As shown in Fig. 2.15, Hill plot equation was computed to be:

$$y = 32068.213 \times \frac{x}{0.000719 + x} \quad (Eq.\,2.14)$$

As *k* in Eq. 2.14 corresponds to the K_d in Eq. 2.11, the K_d of Rhod-5N and Ca^{2+} interaction was determined to 0.719mM in cell culture medium at 37°C. Therefore, the optimal Ca^{2+} sensing range of 50μM Rhod-5N was 71.9μM to 7.19mM (correspond to 0.1~10 K_d, the range was visualised by the two vertical dashed lines in Fig. 2.15), during which Rhod-5N displayed a relatively linear fluorescence enhancement.

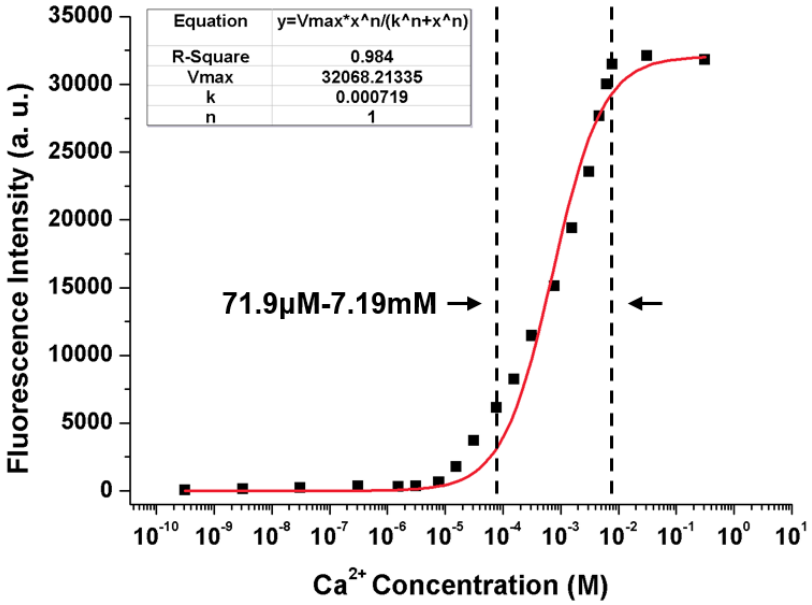

Figure 2.15 | Ca^{2+} titration curve of Rhod-5N (50μM) measured from the emitted fluorescence intensity of Rhod-5N at 580nm. (λ_{ex} = 535nm, λ_{em} = 580nm) The optimal Ca^{2+} sensing range was visualised by the two vertical dashed lines, corresponding to 0.1~10 K_d.

2.4 Discussion

In this chapter, two commercially available fluorescent Ca^{2+} indicators, Calcein and Rhod-5N, were systematically evaluated for sensing $[Ca^{2+}]_{ex}$. It was found that the 3mM Calcein indicator dissolved in pH 12 PBS buffer experienced a fluorescence quenching as $[Ca^{2+}]$ increases from 0 to 2mM in both DI water and cell culture medium. The Stern-Volmer plot indicated a 3.97% fluorescence intensity drop was achieved by adding 0.1 mM Ca^{2+}. Moreover, Calcein was highly selective to Ca^{2+} over other major and trace metal ions in the extracellular environment.

On the contrary, Ca^{2+} induced significant fluorescence enhancement of 50μM Rhod-5N in pH 7.4 PBS, where the intensity was amplified over 72 times in the presence of 2mM Ca2+. Although the Ca^{2+}-induced fluorescence of Rhod-5N was significantly suppressed in the

presence of *in vivo* Cu^{2+} or Zn^{2+} ions (50 μM each), the fluorescent signals improved with the higher linearity in all-ions solution and remain sufficient for accurately quantifying [Ca^{2+}] dynamics. In all-ions solution, Rhod-5N retained the ultra-sensitive response to the variations of [Ca^{2+}], i.e., ΔF = 36.8 % per 0.1mM of Ca^{2+} (Table 2.4).

Table 2.4 | Comparison of Calcein and Rhod-5N for sensing $[Ca^{2+}]_{ex}$

Properties/Conditions	Calcein	Rhod-5N
Concentration	3mM	50μM
pH	12	7.4
$(F_{max} - F_0) / F_0$	-0.48	72
ΔF (per 0.1mM Ca^{2+})	3.97%	36.8%
Interference	Na^+	Cu^{2+}, Zn^{2+}

The quenching of Calcein, for the first time, was utilised to establish a quantitative method for measuring $[Ca^{2+}]_{ex}$. Calcein is known to undergo fluorescence quenching either in high Calcein concentration due to self-quenching or in the presence of certain metal ions at pH7.4, where Calcein displayed a strong background fluorescence [190]. It is worth noting that the mechanisms underlying these two quenching phenomena are different. While the self-quenching observed in a high concentration of Calcein was owing to the dynamic quenching via an increasing collision between Calcein molecules [208], the metal ion-induced fluorescence quenching was attributed to the static quenching by forming non-fluorescent complexes [193]. As shown in Fig. 2.8, at the same Ca^{2+} concentration, the fluorescence quenching of Calcein was enhanced at a higher temperature, suggesting that the accelerated diffusion at a higher temperature led to a higher probability of collisional quenching. Interestingly, the slope of fluorescence quenching was relatively independent of experimental temperatures. Further experiment is required to determine the mechanism underlying the Ca^{2+}-induced fluorescence quenching of Calcein, such as investigating the effect of Ca^{2+} on the fluorescence lifetime of Calcein.

In this work, the Ca^{2+}-induced fluorescence quenching of Calcein is hypothesised to be achieved by the positive effect of Ca^{2+} on the aggregation of Calcein. It is known that Calcein-Ca^{2+} interaction results in a complex with enhanced fluorescence. Therefore, the Ca^{2+}-induced fluorescence quenching of Calcein was unlikely to be caused by static quenching, which resulted from the formation of non-fluorescent complex [202]. At high Calcein concentration (>2mM), the increasing aggregation of Calcein induced the self-quenching of Calcein by enhancing the collisions between Calcein molecules. As Ca^{2+} was added into the solution, Ca^{2+}

interacted with the Calcein and they form a fluorescent complex. However, when Ca^{2+} was much lower than Calcein (Ca^{2+}/Calcein<0.5), a small amount of the fluorescent complex was formed, but only insignificant fluorescence was produced. Meanwhile, the interaction with Ca^{2+} alleviated the electrical repulsion between the negatively charged Calcein molecules, leading to the increased aggregation and a higher probability of collision. The self-quenching further enhanced under the higher collision rate. As the increased self-quenching surpassed the fluorescence enhancement, the overall trend of fluorescence change was quenching at this stage (Calcein > 0.5mM, Ca^{2+}/Calcein < 0.5). As the ratio of Ca^{2+} to Calcein reached up to around 0.5-1, the increasing amount of Ca^{2+}-Calcein complex neutralised the self-quenching of Calcein and boosted the overall fluorescence intensity. Therefore, the increasing [Ca^{2+}] diminished the fluorescence quenching (0.5 < Ca^{2+}/Calcein < 1), followed by a significant fluorescence enhancement (Ca^{2+}/Calcein > 1).

Compared with the previous methods for serum Ca^{2+} quantification using Calcein, the method presented here did not require the dilution of the samples so that the measurement was simplified by mixing the ions sample and indicator solution. However, the alkaline working environment of Calcein would restrict its biological applications.

By contrast, the application of Rhod-5N is well compatible with the physiological environment. In the presence of 0-2mM Ca^{2+}, Rhod-5N displayed the significant fluorescence increase at 7.4 pH (physiological condition). Moreover, Rhod-5N exhibited a high selectivity to Ca^{2+} over other metal ions that were commonly found in the interstitial fluid. Additionally, the optimal concentration of Rhod-5N (50μM) identified in this work was significantly lower than the micro-tip probe for $[Ca^{2+}]_{ex}$ recording, where 3mM Rhod-5N was employed. Although Cu^{2+} and Zn^{2+} were shown to suppress the Ca^{2+}-induced fluorescence of Rhod-5N, interference from Cu^{2+} or Zn^{2+} was less likely to cause a major issue as their concentrations are relatively stable during biological events. If necessary, the Cu^{2+} and Zn^{2+} can be depleted by applying Zn^{2+} and Cu^{2+} chelators, such as *N*, *N*, *N*′, *N*′ -tetrakis(2-pyridylmethyl)ethylenediamine (TPEN) or diethylenetriaminepentacetic acid (DPTA) [209,210].

In conclusion, the comprehensive comparisons between Calcein and Rhod-5N suggested that Rhod-5N showed advantages over Calcein for sensing $[Ca^{2+}]_{ex}$ in terms of fluorescent signal strength, indicator consumption, selectivity to Ca^{2+} and biocompatibility. Therefore, Rhod-5N was used in the following study to be incorporated into the microfluidic system.

Chapter 3

Design, fabrication and characterisation of a microfluidic chip for tissue secretion analysis

This chapter describes the fundamental fluidic physics at microscale that are essential to the rational design of a microfluidic chip and its prevalent fabrication using soft lithography. In order to develop a microfluidic device for tissue secretion analysis, a microfluidic chip was designed with the capabilities of manipulating the stimulation, immobilising tissues, fluorescent sensing and continuous collection of the tissue effluent. Both theoretical simulations and experimental tests were performed to characterise the fluid dynamics in the microfluidic chip, including the flow regime, mixing efficiency and input control. Tissue trapping efficiency was also studied by simulating the tissue loading with microspheres.

3.1 Background

3.1.1 Fundamentals of fluid dynamics at microscale

To design and fabricate a microfluidic chip suitable for biological application, it is essential to know the correlation between the dimension of the micro-geometry of the chip and the fluid dynamics. In general, three fundamental aspects should be considered: (i) the concept of flow regime and different flow types; (ii) the diffusion feature of molecules in a microfluidic channel; (iii) the flow rates in different branches of a microfluidic chip.

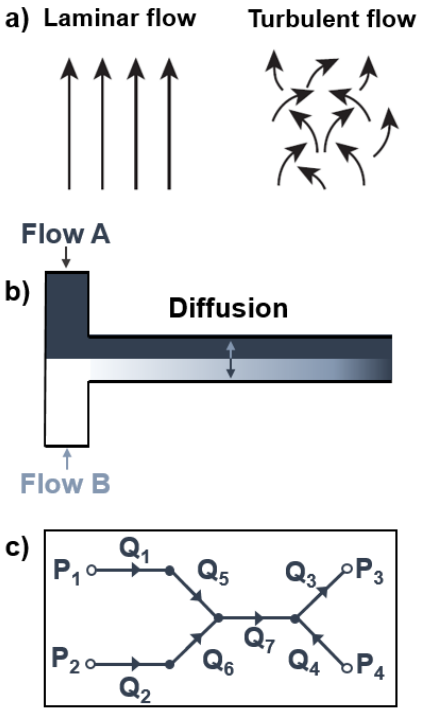

Figure 3.1 | Three typical fundamental aspects of fluid dynamics in microscale channels. a | Fluidic features of laminar flow and turbulent flow [211]; **b |** Molecules diffusion between two co-flow laminar flows, where the diffusion and mixing degree of two flows are enhanced with the increase of the co-flow length [212]. **c |** Stick diagram of a microfluidic model where the arrows indicate the fluidic flow in each branch [213].

3.1.1.1 Reynolds number and flow regimes

Fluid regimes are classified into two major types, laminar flow and turbulent flow, based on the fluidic features (Fig. 3.1a) [214]. Specifically, laminar flow consists of parallel flow streams, leading to highly stable and predictable fluid behaviours. On the contrary, the random fluctuation in turbulent flow produces unpredictable flow patterns such as eddies and vortices [213]. The fluid flow type in a pipe is determined primarily by a dimensionless quantity called Reynolds number (Re), which is defined as:

$$Re = \frac{\rho v D_h}{\mu} \quad (Eq. 3.1)$$

where ρ is the density of the fluid [kg/m^3], v is the average flow velocity [m/s], D_h is the hydraulic diameter of the channel [m], μ is the viscosity of the fluid [kg/m•s]. The hydraulic diameter is calculated by:

$$D_h = \frac{4A}{U} \quad (Eq.\,3.2)$$

where A is the area of a cross-section of the channel [m^2], U is the wetted perimeter [m] [215]. As shown in Table 3.1, the hydraulic diameter of a microfluidic channel can be further expressed based on the shape of the cross-section.

Table 3.1 | The hydraulic diameter of different shapes of microfluidic channels

Cross-section shape	Parameter	Hydraulic Diameter (D_h)
Circle	Radius (R_C), diameter (d)	$D_{hc} = \frac{4 \bullet \pi \bullet {R_C}^2}{\pi \bullet d} = d \quad (Eq.\,3.3)$
Square	Length (l)	$D_{hs} = \frac{4 \bullet l^2}{4 \bullet l} = l \quad (Eq.\,3.4)$
Rectangle	Length (l), height (b)	$D_{hr} = \frac{4 \bullet l \bullet b}{2 \bullet (l + b)} = \frac{2 \bullet l \bullet b}{l + b} \quad (Eq.\,3.5)$

According to the fluid mechanics, the flow is laminar if the Reynolds number is less than 2100, and is turbulent when the Reynolds number is greater than 4000 [216]. When the Reynolds number ranges from 2100 to 4000, the flow is described as transitional. Due to the microscale dimension of the channel and low fluidic velocity, flows in microfluidic chips generally have low Reynolds numbers and, therefore, are laminar.

3.1.1.2 Molecules diffusion

In the context of laminar flow, the mixing of molecules occurring in a microfluidic channel is predominantly dictated by diffusion. When mixing two solutions in a microfluidic channel, a group of molecules in the concentrated solution, by Brownian motion, spread out over time (Fig. 3.1b) [212]. During the mixing process, the distance (d) that a molecule can travel is related to the diffusion coefficient (D) and the time for travelling (t). The relationship can be described as:

$$d^2 = 2Dt \quad (Eq.\,3.6)$$

As shown in Table 3.2, D of molecules related to this work has been reported in the literature. Alternatively, it can also be calculated by the Stokes-Einstein equation:

$$D = \frac{kT}{6\pi r\mu} \quad (Eq.3.7)$$

where k is the Boltzmann constant, r is the hydrodynamic radius of the molecule.

The diffusion in a microfluidic channel is a spreading process over time. The relationship between D and the mixing time (τ) to achieve the homogeneous distributions, and a channel width w is characterised as [217]:

$$\tau \sim \frac{w^2}{D} \quad (Eq.3.8)$$

Assuming two laminar fluids are carried with velocities (v):

$$v = \frac{Q}{w \times h} \quad (Eq.3.9)$$

where Q is the volumetric flow rate. The necessary length (L) for thorough mixing of the two streams can also be estimated based on Eq. 3.8 and 3.9:

$$L \approx \frac{Qw}{hD} \quad (Eq.3.10)$$

As Eq. 3.10 suggests: (1) only fluids flow through channel length L, the concentrations of the molecules become constant across the entire cross-section of the channel (complete mixing); (2) the channel length L required for a complete mixing increases with an increasing ratio between the width and height of the channel or vice versa.

3.1.1.3 Flow rate in the branched channels

For microfluidic chips with constant flows driven by external pumps, the flow rate in each branched channel is determined by the mass conservation. As shown in Fig. 3.1c, three input flows of this conceptual microfluidic structure are pumped into the canals via port 1, 2, 4 (P_1, P_2, P_4) with flow rates Q_1, Q_2 and Q_4 respectively. Port 3 (P_3) is set as the outlet. Based on the mass conservation law, the flow rates of the fluids, in this case, obey the following relationship:

$$Q_1 = Q_5,\ Q_2 = Q_6 \quad (Eq.\ 3.11)$$

$$Q_7 = Q_5 + Q_6,\ Q_3 = Q_7 + Q_4 \quad (Eq.\ 3.12)$$

3.1.2 Fabrication of microfluidic device via soft lithography

Soft lithography refers to the application of photolithography on manufacturing a two-part polymer (elastomer and curing agent), most notably PDMS, with photoresist master. Soft lithography enables the manufacture of chip structures with lateral dimensions of 1-1000μm and vertical dimensions from 100nm to hundreds of microns [218]. The competency of precisely fabricating various structures at microscale has facilitated the development of various microfluidic devices for a wide range of biological studies.

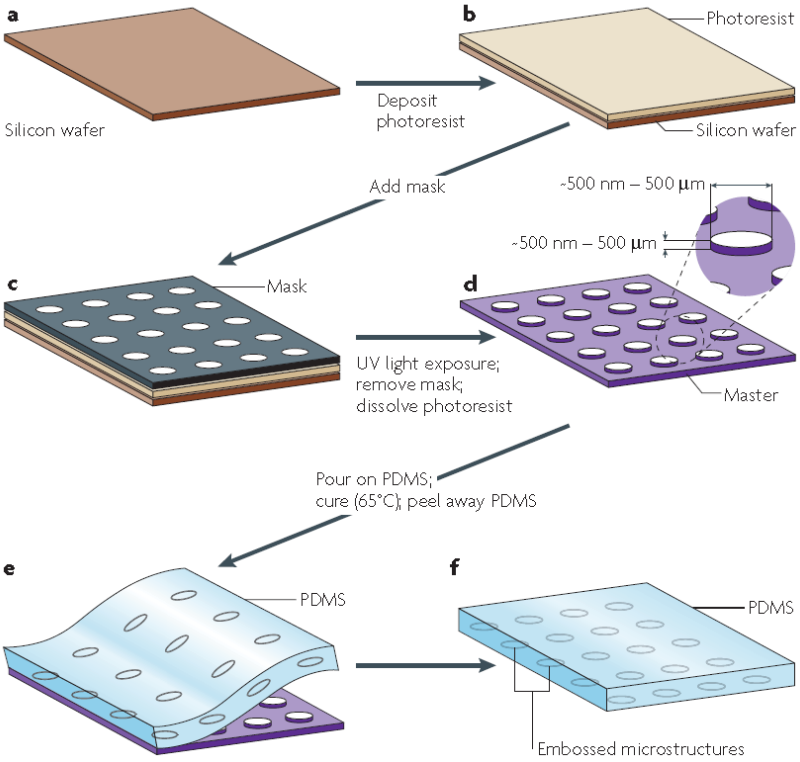

Figure 3.2 | The procedure of the fabrication of microstructures via soft lithography [218]. a | A silicon wafer is prepared as the substrate; **b |** Light-sensitive photoresist is coated on the substrate; **c |** Proposed microstructure is written on the mask, which is placed on the photoresist; **d |** When exposed to UV light, the solubility of the photoresist changes and the unnecessary part is removed by the developer; **e |** PDMS is poured on the mould and cured to form the structure; **f |** A PDMS embossed with designed structure is fabricated and it can be easily replicated with the mould.

The overall procedure of soft lithography is shown in Fig. 3.2. Once the proposed design of a chip is determined, the structure pattern is drawn in a computer-aided design (CAD) software. The pattern is then transferred onto a transparent mask by printing on a polymer matrix or laser/electron-beam writing on a glass substrate. The mask is then placed on the top of a silicon wafer (or glass slide) coated with a layer of photoresist (Fig. 3.2a-c). When exposed to UV light, the photoresist undergoes photochemical reaction, which affects the solubility of the photoresist. The light exposure makes the positive photoresist more soluble and the negative photoresist less soluble. Photoresist solvent, called developer, is then used to dissolve the radiated or non-radiated photoresist to form a master mould, which has the opposite pattern of designed structure (Fig. 3.2d). The as-prepared PDMS is poured onto the mould with the negative pattern. When PDMS is hardened through the curing process, it is peeled off and the microstructure is formed in the PDMS chip (Fig. 3.2e-f).

Soft lithography represents a mainstream method for fabricating microfluidic devices due to the intrinsic advantages of PDMS, which is non-toxic to cells and permeable to biologically important gas. Moreover, PDMS is optically transparent and essentially soft and flexible compared with solid materials such as glass. The transparency of PDMS allows the applications of optical sensing methods, particularly the fluorescent sensing, without causing significant interference. With a remarkable advantage in replicating, the procedures of soft lithography can be accomplished in an ambient laboratory environment and no major expense will be produced once the master is patterned [219]. Furthermore, the tunability of the surface properties of PDMS enables the adjustments of hydrophilicity and therefore the bonding capability of the PDMS chip to various materials.

Considering the outstanding strengths of PDMS as discussed above, the microfluidic chip used in this work was fabricated with PDMS by soft lithography.

3.2 Methods

3.2.1 Design of the microfluidic chip

The proposed design of the chip layout is shown in Fig. 3.3a. The microfluidic chip consisted of three inlets, where cell culture mediums would be loaded via the first two inlets and fluorescent indicator would be introduced through inlet 3. Following the inlets, two sections of

serpentine channels were implemented to increase the mixing efficiency of molecules in the solutions. To achieve the immobilisation of biological tissues (e.g. the pancreatic islets), a tissue array was incorporated within the first serpentine channel. Under the continuous perfusion, the effluent of the tissues would be collected from the tissue array and flowed into the downstream channel. The extracellular fluid was then mixed with the indicator solution in the second serpentine channel. Following the second serpentine channel, an optical window was built for fluorescence detection. The detailed criteria of the chip design were described as follow:

1) Double-input inlets. Double-input system was designed for introducing stimulation in cell culture medium and fluorescent indicator via stimulation inlet and indicator inlet, respectively. The stimulation inlet consisted of two converged inlets, inlet 1 and inlet 2. The stimulation inlet was built in prior to tissue trapping to supply the tissue with refreshing medium and stimulation. The indicator inlet, inlet 3, was built beyond the tissue trapping site so that the fluorescent indicator(s) could be mixed with the effluent from the tissue for quantifying $[Ca^{2+}]_{ex}$. Meanwhile, building the indicator inlet after the tissue array would eliminate the interaction between the indicator and tissues, including the intake of indicator into the cells and the potential toxicity of the indicator imposed on tissues.

2) Tissue trapping structure. As this chip was designed for investigating the insulin secretion from the pancreatic islet, structures for immobilizing islet tissues were required to be built in the chip. This work adopted the design of a tissue array for islet immobilisation. The tissue array consists of a column of U-shape cups, which showed the advantages in reducing the shear stress on the tissue and amplifying the secretion by adjusting the number of the cups [159,174].

3) Mixing efficiency. In the stimulation inlet, two groups of cell culture medium containing different concentrations of stimulus, typically one of the inlets with glucose, could be pumped into the chip to controllably create the dynamic stimulation. To ensure the immobilised tissues to be exposed to identical stimulation, the complete mixing of mediums from inlet 1 and 2 was required before the mixture arrives at the tissue array. Therefore, serpentine channels were built into the chip design. The first one was built after the stimulation inlet to improve the mixing efficiency of

stimulatory molecules. The second serpentine channel was built post tissue array to enhance the mixing of the indicator solution with the effluent from the tissue array.

4) Dimensions of channels and U-shape cups. The pancreatic islets would be loaded into the chip by injection via inlet 1 or 2. Once in the channel, the tissues flowed through the channel under the continuous injection until they were captured in the tissue array. As the size of islets varies from 40 to 200μm in diameter and the shapes are close to the sphere, the width and height of the microfluidic channel were proposed to be 300μm and 250μm, respectively (Fig. 3.3b & c). For the tissue cups, the dimension was designed as reported in the literature [162,177], where the opening was 250μm and the narrow cross-section area was 45μm (Fig. 3.3e). With the proposed dimensions, the channels would allow the free movement of tissues without causing clogging and the cups would be able to effectively capture the tissue.

5) The dimension of the optical window. An optical window with 500μm in diameter was incorporated after the second serpentine channel (Fig. 3.3d) for two reasons: (i) The diameter of the optical window was larger than the channel width so that it would be capable of containing a larger volume of the sample for detection of a higher fluorescent signal at the optical window; (ii) The optical window was not overly large to cause time delay in refreshing the sample inside. Detailed dimensions of mask design were shown in Fig. 3.3b-e as drawn in AutoCAD.

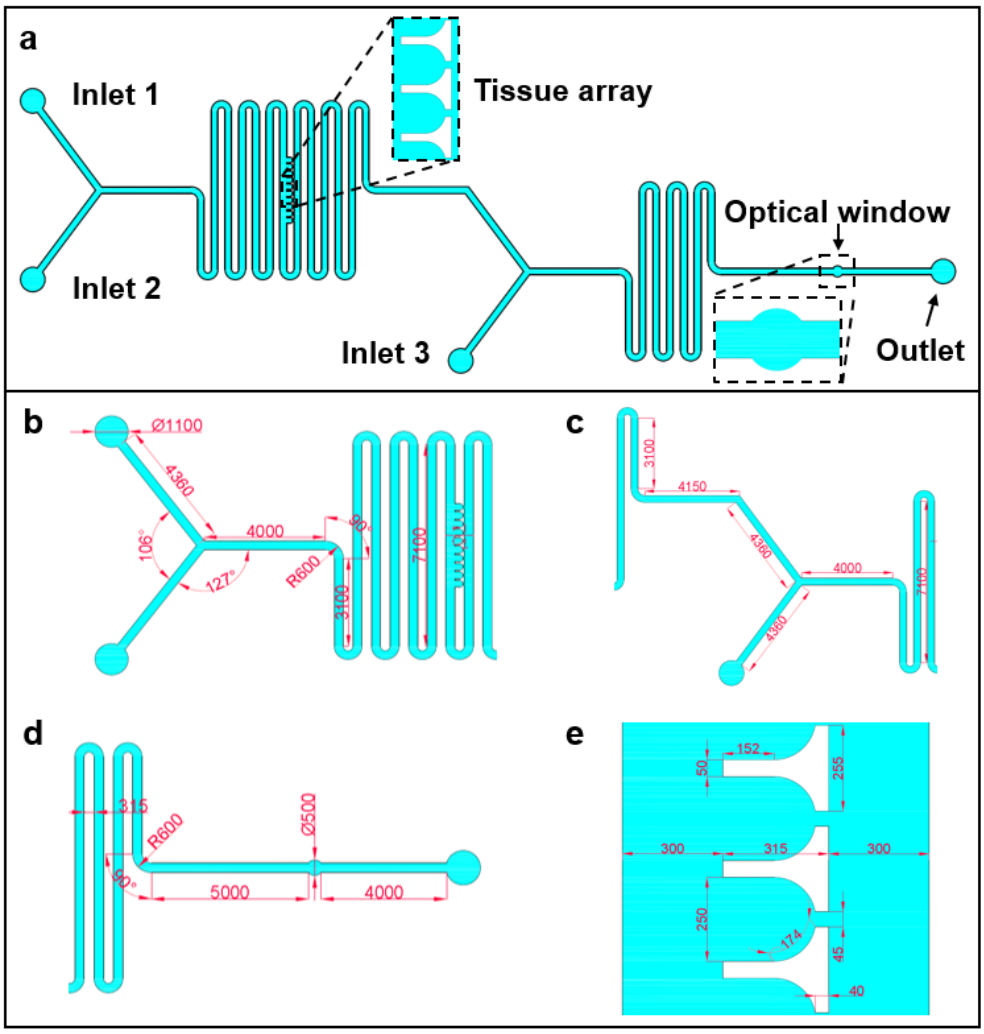

Figure 3.3 | The layout and dimension of the microfluidic chip design. a | The overall layout of the microfluidic chip, which consisted of three inlets, two serpentine channels, a tissue array embedded in the first serpentine channel, an optical window and an outlet; **b-e |** The detailed dimensions of the chip structure.

3.2.2 Theoretical simulation of the fluid dynamics

To understand the flow regime in the proposed design, the Reynolds number was calculated as a function of the flow rate based on the proposed chip dimension and the equations in section 3.1.1.1. By plotting the Reynolds number against the flow rate, the ranges of flow rates were identified as laminar flow, transitional flow or turbulent flow in the microfluidic channel. Then the theoretical lengths required for the thorough mixing of glucose, Ca^{2+} and insulin were calculated to understand the relationship between flow rate and mixing length for each of the molecule in a straight channel. The serpentine channel is not necessary if the required length is much shorter than the scale of a microfluidic chip under a common flow rate for biological

study (1-10μL/min). Otherwise, the serpentine channels are indispensable to facilitate the mixing.

The fluid dynamics in the microfluidic channels were further simulated in COMSOL 5.3 (COMSOL Multiphysics, Sweden) to understand the fluid dynamics. The geometry for the simulation study was imported from the mask design in AutoCAD. The computational fluid dynamic (CFD) simulation was performed using the 'laminar flow' model. Under the physical model section, an incompressible flow model was applied to the simulation under general environment pressure level of 1atm and the temperature of 293.15K, i.e. the general room condition. The material used in the study was defined as water, with a density of 1000kg/m^3 and a dynamic viscosity of 0.001Pa•s. The boundary conditions of inlet 1 and 2 were defined with a fluid velocity of 10μm/s, while the velocity at inlet 3 was set as 20μm/s in order to compare the accumulated velocity of inlet 1 and inlet 2 with inlet 3. The velocities were arbitrarily set for a preliminary understanding of the fluid dynamics. At the outlet, the pressure was set as 1atm (same pressure as the outlet is exposed to air) with suppressed backflow. The physics-controlled mesh was used for the mesh sequence type with a normal element size under the default setting.

Taking into account the criterion factors and simulation output, the chip design was sent to Dr. Aliaa Shallan for fabrication via soft lithography under the supervision of A/Prof. Craig Priest at the Future Industries Institute, University of South Australia. Similar fabrication procedure can be found in their previous papers [220,221].

3.2.3 Optical examination of the dimension of microfluidic channels

To examine the dimensions of the fabricated microfluidic chip, an optical microscope (Olympus BX51, Olympus, Japan) was used to examine the overall outlook of the microfluidic channels and an optical profiler Contour GT-I (Bruker, Germany) was then used to measure the detailed dimension of the chip. The measurement type was VSI, which was suitable for measuring the sample thickness higher than 135nm with precision at nano-meter. In order to expand the view, 5× and 0.55 were applied on the objective and multiplier respectively. Three PDMS chip replicas were measured and the averaged values of the measurements were used for further analysis.

3.2.4 Experimental characterisation of the fluid dynamics

A microfluidic perfusion system was set up to investigate the fluid dynamics in the microfluidic chip as shown in Fig. 3.4. The perfusion system consisted of a microfluidic pump with three syringe drivers (NanoJet Stereotaxic Syringe Pump, Chemyx, USA), three 500µl glass syringes (SGE, Trajan, USA), Fluorinated ethylene propylene (FEP) tubing (1/16'' OD× .010'', IDEX, USA), inverted optical microscope (Olympus IX73, Olympus, Japan) and a waste container. Syringes and tubes were connected by 10-32 female and male lure adapter (IDEX, USA). Syringes, tubes and PDMS chip were loaded with ethanol before each experiment to reduce the entrapment of bubbles and then rinsed with DI water for three times.

To indicate the flow dynamics in the channel, a 10% food colouring solution was prepared by 100µL diluting the red food colouring in 900µL DI water. To investigate the mixing efficiency of the channel, 0.5mg/mL Rhodamine-B (Sigma, USA) was prepared by dissolving 5mg Rhodamine-B in 10mL DI water.

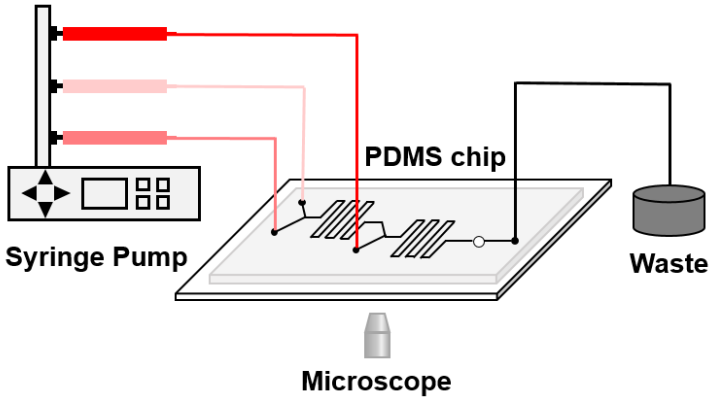

Figure 3.4 | Schematic of the experimental set up of the microfluidic perfusion system. Three syringes were connected to the PDMS chip via FEP tubes. The flow rates of the three syringes were controlled by a syringe pump. For fluid observation, the chip was placed on an inverted microscope. The outlet was connected to a waste container.

3.2.5 Investigation of the particle trapping efficiency

Blue polyethylene (PE) microspheres (Cospheric, USA) were used as tissue surrogates to investigate the efficiency of the tissue trapping structure. The microspheres with diameters in 90-100µm were selected as they were similar to the pancreatic islets in size and density. The microspheres suspension was prepared as indicated by the protocol. Briefly, 250mg

microspheres were dispersed in 1mL 0.1% Tween 80 (Sigma, USA) and the suspension was further diluted 100 times into 2.5mg/mL with 0.1% Tween 80 as the final injection sample. Prior to the loading, the microfluidic chip was rinsed with DI water and placed on the inverted microscope. The microspheres were loaded into the microfluidic chip by injecting with a 200μL pipette via inlet 1, while inlet 2 and inlet 3 were blocked by connecting to the paused pump and the outlet was exposed to air. The microspheres were carried into the channel and further into the tissue array with the injection flow.

3.3 Results and discussion

3.3.1 Reynolds number

With the proposed chip width (300μm) and height (250μm), the hydraulic diameter was determined based on Eq. 3.2 and 3.5:

$$D_h = \frac{4A}{U}$$

$$D_h = \frac{4 \times w \times h}{2 \times (w + h)}$$

$$D_h = \frac{4 \times (0.3 \times 10^{-3}) \times (0.25 \times 10^{-3})[m^2]}{2 \times (0.3 \times 10^{-3} + 0.25 \times 10^{-3})[m]}$$

$$D_h = 2.72 \times 10^{-4}[m]$$

In order to build up the relationship between flow rate and Reynold number, the volumetric flow rate Q[μl/min], which is commonly used in the microfluidic experiment, was transformed into the fluidic velocity v[m/s] in the proposed channel:

$$v = \frac{Q[\mu l/min]}{wh[m^2]}$$

$$v = \frac{Q \times 10^{-9} \div 60[m^3/s]}{0.25 \times 10^{-3} \times 0.3 \times 10^{-3}[m^2]}$$

$$v = Q \times 2.22 \times 10^{-4}[m/s]$$

The Reynolds number in the proposed channel was further determined based on Eq. 3.1 and physical properties of water. The viscosity of water depends on the temperature: the viscosity is 1.004×10^{-3} [kg/m•s] at 20°C and 0.691×10^{-3} [kg/m•s] at 37°C.

At 20℃,

$$Re(T = 20℃) = \frac{\rho v D_h}{\mu}$$

$$Re(T = 20℃) = \frac{1000 \times 2.72 \times 10^{-4} \times Q \times 2.22 \times 10^{-4}[kg/m \bullet s]}{1.004 \times 10^{-3}[kg/m \bullet s]}$$

$$Re(T = 20℃) = 6.01 \times 10^{-2} \times Q$$

At 37℃,

$$Re(T = 37℃) = \frac{1000 \times 2.72 \times 10^{-4} \times Q \times 2.2 \times 10^{-4}[kg/m \bullet s]}{0.691 \times 10^{-3}[kg/m \bullet s]}$$

$$Re(T = 37℃) = 8.74 \times 10^{-2} \times Q$$

As shown in Fig. 3.5, Reynolds number in the proposed channel was plotted against the flow rate at different temperature. At 20°C, the flow in the microfluidic channel transformed from laminar flow to turbulent flow at a flow rate of 34.94mL/min, while the transiting flow rate for 37°C was 24.03mL/min. As the usual flow rate in a microfluidic device is at the scale of microliter per minute, the fluid in the proposed microfluidic chip would typically be laminar both at room temperature and physiological temperature.

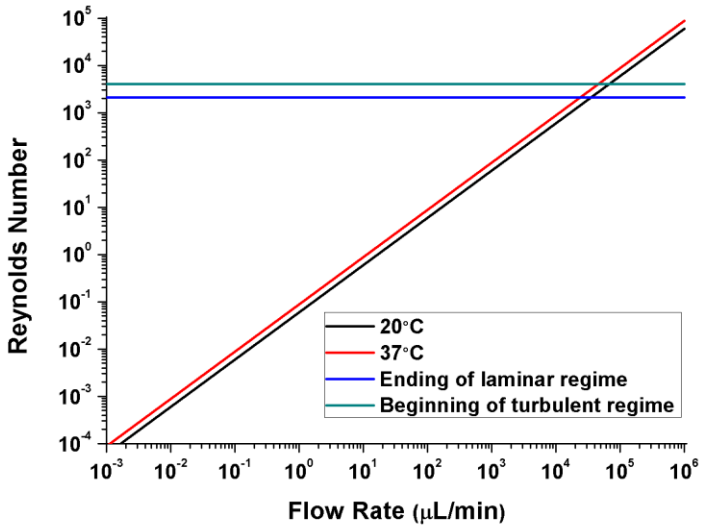

Figure 3.5 | The Reynolds number of fluid in the proposed design as a function of flow rate. Black and red lines indicate the Reynold numbers at 20°C and 37°C respectively. The area under the blue is defined as laminar flow, while the area between the blue line and green line indicates the transitional flow. Flows are turbulent if the Reynolds number is in the area above the green line.

3.3.2 Molecules diffusion

As the flow was typically laminar in the proposed design, the mixing of the two co-flow solutions relied on the diffusion of the molecules as above mentioned. It is important to know the channel length to reach a homogeneous distribution of the molecules across the channels. In this case, glucose was the molecule of interest as it would be used as the stimulus for future biological experiments. Therefore, the calculated channel length for glucose molecule was expected to be shorter than the practical distance from inlets to tissue array in the design, so that all the tissue in the arrays would be exposed to the same concentrations of glucose.

Based on Eq. 3.9 and D [cm^2/s] of the molecules (Table3.2), the relationship between the required mixing length for each molecule and the flow rate Q[μL/min] was expressed as:

$$L \approx \frac{Qw}{hD}$$

$$L \approx \frac{Q \times 10^{-9} \div 60\ [m^3/s]\ \times 0.3 \times 10^{-3}[m]}{0.25 \times 10^{-3}[m] \times D \times 10^{-4}[m^2/s]}$$

$$L \approx \frac{Q \times 10^{-6}}{5 \times D}[m] \quad (Eq. 3.13)$$

Table 3.2 | Diffusion coefficients for key molecules in this study

Molecule	Molecular weight (Da)	Diffusion coefficient (cm^2/s)	Ref.
Glucose	180.16	6.7×10^{-6}	[222]
Ca^{2+}	40.08	7.9×10^{-6}	[223]
Insulin (bovine)	5733.49	7.3×10^{-7}	[224]
Rhodamine-B	479.02	4.2×10^{-6}	[225]

As shown in Fig. 3.6, the required mixing length for the three relevant molecules were plotted against the flow rates in the perfusion channel. To visualise the mixing length for the three molecules, the length of half a common glass microscopic slide (3.5cm) is shown as the green line. In a microfluidic channel without any mixing structure, 5.9cm length of the channel was required for a complete mixing of glucose at a flow rate of 2μL/min (pink line), which was almost the minimal flow rate for secretion study. Accordingly, the channel of the microfluidic chip would be over the scale of a glass slide if the mixing mechanism only relied on the diffusion of the molecules. Thus, the results justified the need for incorporating the serpentine channels into the microfluidic channel to improve the mixing. The incorporation of serpentine channels would not only extend the distance that the molecules travel through, but also would enhance the mixing of two co-flowing solutions via centrifugal forces when they pass the curved section [226]. The actual mixing efficiency will be discussed in section 3.3.5.

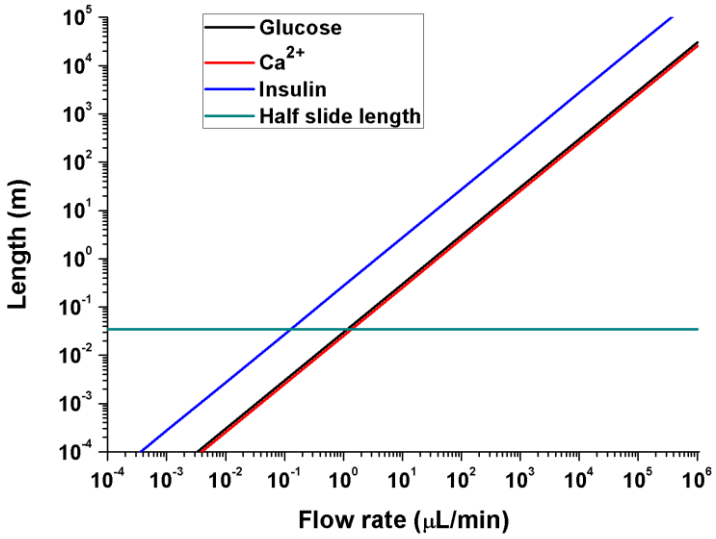

Figure 3.6 | The required mixing length for three relevant molecules as a function of flow rate. The mixing lengths of insulin, glucose and Ca^{2+} are shown in blue, black and red lines, respectively. The red line shows the basal length for the mixing of glucose in the secretion study, while the green line indicates the length of half a microscopic slide.

3.3.3 Computational fluidic dynamics (CFD) simulation

Fig. 3.7 shows the initial velocity settings and the velocity profile in the simulation. The boundary conditions of inlet 1, inlet 2 and inlet 3 were set as initial flow velocities of 10μm/s, 10μm/s and 20μm/s (arbitrary value), respectively (Fig. 3.7a). The overall simulation displayed a typical velocity profile of a laminar flow, where the fluid velocity was highest in the channel centre and dropped down to zero at the wall. The velocity mapping indicates that the distribution of the velocity is consistent with the conservation of mass (Fig. 3.7b).

$$v_1 + v_2 = v_4 = v_5 = v_3$$

$$v_6 = v_3 + v_5 = v_3 + v_1 + v_2$$

Notably, at the bottom half of the serpentine channel (indicated by the red arrow in Fig3.7b) where the tissue array was embedded in, the velocity was significantly smaller than the neighbouring main channel, suggesting that a significant amount of fluid was flowing through the tissue cup. The zoom-in view of the U-shape cups indicates the occurrence of a substantial partial stream (Q_2) and a mainstream flow (Q_1) when the flow passes through the tissue array. When the tissues are flowing in the channel, the individual tissue could be guided to occupy

the cups under the sequential effects of Q_2 and Q_1. As the perfusion system would be running continuously, the partial flow stream and the higher flow velocity at the narrower cross-channel section (indicated by the red arrow in zoom-in inset figure) would stabilise the tissue in the trapping site under hydrodynamic force [162] (Fig. 3.7c).

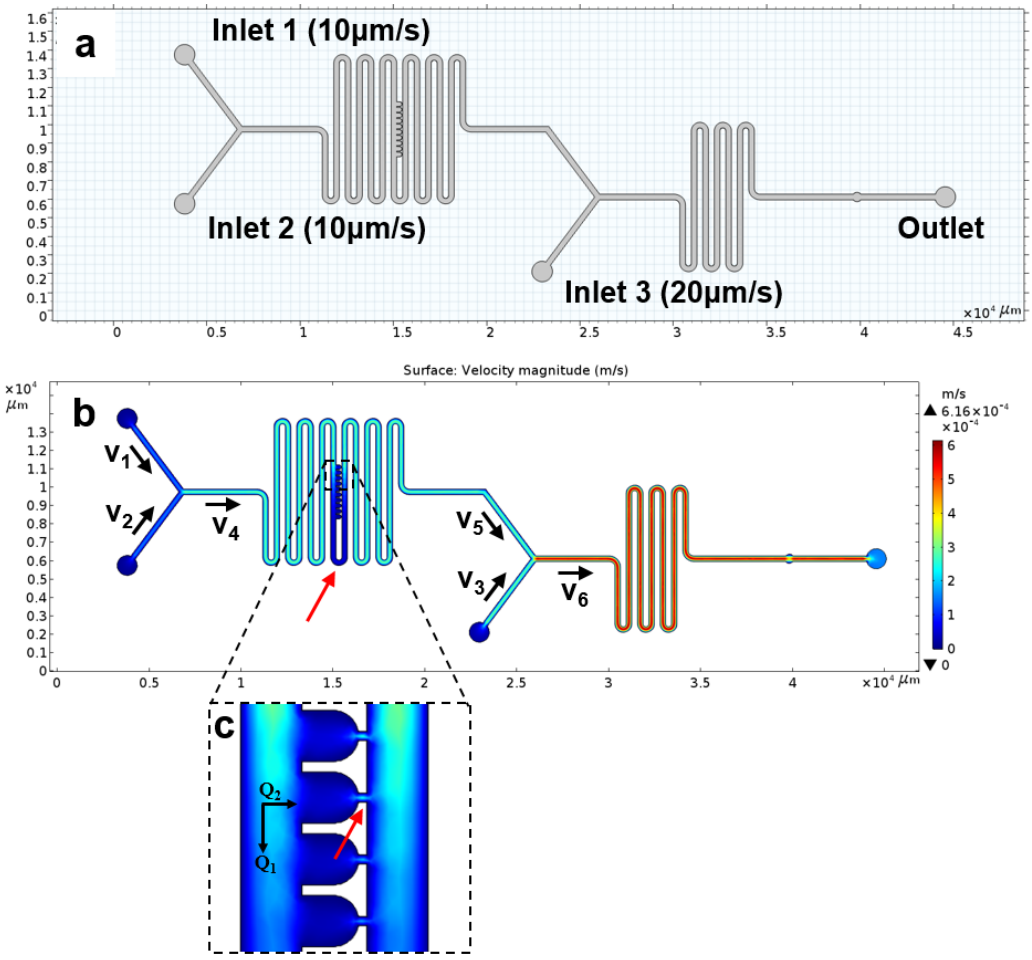

Figure 3.7 | Computational fluidic dynamics (CFD) simulation on COMSOL. a | The simulation geometry and initial flow velocity at inlet 1 (10µm/s), inlet 2 (10µm/s) and inlet 3 (20µm/s). The velocity was set by arbitrary units; **b |** The velocity mapping of the microfluidic channel; **c |** A close-up view at the tissue cups, where the flow is separated into a main stream (Q_1) and a partial stream (Q_2). The red arrow highlights the higher velocity at the cross-section area.

3.3.4 Dimension of the microfluidic geometry

The overall outlook of the microfluidic channels is shown in Fig. 3.8i. The PDMS chips fabricated through soft lithography displayed well-defined microfluidic channels (Fig. 3.8a-f) which were highly consistent with the mask design on AutoCAD (Fig. 3.3a).

A major challenge in fabricating this microfluidic device was to preserve the narrow cross channel section, which was 40µm in width and much smaller than the main channel (300µm in width). Therefore, a proper developing time for dissolving the PDMS was critical as under-development of PDMS would lead to residue sticking to the wall and over-development of PDMS would cause damage to the channel structure. As shown in Fig. 3.8c, the tissue array displayed no residues in the arc of the cup or damage caused by over-development. Moreover, the multiple trapping cups were accurately aligned, suggesting the fabrication protocol produced a minimal distortion to the micro-pattern. Similarly, the 3D simulated images of the microfluidic channel show that the microstructures were highly preserved in the fabricated chip (Fig. 3.8g & h).

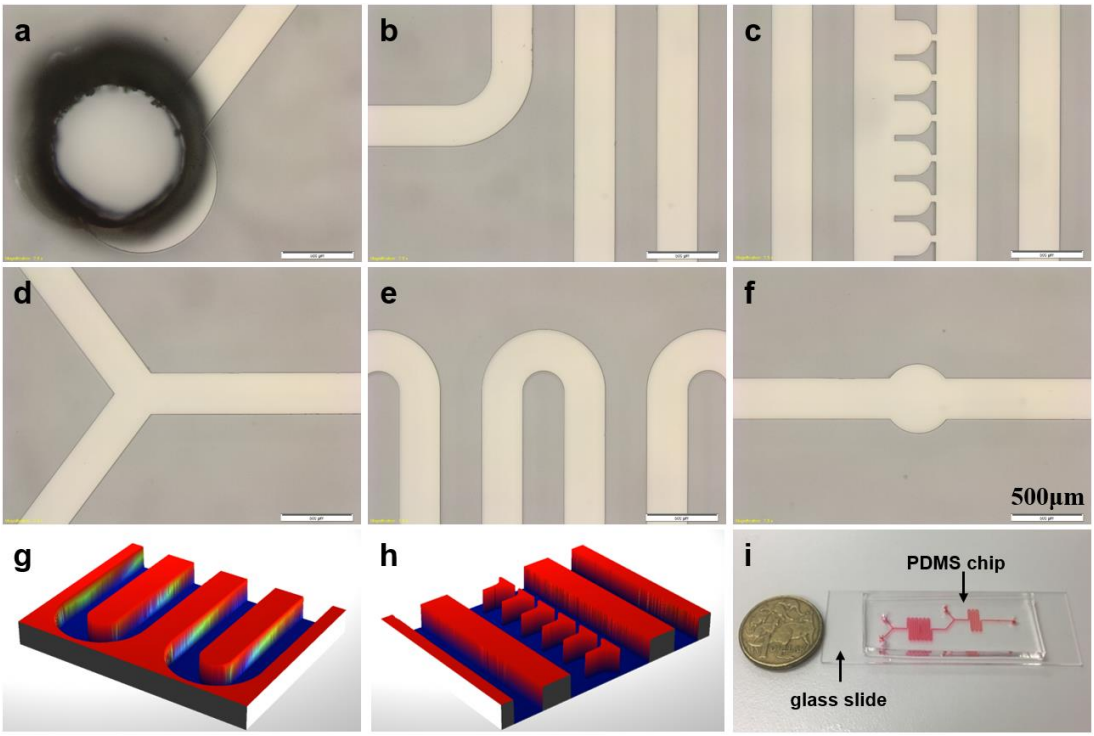

Figure 3.8 | The appearance of the microfluidic chip examined by optical microscope and optical profiler. a-f | The overall outlook of the channel examined by an optical microscope is clean and highly consistent with the mask design, suggesting the soft lithography well preserved the micro-pattern when translating the design into a PDMS chip; **g-h |** 3D simulated images based on the measurement of optical profiler indicate that soft lithography produced smooth channel surfaces throughout the PDMS chip. The 3D structure of the design was highly preserved in the fabricated devices; **i |** Outlook and size of the microfluidic chip in comparison with a coin (one Australian dollar). The chip consisted of a PDMS chip with embedded micro-patterns and the PDMS chip bound to a glass slide via surface plasma treatment.

To precisely examine the dimension of the PDMS chip, the size of microfluidic structures measured by the optical profiler was compared with the original mask design. As shown in Table 3.3, the dimensions of the PDMS chip displayed a trend to undergo shrinkage in general. There were two reasons that can contribute the shrinkage. Firstly, the PDMS was poured into the mould to form the structure, thus it was normal that the dimension of the final PDMS chip was smaller than the mould. Secondly, the curing process in the mould was performed by incubation at 70°C so the PDMS was likely to undergo physical shrinkage when it cooled down to room temperature (thermal expansion coefficient of PDMS: 300×10^{-6} °C^{-1}) [227].

Comparing the errors in relatively larger structure with the smaller ones, the PDMS chips showed smaller errors (<10%) in the larger geometries, as reflected by the width and height of the main channel, the opening and base of the tissue array. However, the chips exhibited much higher errors (~25%) in the smaller structure, including the walls and cross-channel sections and of the tissue cups (Table 3.3). The larger errors in the smaller structure reflected the difficulties in fabricating the structures with tens of micrometres within the major channels at dimensions of hundreds of micrometres.

Table 3.3 | Comparison of the dimensions of the design and fabricated device

Structure	Main channel		Tissue array				
	Width	Height	Opening	Wall	Cross-channel	Base	Body
Design	300	250	250	50	45	255	315
PDMS chip	289 ± 2	236 ± 7.9	235.8 ± 3.6	37.5 ± 2	55.6 ± 2.09	226.2 ± 2.1	285.4 ± 2.1
Error (%)	3.7	5.6	5.68	25	23.56	9.3	9.40

3.3.5 Fluid dynamics in the microfluidic channels

To experimentally characterise the fluidic behaviours in the microfluidic channel, manipulation of input solution and mixing efficiency of molecules in the channel were investigated. The former indicates the capability of producing a dynamic culture environment for the tissues, while the latter defines the flow rate range, within which all the tissues in the trapping site would be exposed to homogeneous stimulations. Without the addition of serum or other sources of protein, the density and viscosity of PBS and cell culture medium are not significantly different from the properties of water. Based on Eq. 3.1, the Reynold number of PBS or cell culture medium should be essentially similar to water. Therefore, DI water was used in the

experimental characterisation and the results are sufficient to reveal the fluidic dynamic of PBS or cell culture medium.

3.3.5.1 Input manipulation

The manipulation of input was achieved by modifying the ratio of flow rates at the inlet 1 and inlet 2. In this experiment, food colouring and DI water were pumped into the channel via inlet 1 and inlet 2, respectively. When adjusting the ratio between the two flow rates (from 9:1 to 1:9), different concentrations of the food colouring were produced in the microfluidic device. As shown in Fig. 3.9, the width of the food colouring flow decreased as the ratio between the flow rates of food colouring to water decreased. The differences in the width of food colouring flow resulted in serial diluted concentrations of food colouring from 0.9 to 0.1 of the original concentration of the colouring pumped via inlet 1. The results indicated that, in the future, a wide range of stimulus concentrations can be achieved by switching the flow rates ratio between the two inlets, where two solutions containing different concentrations of stimuli are pumped into the channel.

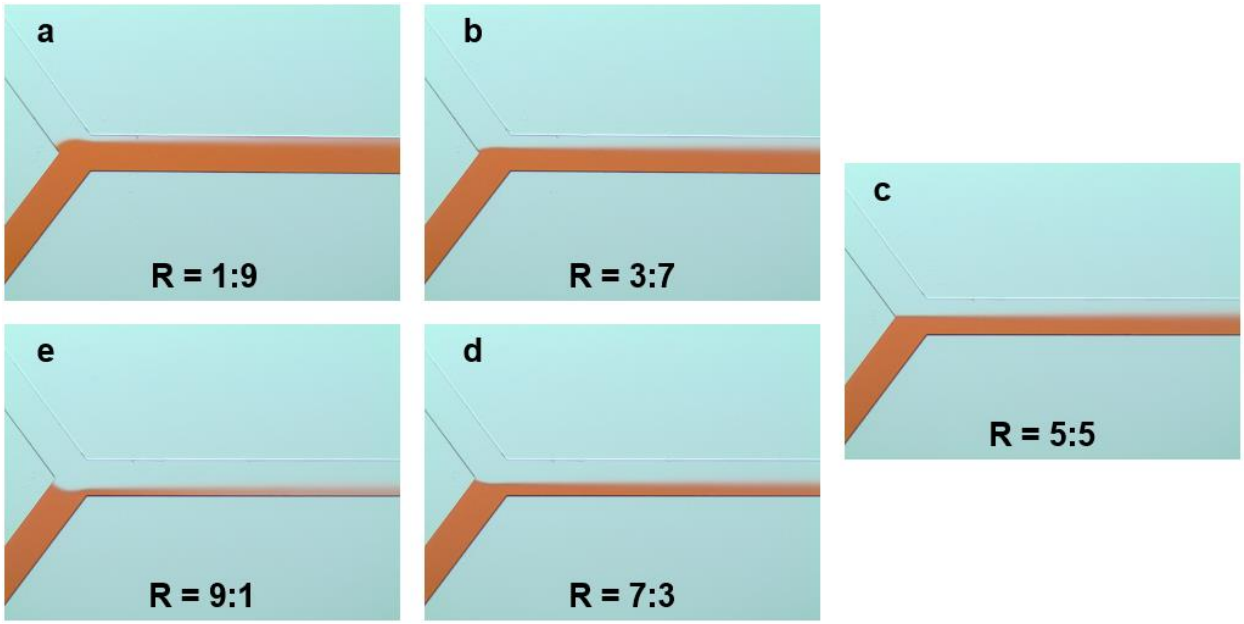

Figure 3.9 | Experimental of analysis of input manipulation to achieve different final concentrations of food colouring. Food colouring and DI water were pumped into the microfluidic channel via inlet 1 and inlet 2, respectively. (R indicates the ratio between the flow rate of food colouring and DI water.)

3.3.5.2 Mixing efficiency

The mixing efficiency of the microfluidic chip was examined by the distribution of the colouring molecules upon the arrival at the tissue trapping site. Either food colouring or Rhodamine-B was pumped into the microfluidic channel with DI water via inlet 1 and inlet 2, respectively, at a flow rate ratio of 1:1 (Fig. 3.10a & d). Based on Eq. 3.9 and 3.10, a higher flow rate or a larger molecular radius would lead to a longer length to achieve a homogenous distribution of the molecules.

Fig. 3.10b shows that the flow rate of food colouring at 8µl/min (or lower) produced a homogeneous distribution of molecules before the flow reached the tissue array. When the flow rate increased over 8µl/min, uneven concentrations of food colouring were observed across the channel at the trapping site. The heterogeneous distribution was particularly apparent when the flow rate reached 14µl/min (Fig. 3.10c), suggesting the mixing of dye molecules was incomplete and the concentration of the colouring was varying in each cup.

As the diffusion coefficient of food colouring was not clear, Rhodamine-B (known diffusion coefficient, Table 3.2) was introduced into the channel via stimulation inlet so that the maximum flow rate for glucose could be calculated based on the mixing efficiency of Rhodamine-B.

For Rhodamine-B, as the molecular radius was larger than the radius of food colouring molecule, heterogeneous distribution (insufficient mixing) of the Rhodamine-B in the microfluidic channel was observed with flow rate even low to 6µl/min (Fig. 3.10g-i). Specifically, the concentration of Rhodamine-B was higher at the side with the opening of the cup and lower at the wall side (Fig. 3.10h). As a result, flows in the first two cups (indicated by the dashed rectangle) were exposed to much higher concentrations of the dye compared with the following cups. Alternatively, if the inlet for Rhodamine-B swapped with the inlet with water, the concentration of Rhodamine-B was lower at the opening side, leading to much lower concentrations of Rhodamine-B in the first few cups (Fig. 3.10i). In contrast, complete mixing of Rhodamine-B upon reaching the trapping site was achieved with the flow rate at 3µl/min as indicated by the arrows (Fig. 3.10d & e).

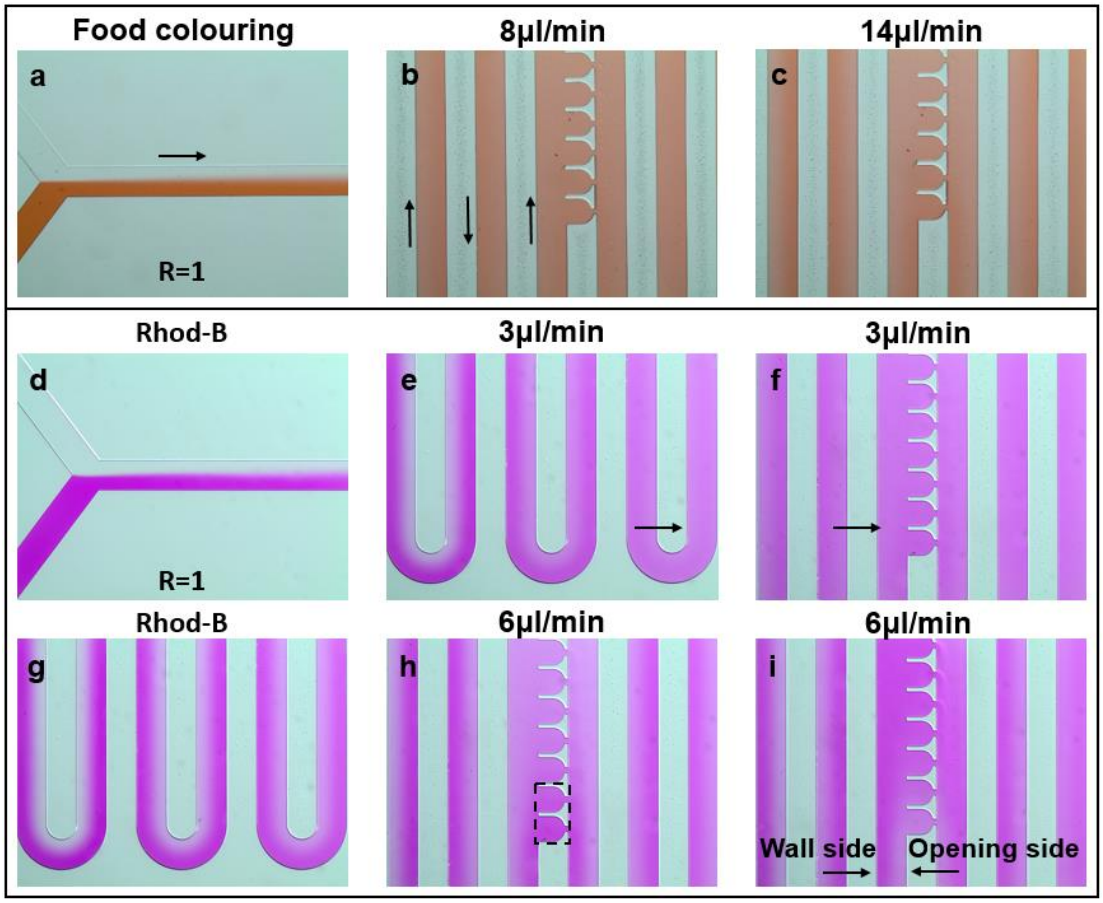

Figure 3.10 | The mixing efficiency of food colouring and Rhodamine-B at different flow rates in the microfluidic chip. Flow rates shown above each panel indicates the corresponding total flow rate of inlet 1 and inlet 2. **a |** Food colouring and DI water were pumped into the microfluidic chip via inlet 1 and inlet 2. The ratio of the flow rates at the two inlets was 1:1; **b |** Homogenous distribution of food colouring was achieved prior to the tissue array when the total flow rate of inlet 1 and inlet 2 was lower than 8µL/min; **c |** An incomplete mixing of food colouring was observed when the flow rate reached 14µL/min; **d |** Rhodamine-B and DI water were pumped into the microfluidic chip via inlet 1 and inlet 2 at the flow ratio of 1:1; **e – f |** Homogenous distribution of Rhodamine-B was achieved prior to the tissue array when the flow rate was 3µL/min or lower; **g – i |** Heterogeneous distribution of Rhodamine-B were observed as the flow rate reached up to 6µL/min. The dashed rectangle shows the dye concentrations significantly different from the following cup if the mixing is incomplete.

At a given channel length L from inlet to the tissue array, the maximum flow rate for ensuring a sufficient mixing of a molecule is expressed based on Eq. 3.10:

$$Q \approx \frac{LhD}{w}$$

Therefore, the relationship between the maximum flow rate for glucose Q_G and Rhodamine-B Q_R can be written as:

$$\frac{Q_G}{Q_R} \approx \frac{LhD_G}{w} \times \frac{w}{LhD_R}$$

$$\frac{Q_G}{Q_R} = \frac{D_G}{D_R} \quad (Eq. 3.14)$$

The diffusion coefficient of glucose and Rhodamine-B are $6.7\times10^{-6}cm^2/s$ and $4.2\times10^{-6}cm^2/s$, respectively. The maximum flow rate for glucose was calculated as:

$$Q_G \approx \frac{6.7 \times 10^{-6}}{4.2 \times 10^{-6}} \times Q_R = 4.77[\mu L/min]$$

With the fixed length from inlet to tissue array, the maximum flow rate from the stimulation inlet was estimated to be around 4.77μL/min to allow a homogeneous distribution of glucose across the channel upon reaching the tissue array. It is worth noting that the perfusion experiment in this section was conducted at room temperature 23°C (296.15K). In the future biological experiment, the perfusion system would be heated up to 37°C (310.15K). Therefore, the diffusion coefficient would increase according to Eq. 3.7:

$$D = \frac{kT}{6\pi r\mu} \quad (Eq. 3.7)$$

Based on Eq. 3.14 and Eq. 3.7, the maximum flow rate for glucose at 37°C (Q_B) can be expressed as

$$\frac{Q_B}{Q_G} \approx \frac{D_B}{D_G} = \frac{310.15K}{296.15K}$$

$$Q_B = 1.047 \times 4.77[\mu L/min]$$

$$Q_B = 5[\mu L/min]$$

Therefore, complete mixing of glucose can be ensured at the tissue array when the total flow rate of inlet 1 and inlet 2 is 5μL/min at 37°C. As glucose is the most prevalent stimulus in islet study, 5μL/min would be used as the flow rate in Chapter 4 to characterise the sensing

performance of the system so that the characterisation will have biological implications for the applications in pancreatic islets.

3.3.6 Particle trapping efficiency of the tissue array

To simulate the loading procedure of pancreatic islet, the particle trapping experiment was performed to investigate the trapping efficiency of the tissue array. Notably, the actual size of the beads varies from 45-90μm in diameter, which was smaller and more heterogeneous than the size in the product information (90-100μm). As the beads loading was achieved by manual injection with a 200μL pipette, the flow rate, instead of giving an accurate value, would be described as slow if the 200μL was injected within a few minutes or fast if the injection was completed in tens of seconds.

As shown in Fig. 3.11b, the beads were successfully captured by the tissue array after their loading via injection at inlet 1 with a slow flow rate. By optimizing the concentration of the microspheres at 2.5mg/mL, nearly every cup was occupied by a single bead. When extending the loading time (slow flow rate), the beads were continuously captured by the tissue array (Fig. 3.11d-f). It was interesting to note that the beads delivered by this flow rate were all stacked in the cups without leakage before the cup was full. In contrast, beads immobilised in the cup were shown to be pushed out of the cup under fast injection (Fig. 3.11c), suggesting the fast injection resulted in higher hydraulic pressures in the cups. These observations suggested that apart from the loading time, the injection speed or flow rate (corresponding to the localised pressure in the cups) affected the loading efficiency. More importantly, all experimental results indicate that, in the U-shape cups, the partial flow Q_2 lead to the effective guidance of beads into the cups, which is in good agreement with the simulation work (Fig. 3.7).

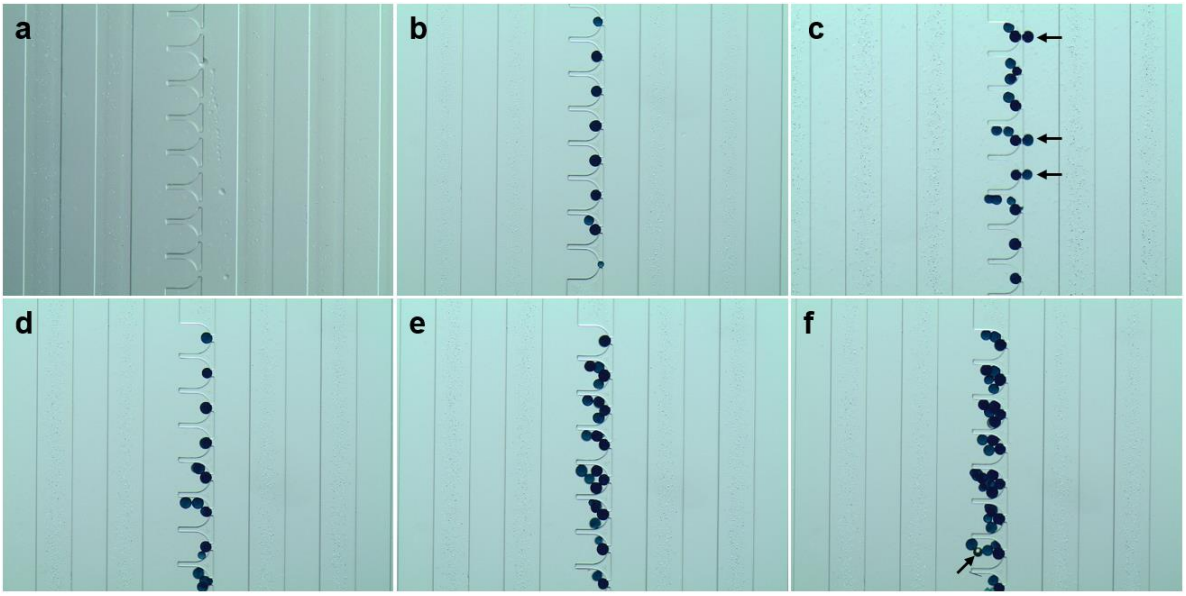

Figure 3.11 | The trapping efficiency of the tissue array with micro-beads (45-90µm in diameter). a | Microfluidic channel perfused with water; **b |** Micro-beads were loaded into the tissue array and trapped in the cups via manual injection through a 200µL pipette; **c |** The beads were pushed out the cups during fast injection; **d-f |** The number of beads in each cup increased in the continuous loading. The black arrow points out a bubble that was trapped during the experiment.

3.4 Discussion

In this chapter, the microfluidic chip aimed for detecting $[Ca^{2+}]$ and secretion analysis was designed, fabricated and characterised. The microfluidic chip consisted of stimulation inlets, serpentine channels, tissue array, indicator inlet and outlet. Driven by the ultimate goal of investigating the role(s) of $[Ca^{2+}]_{ex}$ in the secretion of insulin, the microfluidic chip was designed to be capable of controlling culturing environment of tissues, continuously extracting the extracellular fluid, introducing fluorescent Ca^{2+} indicator, detecting $[Ca^{2+}]_{ex}$ and collecting samples for insulin quantification.

Prior to the chip fabrication, the rationales of the design were examined by the fluidic dynamics simulation (based on the related fluidic physics). The Reynolds number calculation confirmed the laminar flow in the proposed device. The diffusion calculation for glucose suggested that the molecule diffusion was insufficient for a complete mixing upon reaching the tissue array, which justified the necessity to integrate the serpentine channels for enhancing the mixing efficiency. The CFD simulation indicated that substantial partial flow was flushing through the

U-shape cups, enabling the capture of tissues and continuously refreshing the extracellular environment.

The proposed microfluidic chip was then manufactured by soft lithography with PDMS. The overall outlooks of the fabricated PDMS chips displayed a well-structured microfluidic channel, which was highly consistent with the mask design. Certain fabrication errors (the physical dimension of the chips smaller than the design) were found in the as-fabricated PDMS chips, which were majorly due to the shrinkage property of PDMS during curing. However, as the dimensions of fluidic channels (hundreds of microns) and cross-section area of U-shape cup (down to tens of microns) were significantly different, varying deviations (<10% for large structure and around 20% for smaller structure) were observed in different structures of the chip.

Pilot experiments of simulating the loading of pancreatic islets by micro-beads demonstrated the capability of the tissue array to efficiently capture the micro-scale objects in the microfluidic channels. With the diluted beads suspension and relatively short injection time, the optimal loading was achieved as a single bead was captured in each cup. However, if the suspension was over-injected into the channel, it was challenging to achieve the optimal trapping as the beads tended to stack in the cups until they filled the cup. Moreover, the beads were shown to be pushed out of the cup under fast injection due to the higher pressure imposed on the beads in a faster flow. Nevertheless, the loading of pancreatic islets is expected to be promising based on the loading experience on microspheres. Firstly, the sizes of mammal pancreatic islets for loading can be selected between 150 and 200μm [228] in diameter so that only one tissue would be trapped in a cup. Therefore, the rest of the tissues in the channel will be guided into the following cup. Secondly, it is unlikely to push the trapped islets out of the cups considering the selected sizes will be significantly larger than the microspheres (45-90μm in diameter) used in the simulation.

Chapter 4

Demonstration of the microfluidic system for simultaneous monitoring of $[Ca^{2+}]_{ex}$ and insulin

This chapter demonstrates the feasibility of utilising this microfluidic sensing system for simultaneous monitoring of $[Ca^{2+}]$ and insulin. Firstly, the microfluidic system was incorporated with a LIF detection system to establish the standard curve of the fluorescent signal as a function of $[Ca^{2+}]$. Secondly, the simultaneous monitoring of $[Ca^{2+}]_{ex}$ and insulin was achieved by correlating the Ca^{2+}-induced fluorescent signals with insulin concentration determined by ELISA. The results suggested that the on-chip fluorescence measurements were stable over the long-term measurement and promising in investigating the role of $[Ca^{2+}]_{ex}$ in insulin secretion.

4.1 Background

As the aim of this sensing platform is to achieve the simultaneous monitoring of $[Ca^{2+}]_{ex}$ and insulin, quantitative method for measuring the concentration of insulin is required to be incorporated into the system. For the microfluidic devices developed for islet study, ELISA is the prevalent method for insulin quantification [151].

ELISA is a biochemical assay that utilises antibodies and the enzyme-induced colouration to measure the presence or concentration of either antigen (peptides, proteins, hormones, etc.) or antibody in biological fluids [229]. There are four major principles in ELISA protocols, i.e., direct ELISA, indirect ELISA, sandwich ELISA and competitive ELISA [230]. Generally, ELISAs work in 96-well microplates with the fluid samples isolated from the objects.

For direct ELISA, a molecule of interest, antigen in this case, in the sample is absorbed onto the surface of the assay plate via non-specific binding. Enzyme-conjugated primary antibody is then added into the system and incubated with the immobilised antigen. On the completion of the incubation, the well is washed to remove the unbound antibody. Subsequently, the enzyme substrates are added into the well, where the substrates interact with the enzyme and undergo colouration. The latter is dependent on the bound enzyme. The concentration of the antigen is further determined by measuring the optical density (OD) of the sample (Fig. 4.1a). In the indirect ELISA, the plate surface is pre-coated with antigen, which specifically reacts with the primary antibody (target molecule in this case) in the sample. The enzyme-conjugated secondary antibody is then added into the plate and binds to the primary antibody. The concentration of the primary antibody is further read out by the colouration of the substrates induced by the bound secondary antibody (Fig. 4.1b). In the sandwich ELISA, the target antigen is trapped between the primary antibody and the enzyme-conjugated secondary antibody, where a sandwich-like structure is formed (Fig. 4.1c). In the competitive ELISA, samples containing the target antigen are mixed with enzyme-tagged antigen and then added into a microplate coated with antibody. The untagged antigen (from the sample) competes with the tagged antigen to bind with the antibody (Fig. 4.1d). The unbound antigen is removed and substrates are added into the system to quantify the bound enzyme-tagged antigen. In this case, the concentration of the untagged antigen (molecule of interest in this case) has a negative correlation with the optical signal, as the more antigen in the sample, the less enzyme-conjugated antigen can bind to the antibody to induce the colouration of the substrates.

ELISA represents a reliable method for protein quantification as it is highly sensitive and selective to the molecules of interest [230]. Moreover, all the components for ELISA have been assembled into a portable kit that is ready-to-use. It allows multiple measurements (over 80 samples per kit) with low requirement on experimental facilities (only a plate reader for measuring OD). Therefore, ELISA is used in this study to quantify the insulin concentrations in the sample collected from the microfluidic system.

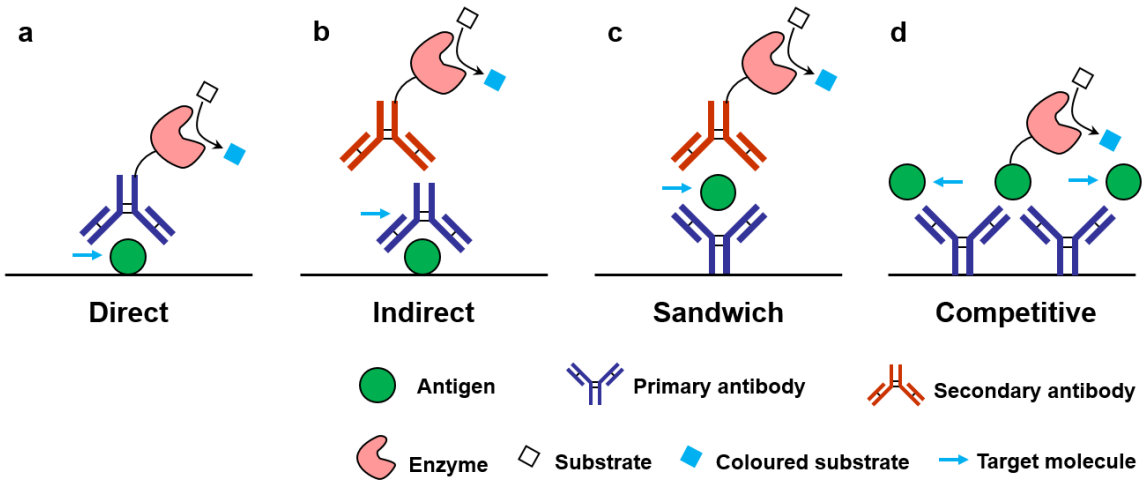

Figure 4.1 | Schematics of the four major types of ELISA. a | In the direct ELISA, the antigen is absorbed onto the plate surface via non-specific binding. The enzyme-tagged antibody is then added into the system to induce a dose-dependent colouration of the substrate. The concentration of the antigen is revealed by the degree of the colouration; **b |** In indirect ELISA, the plate surface is pre-coated with the antigen that specifically reacts with the target antibody. When the antibody in the sample binds to the antigen, the enzyme-tagged secondary antibody (orange) is added into the system. The bound enzyme induces the dose-dependent colouration of the substrate, which is further used to analyse the concentration of target antibody; **c |** In sandwich ELISA, the target antigen is trapped between the primary antibody coated on the plate surface and the enzyme-tagged secondary antibody. Therefore, they form a sandwich-like structure; **d |** In competitive ELISA, the target antigen in the sample competes with the enzyme-tagged antibody to bind to the antibody. The more antigen in the sample, the less enzyme-tagged antibody can bind to the antibody, leading to a less extent of colouration. Thus the concentration of target antigen is negatively correlated with the degree of colouration.

4.2 Methods

4.2.1 In-house built microfluidic sensing system

To measure the dynamic fluorescence intensity in the microfluidic chip, a LIF detection system was incorporated with the microfluidic perfusion system as shown in Fig. 4.2a. As Rhod-5N has been identified as the indicator to monitor the dynamic Ca^{2+} in biological samples, 532nm laser generator (MatchBox, Integrated Optics, Lithuania) was employed as the light source, which was guided by a bifurcated fibre (FG200UEA, THORLABS, USA) to the PDMS chip. The optical signal of Rhod-5N in response to [Ca^{2+}] was collected and delivered by the other branch of the fibre to the spectrometer (QEPro, Ocean Optics, UK). The tip of the bifurcated fibre underneath the PDMS chip was coupled by a focusing lens. A 532nm long-pass filter

(THORLABS, USA) was placed before the spectrometer (to remove the scattering light interference (Fig. 4.2b). As shown in Fig. 4.2c, the PDMS chip attached on a glass slide was mounted on an in-house fabricated aluminium framework as a slide holder (Fig. 4.2d) for mechanical stability. The position of the slide holder can be controlled precisely in a step-wise manner by the micro-stepper (LST-15FC60-40R-XYZ, Lambda Scientific).

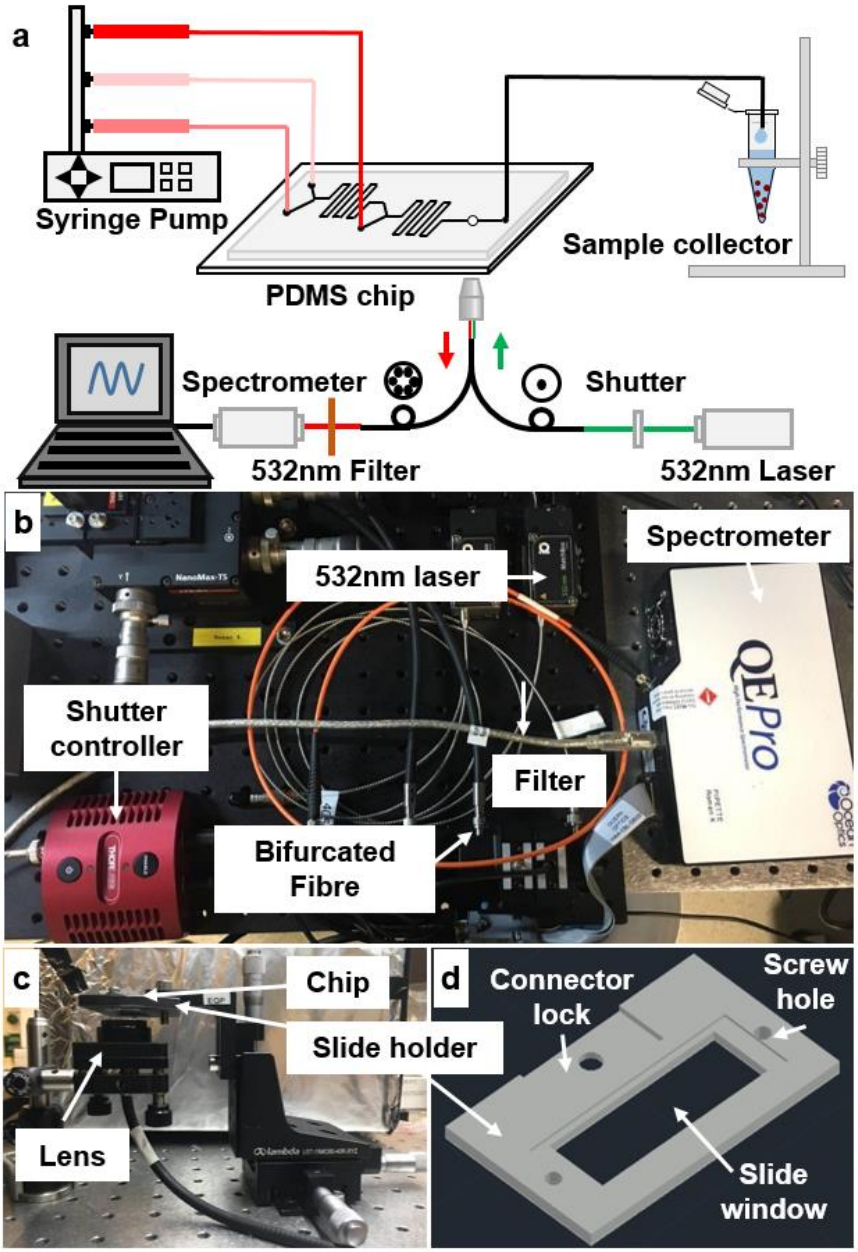

Figure 4.2 | Schematics of the in-house built microfluidic sensing system. a | The microfluidic perfusion system was incorporated laser-induced fluorescence detection system based on a bifurcated fibre; **b |** The major optical components, including laser, filter, shutter and spectrometer, were equipped on a board, enabling a portable detection system; **c |** The glass slide was connected to the position adjuster via an aluminium slide holder; **d |** The design of the slide holder for mounting the glass base of the PDMS chip.

The open and closure of shutter, as well as the detection of the spectrometer, were controlled by the LabView program developed by Dr. Erik Schartner. Briefly, once the laser beam was on, the shutter closed to block the light. When clicking at the 'read' button on the computer, the shutter opened, the laser passed through the shutter and excited the fluorescent indicator in the chip. The emitted fluorescence from the indicator was collected by the fibre and, subsequently, sent to the spectrometer for detection. The shutter closed again once a fluorescent signal was detected. The closure of shutter during the non-detection period effectively avoided the photobleaching of the indicator induced by continuous exposure.

4.2.2 Preparation of fluorescent Ca^{2+} indicator and artificial extracellular fluid

As discussed in Chapter 2, Rhod-5N has been identified for the optimal indicators to track the Ca^{2+} concentration. The 1mM stock solution of Rhod-5N was prepared by dissolving 500μg Rhod-5N powder (Thermo Fisher Scientific, USA) in 555.6μL pH7.4 PBS buffer. The stock solution was subsequently diluted into 100μM with pH7.4 PBS buffer for measuring Ca^{2+} concentration. PBS buffer was freshly prepared before preparing the Rhod-5N solutions as described in section 2.2.2 with freshly calibrated pH meter for adjusting the pH.

Dulbecco's Modified Eagle Medium (DMEM) (Thermo Fisher Scientific, USA), is a cell culture medium that is widely used in *in vitro* cell/tissue culture. To simulate the measurement of $[Ca^{2+}]_{ex}$ in a biologically relevant environment, Ca^{2+}-free cell culture medium, was used to as the base medium for preparing Ca^{2+} solution.

The 200mM Ca^{2+} stock solution was diluted into 2mM and 4mM respectively. The 4mM Ca^{2+} DMEM was subsequently 1:1 mixed with a standard insulin sample to obtain an insulin-supplemented DMEM for the simultaneous measurement of Ca^{2+} and insulin. In this experiment, the Calibrator 5, containing 200mU/L insulin, from the insulin ELISA kit (Mercodia, Sweden) was used to mix with the 4mM Ca^{2+} DMEM to prepare the insulin-supplemented cell culture medium, where the final concentrations of insulin and Ca^{2+} were 100mU/L and 2mM respectively.

4.2.3 Perfusion arrangements of the on-chip measurements

To characterise the on-chip fluorescent sensing of the system, two on-chip experiments were carried out as proof-of-concept experiments: (i) Standard curve of the fluorescence intensity as a function of [Ca^{2+}]; (ii) Demonstrate the feasibility of utilising this sensing platform for simultaneous measurements of [Ca^{2+}] and insulin.

The perfusion settings for the two experiments are shown in Fig. 4.3. Generally, two cell culture mediums containing varying concentrations of Ca^{2+} or insulin were pumped into the microfluidic chip via inlet 1 and inlet 2 respectively. While the total flow rate of inlet 1 and inlet 2 was maintained constant, the ratio of inlet 1 to inlet 2 (R_I) was switched to obtain serial concentrations of Ca^{2+} in the channel. The flow rate at inlet 3 was set the same as the total flow rate of inlet 1 and inlet 2. These sensing conditions replicated the off-chip measurements, where the Ca^{2+} solution was 1:1 mixed with the indicator solution. The detailed flow rates settings for the two experiments are described in the following two sections, respectively.

In Chapter 2, the Ca^{2+} sample was 1:1 mixed with indicator solution in a well for fluorescence measurement. The concentrations of Ca^{2+} used in the results were the final Ca^{2+} concentrations (detecting concentrations) in order to demonstrate the sensing performance of the indicator when they were dissolved in the extracellular fluid. In this chapter, Ca^{2+} concentrations in the samples (sample concentrations of Ca^{2+} before mixing with the indicator) are used in the results to demonstrate the sensing performance of the system in revealing the dynamic changes of Ca^{2+} in the effluents from the tissue array. Therefore, the concentrations of Ca^{2+} in this chapter are equivalent to twice the Ca^{2+} concentrations in Chapter 2. For example, the fluorescence of Rhod-5N induced by 0-2mM Ca^{2+} in the results of this chapter is equivalent to the fluorescence induced by 0-1mM Ca^{2+} in Chapter 2. Thus, the standard curve of fluorescence intensity in response to 0-3mM [Ca^{2+}] (sample concentration) established in the following section (4.2.4) is then further compared with the fluorescence intensity induced by 0-1.5mM Ca^{2+} (detecting concentration) in the off-chip measurements via plate reader. (The difference between sample concentration and detecting concentration can be referred to Fig. 4.3)

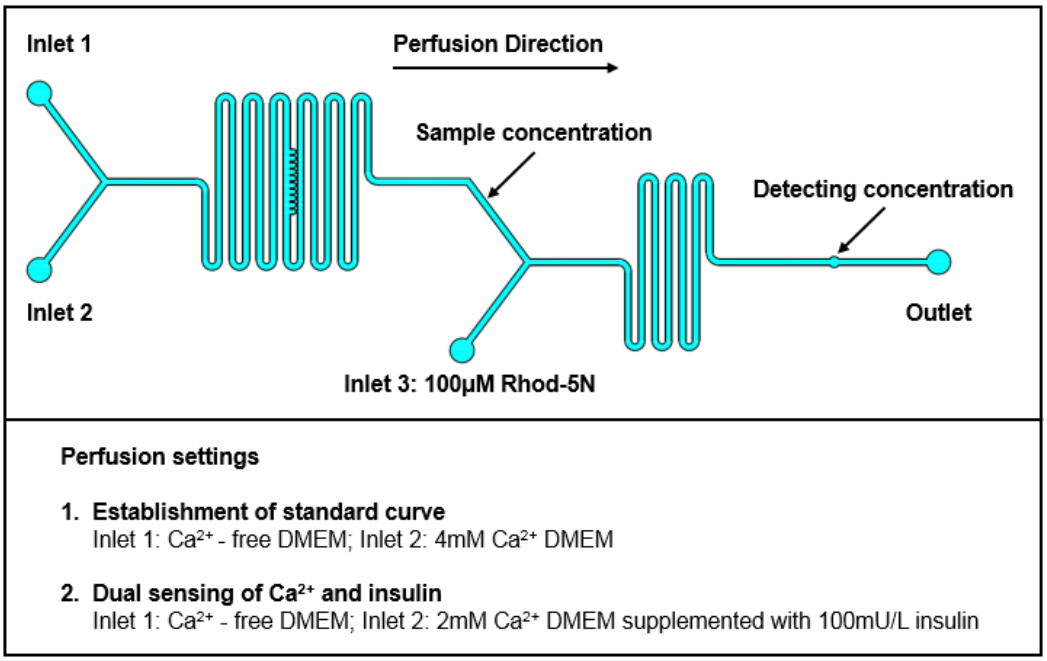

Figure 4.3 | The experimental settings for the perfusion solution in the two following experiments. Two cell culture medium containing varying concentrations of Ca^{2+} were pumped into the channel via inlet 1 and inlet 2. While the total flow rate of inlet 1 and inlet 2 were constant, the ratio of the flow rate at inlet 1 to inlet 2 was altered to obtain serial concentrations of Ca^{2+} in the channel. The Rhod-5n solution was pumped into the channel at inlet 3 at the same flow rate as the total flow rate of inlet 1 and inlet 2.

4.2.4 On-chip establishment of fluorescence standard curve as a function of [Ca^{2+}]

Considering the volume and motions, the fluorescence intensity measured from samples flowing in a microfluidic channel can dramatically vary from the fluorescence of the samples in a microplate. Thus, it was important to establish a standard curve of the fluorescence intensity of the indicator as a function of [Ca^{2+}] to characterise the on-chip fluorescence profile.

In this experiment, 4mM Ca^{2+}-supplemented DMEM was used as the Ca^{2+} fluid in order to establish a standard curve of 0-3mM Ca^{2+} in the sample, which fully encompassed the target Ca^{2+} (0-2mM) (Fig. 4.3 *bottom*, Perfusion setting 1). As shown in Table 4.1, the flow rates of inlet 1 and inlet 2 were switching between 0-4μL/min with a total flow rate of 4μL/min, which was also the flow rate at inlet 3. The flow rates used in this experiment were arbitrarily set within the flow rate range of future biological application (0-5μL/min). The fluorescence intensities at 580nm (fluorescence peak of Rhod-5N) in response to varying Ca^{2+} concentrations were recorded. Each measurement was repeated three times with an interval of 30 seconds. When adjusting the flow rate for a different [Ca^{2+}], the fluorescence was recorded only after stable signals were observed.

Table 4.1 | Flow rate setting and corresponding sample concentration of Ca^{2+}

$[Ca^{2+}]_S$ (mM)	Flow Rate (µL/min)				R_I
	Inlet 1	Inlet 2	Inlet 3	Outlet	
0	4	0	4	8	4 : 0
0.5	3.5	0.5	4	8	7 : 1
1.0	3	1	4	8	3 : 1
1.5	2.5	1.5	4	8	5 : 3
2.0	2	2	4	8	1 : 1
2.5	1.5	2.5	4	8	3 : 5
3.0	1	3	4	8	1 : 3

4.2.5 Development of a dual-sensing system for $[Ca^{2+}]_{ex}$ and insulin secretion

To simultaneously record the $[Ca^{2+}]_{ex}$ and insulin concentration, Ca^{2+}-free DMEM and 2mM Ca^{2+} DMEM supplemented with 100.5mU/L insulin were pumped into the channel via inlet 1 and inlet 2, respectively (Fig. 4.3 *bottom,* Perfusion setting 2). Prior to pump the samples, the microfluidic channel was rinsed with 0.3% bovine serum albumin (BSA) for 15 minutes to prevent the non-specific absorption of insulin by PDMS. The 0.3% BSA was prepared by dissolving 0.15g BSA (Sigma, USA) in 50g DI water in a clean Falcon tube.

In this experiment, the flow rates of inlet 1 and inlet 2 were dynamically controlled to produce oscillatory $[Ca^{2+}]$ (1.0-1.8mM, 0.5-1.5mM and 0.2-1.0mM, respectively) and oscillating insulin concentrations as detailed in Table 4.2. The experiment time of each concentration group last for 30 minutes, during which the fluorescence intensity was recorded in every 10 seconds.

In a biological experiment, homogeneous distributions of stimulatory molecules must be achieved on the tissue array in order to equally stimulate the 10 tissues in the tissue array. As a result, the applicable flow rate range is determined by the stimulus used in the experiment. Glucose is the most prevalent stimulus used in islet studies and, therefore, it was used as the reference for deciding the flow rate to be used in the following experiment. As discussed in section 3.3.5, the maximum flow rate to ensure the complete mixing of glucose was calculated to be 5µL/min (total flow rate of inlet 1 and inlet 2) in the current system. Therefore, 5µL/min was used as the flow rate to characterise the sensing performance of this system. Under this condition, the characterised fluorescence profile for Ca^{2+} would serve as a good indicator to improve the chip design for biological applications in the future.

The detailed flow rate of each inlet and corresponding concentrations of Ca^{2+} and insulin are shown in Table 4.2. To measure the insulin via ELISA, a 1.5mL Eppendorf tube was placed under the tube, which was connected to the outlet (Fig. 4.2a). It is worth noting that a volume of 25μL is required for each sample. Considering the flow rate was 10μL/min at the outlet, the collecting time for each sample was 3 minutes to ensure a sufficient sample for the measurement. Therefore, the Eppendorf tube was replaced every three minutes.

Table 4.2 | Flow rate settings and corresponding sample concentrations of Ca^{2+} and insulin

$[Ca^{2+}]_S$ (mM)	Insulin (mU/L)	Flow Rate (μL/min)				R_I
		Inlet 1	Inlet 2	Inlet 3	Outlet	
0.2	10	4.5	0.5	5	10	9 : 1
0.5	25	3.75	1.25	5	10	3 : 1
1	50	2.5	2.5	5	10	1 : 1
1.5	75	1.25	3.75	5	10	1 : 3
1.8	90	0.5	4.5	5	10	1 : 9

4.2.6 Quantification of insulin by direct sandwich ELISA

The concentration of insulin was measured by an insulin ELISA kit (Mercodia, Sweden). The procedure is based on the direct sandwich technique, where two anti-insulin antibodies that bind to two separate antigenic sites on the insulin molecule. The experiment steps followed the protocol of the ELISA kit. Briefly, the effluents collected from the outlet of the chip every three minutes were used as the samples for the off-chip insulin quantification. In the 96-well microplate from the ELISA kit, the surface of each well was coated with anti-insulin antibody (primary antibody). Calibrators (standard samples with known concentrations of insulin), samples and peroxidase-conjugated anti-insulin antibodies (enzyme-conjugated secondary antibody) were successively added into the plate. The plate was then incubated for an hour to allow the binding between insulin and antibody, followed by a washing step to remove the unbound secondary antibody. To indicate the concentration of bound enzyme in the sample, 3, 3', 5, 5'-tetramethylbenzidine (TMD) (substrate) was added into the wells, where TMD reacted with the enzyme and the system turned from colourless to blue. A stop solution was added into the well to terminate the reaction to give a colourimetric endpoint. Subsequently, the absorbance of the samples was read at 450nm to calculate the concentration of insulin in the samples based on the standard curve of the calibrators.

4.3 Results

4.3.1 Standard curve of on-chip fluorescence intensity as a function of [Ca^{2+}]

To compare the off-chip measurements with on-chip results, the standard fluorescence curve in the microfluidic chip was plotted against the [Ca^{2+}] together with the fluorescence measured in a microplate.

As shown in Fig. 4.4, the profile of Rhod-5N in the microfluidic chip displayed a similar pattern in response to 0-2mM Ca^{2+} as the off-chip measurements, where significant fluorescence enhancements were observed in response to increasing [Ca^{2+}] from 0-3mM. Consistent with the off-chip measurements, the on-chip fluorescent profile also well fitted in the 'Hill fit' analysis, which reflected the monomer binding between Rhod-5N and Ca^{2+}. In addition, the minor standard deviations of the repeated on-chip measurements suggested a complete mixing and stable binding between Ca^{2+} and Rhod-5N at the optical window. The fluorescence curves show that the increase of off-chip fluorescence responding to 0.5-3mM Ca^{2+} was smaller than the increase of on-chip fluorescence. This tendency to saturation of the off-chip results may attribute to the fact that the Ca^{2+}-induced fluorescence intensity of Rhod-5N was reaching the upper detection limit of the plate reader.

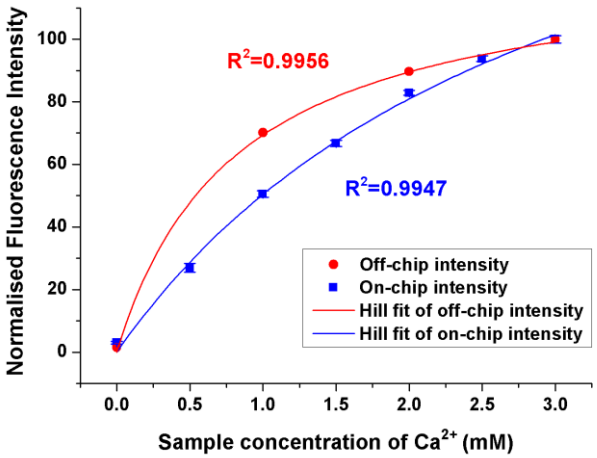

Figure 4.4 | Comparison of on-chip (blue) and off-chip (red) fluorescence intensity of Rhod-5N as a function of Ca^{2+} concentration in the samples. The errors of the repeated measurement are significantly lower than the fluorescent signals, suggesting the highly stable flow rate over time and fluorescent sensing capability.

4.3.2 Oscillatory insulin concentrations in the artificial extracellular fluid

Insulin concentrations in the effluents collected from the outlet (experiment 2) were measured by ELISA. As shown in Fig. 4.5a, OD values of the calibrators were plotted against the insulin concentration in the calibrators as the standard curve. The linear fit equation of the standard curve was then used to translate the OD values into corresponding concentrations of insulin in the effluent. As the concentration of insulin in the effluents represented the detecting concentration (indicated in Fig. 4.3), sample concentrations of the three groups were obtained by doubling the detecting concentration and shown in Fig. 4.5b.

Oscillatory patterns of insulin concentration were recorded in the two groups with higher concentrations of insulin, 50-90mU/L and 25-75mU/L groups. However, the pattern was diminished in the lowest concentration group, where the insulin concentration should theoretically fluctuate between 10 and 50mU/L (Fig. 4.5b). Compared with the theoretical concentration (Fig. 4.5b, legend), the experimental results of the three groups were less than half of the concentration in theory. Therefore, the loss of the pattern could be caused by the non-specific absorption of the PDMS or the degradation of insulin over the long experiment periods.

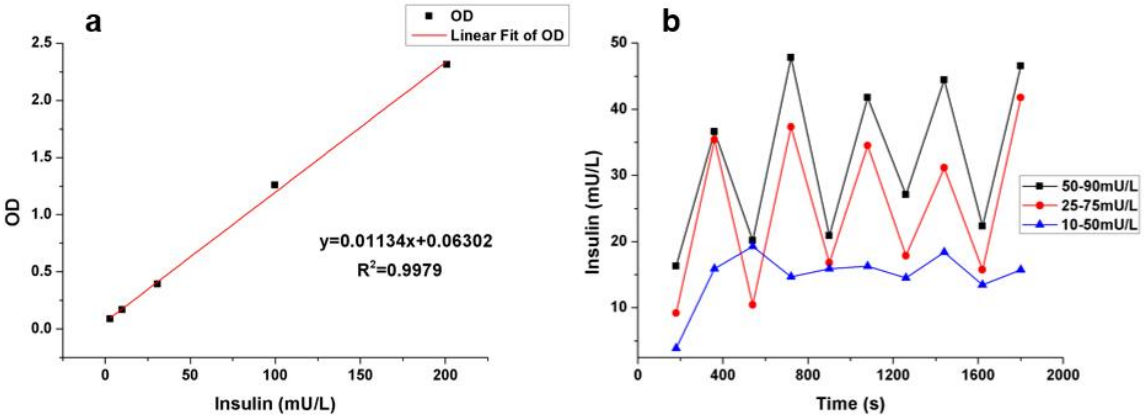

Figure 4.5 | Quantification of sample concentrations of insulin collected from the outlet every 3 minutes. a | Standard curve drawn with the OD and concentrations of the calibrators; **b** | Calculated sample concentrations of insulin in the three experimental groups.

4.3.3 Development of a dual-sensing system for simultaneous monitoring of $[Ca^{2+}]_{ex}$ and insulin

To demonstrate the dual-sensing capability of the system, the results of insulin quantification were integrated with the dynamic fluorescent signal recorded concurrently. As shown in Fig. 4.6, the oscillatory patterns observed in insulin (Fig. 4.6, red) concentration synchronised with the dynamic fluorescence intensity (Fig. 4.6, blue) revealing the oscillating concentrations of Ca^{2+} (Fig. 4.6 *top* and *middle*). It was clear that one period of Ca^{2+} oscillation lasts around 500-600s and the time required for the transition between two concentrations of Ca^{2+} is around 90s. When comparing the Ca^{2+}-induced fluorescence and signal of insulin, a time delay of around 70-100s was observed between the Ca^{2+} oscillation and corresponding insulin concentration.

The time delay between the patterns of the two molecules reflected the time for the sample to travel from the optical window to the Eppendorf tube and also for the operations to change the flow rates. This time delay could be validated by calculating the volume (V) for the sample to travel through from the optical window to falcon tube. The distance from the optical window to the outlet (L_c) was 4000μm. Considering the channel width (300μm) and the height (250μm), the volume on-chip (V_c) was calculated as:

$$V_c = w \times h \times L$$

$$V_c = 300 \times 250 \times 4000\ [\mu m^3] = 0.3 \mu L$$

As the length (L_t) and internal radius (r_i) of the circular tube were 20cm and 0.25mm respectively, the volume in the tube (V_t) was expressed as:

$$V_t = \pi r_i^{\,2} L_t$$

$$V_t = \pi \times 125^2 \times 200000 [\mu m^3] \approx 9.81\ \mu L$$

The time (t_s) for the sample to travel from the optical window to the falcon tube was:

$$t_s = \frac{V_c + V_t}{Q} = \frac{0.3 + 9.81\ [\mu L]}{10\ [\mu L/min]} = 60.675 s$$

Therefore, the time delay observed between the insulin concentration and Ca^{2+}-induced fluorescence resulted from the travelling time together with the operation time on adjusting the flow rate (10-20s).

In terms of signal strength, the highest fluorescent signal (around 60% of the maximum fluorescence) was observed as Ca^{2+} was oscillating between 0.2-1.0mM (Fig. 4.6 *bottom*). The corresponding signals were 40% and 20% in the 0.5-1.5mM group (Fig. 4.6 *middle*) and 1.0-1.8mM group (Fig. 4.6 *top*), respectively. By continuously refreshing the indicator solution, the fluorescent signal in the microfluidic chip was free from drifting or photobleaching throughout the experiment period.

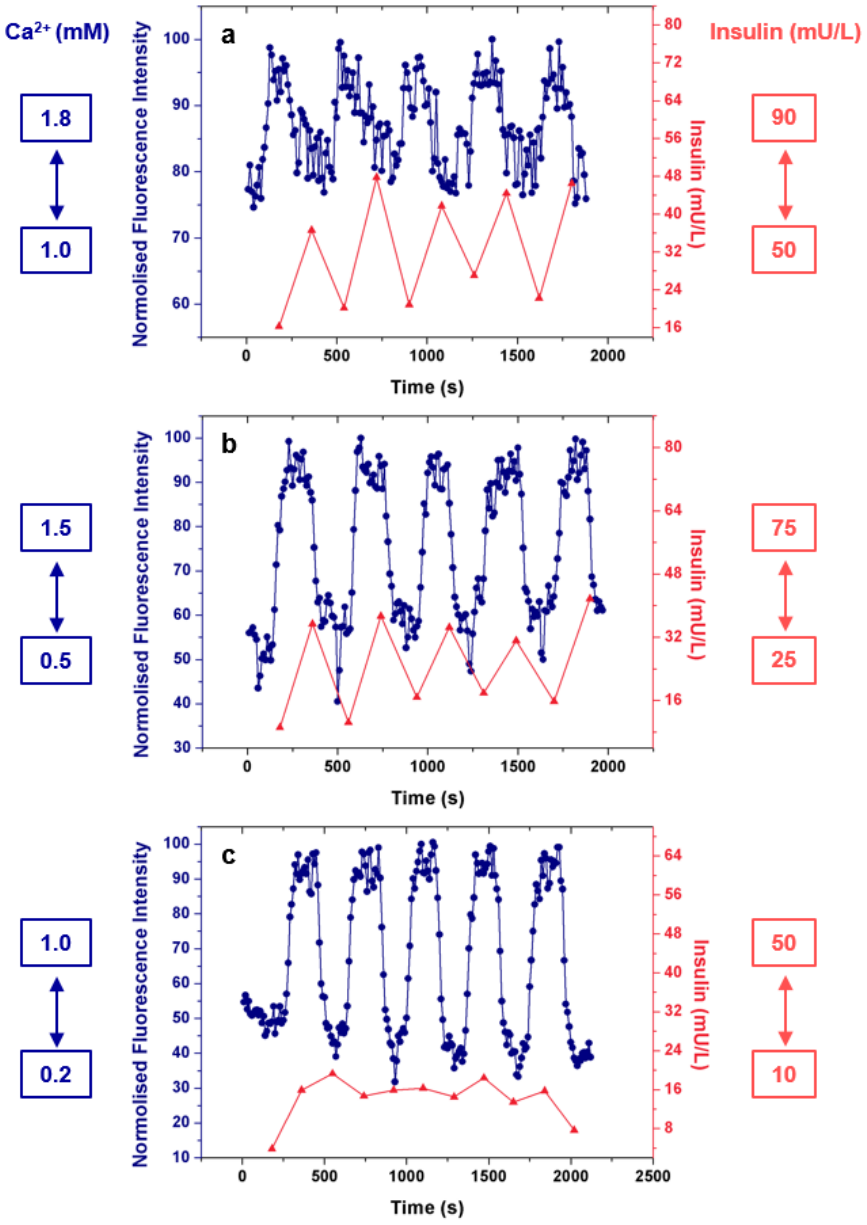

Figure 4.6 | Simultaneous monitoring of Ca^{2+} and Insulin in biological samples via fluorescent sensing (blue) and ELISA (red). Both the [Ca^{2+}] and insulin concentration were oscillating in the artificial extracellular fluid as indicated beside each panel.

4.4 Discussion

This chapter demonstrated the feasibility of utilising the sensing system for simultaneous monitoring of $[Ca^{2+}]_{ex}$ and insulin concentration in biological samples. The system, for the first time, successfully recorded the oscillatory $[Ca^{2+}]$ and insulin in an artificial extracellular environment based on cell culture medium. It was shown that the current temporal resolutions were 10 seconds on sensing Ca^{2+} and 3 minutes on quantifying insulin. While the system displayed a promising performance as a dual-sensing system, further improvements of the system should include reducing the loss of insulin, the automation of the procedure, mixing efficiency and temporal resolution.

Firstly, the absorption of insulin by PDMS should be properly addressed so that minor fluctuation of insulin would be captured by the system. The blocking treatment conducted in this study was achieved by rinsed the channel with 0.3% BSA for 10 minutes. Strategies to enhance the exposure of the channel to BSA are likely to reduce the loss of insulin, such as increasing the concentration of BSA, continuously perfusing the channel with BSA solution instead of static treatment.

Secondly, higher automation in flow rate control and sampling are in great demand to reduce the repeated operations, particularly in a long-term experiment. The establishment of the on-chip standard curve of the fluorescence intensity as a function of $[Ca^{2+}]$ indicated the stability of the system, including the input control and fluorescence detection, over a relatively long experiment period (more than one hour). However, the laborious operations on flow rate adjustment and sample collection justified the necessity to introduce programs or devices that could enhance the degree of the automation of the system. For example, a pre-set flow rate schedule that spontaneously modifies the flow rates at a certain time point or an automated sample collector that automatically replaces the sample tube on the completion of a given sampling period. Moreover, manual operations significantly increased the time required for stabilising the signal. Therefore, improvement in the automation of the system will enhance the temporal resolution of the detection as well as the accuracy of the results.

Last and most importantly, as the goal of developing this microfluidic sensing system was to investigate the role of $[Ca^{2+}]_{ex}$ in the pulsatile insulin secretion, the temporal resolution of the system is expected to be higher than the periods of insulin pulsatility under physiological conditions (4-6 minutes [22]). As the temporal resolution was faster than the periods of pulsatile

insulin secretion, the general insulin pulsatility would be recorded with the current sensing capability. However, it may fail to genuinely reveal the occurrence of fast oscillations which oscillate at a shorter period (~4 minutes).

Therefore, the temporal resolution of the platform should be optimised further. One solution is to enhance the mixing efficiency of the microfluidic chip so that higher flow rates can be applied on the system, allowing to collect the sample for insulin detection within a shorter period of time. As a result, the interval between each measurement would be reduced, leading to a higher temporal resolution on insulin quantification. Passive mixers, such as herringbones structure [231], are promising candidates to be embedded into the microfluidic channel as they effectively enhance the mixing efficiency without the assistance of external device [232].

Alternatively, on-chip insulin quantification via capillary electrophoresis immunoassay (CEI) is also a reliable technique to be incorporated into the system [160,165,178,233]. Similar to the competitive ELISA, on-chip CEI is based on competitive binding between insulin in the samples and fluorescein isothiocyanate-labelled insulin (FITC-insulin) to the anti-insulin antibody (Ab). In a microfluidic chip, the effluent from a pancreatic islet, Ab and FITC-insulin are individually pumped into a reaction channel, where insulin in the effluent and FITC-insulin competitively bind to Ab. The reacted mixture is then injected into an electrophoresis channel, where the bound and unbound FITC-insulin are separated due to their different velocity in the electric field (unbound FITC-insulin would be faster as they are lighter). Since the ratio of bound to unbound FITC-insulin is dependent on the concentration of insulin from the islet, the insulin secretion can be quantified by comparing the fluorescence of bound and unbound FITC-insulin as they successively pass through the detection point. By integrating the on-chip CEI, a real-time dual-sensing system can be achieved with temporal resolutions of tens of seconds on both $[Ca^{2+}]_{ex}$ and insulin secretion. However, as CEI demands another independent LIF detection system, which significantly complicates the experimental setup. Further evaluation is required before deciding which strategy to be adopted.

Chapter 5

Conclusions & Perspectives

The work detailed in this thesis relates to the development of a novel microfluidic sensing platform capable of simultaneous monitoring of extracellular Ca^{2+} and insulin, which will enable thorough investigation on the role of Ca^{2+} in insulin secretion from the endocrine pancreas.

As described in Chapter 1, Ca^{2+} is involved in a complex intracellular and extracellular signalling pathways responsible for insulin secretion from the pancreatic islets, which plays a central role in maintaining blood glucose homeostasis in health. The disrupted insulin secretion, characterised as both impaired responsiveness of the pancreatic beta-cells to glucose stimulation and the pulsative secretory pattern, has featured early pathophysiology of T2DM, one of the most devastating chronic diseases in the modern society. The current understanding relating to the dynamic $[Ca^{2+}]$ and the physiology of insulin secretion has been facilitated by the development of novel Ca^{2+} sensors. In particular, the role of intracellular Ca^{2+} signalling has been clarified using synthetic fluorescent indicators. However, the mechanism of extracellular Ca^{2+} signalling pathway is poorly defined due to the lack of sensing method suitable for measurement of both dynamic $[Ca^{2+}]_{ex}$ and insulin secretion from the pancreatic islets. Therefore, the fundamental aim of the work in this thesis was to overcome this barrier by developing a novel microfluidic sensing system that is capable of sensing $[Ca^{2+}]_{ex}$ and insulin secretion from tissues simultaneously.

In Chapter 2, quantitative methods for determining $[Ca^{2+}]_{ex}$ were established based on commercially available fluorescent indicators, Calcein and Rhod-5N [63,74]. Although previous studies suggested that these two fluorescent indicators might be suitable candidates, systematic evaluations relating to their performance in sensing $[Ca^{2+}]_{ex}$, including the fluorescent profile, selectivity and compatibility with the biological system, have not been reported. The two

methods presented in this work exhibited comparable or even superior capabilities to those recently developed methods for measuring $[Ca^{2+}]_{ex}$ [179-181]. Furthermore, the environment-dependent selectivity of Calcein and the effect of Zn^{2+} and Cu^{2+} on Rhod-5N justified the necessity to investigate the interference from the other metal ions in the proposed working environment. As a conclusion of this chapter, Rhod-5N was more suitable for tracking dynamic $[Ca^{2+}]_{ex}$ considering its higher signal to background ratio and the compatibility with the biological environment.

In Chapter 3, a microfluidic chip was designed, fabricated and characterised for correlating the dynamic $[Ca^{2+}]_{ex}$ with the function of the tissue. The current measurement for $[Ca^{2+}]_{ex}$ relies on the CSM [129], which intrinsically reflects the dynamic $[Ca^{2+}]_{ex}$ in proximity to a single cell. Considering the broad roles of $[Ca^{2+}]_{ex}$ in multi-cellular level, the applicability of ISM is limited when correlating $[Ca^{2+}]_{ex}$ and the tissue function, such as the secretion of insulin from the pancreatic islets. With the microfluidic described in this work, tissue culture, dynamic stimulation and functional analysis were performed with one experiment set up. The continuous extraction of extracellular fluid would allow simultaneous examination of $[Ca^{2+}]_{ex}$ and insulin secretion in the effluent. Due to the limited mixing efficiency, the maximum on-chip flow rate is relatively smaller compared with other chip devices for secretion analysis, where the on-chip flow rate ranges from tens to a hundred microliter per minute [234]. Therefore, future work should consider the incorporation of the efficient fluid mixer, such as the herringbones structure, to enhance a higher mixing efficiency and, therefore, allow a higher flow rate in the microfluidic channel [231]. A novel, but logical extension from the islet study, the development of different tissue trapping structures may enable evaluation of the endocrine function of tissues other than islets.

Hitherto, the microfluidic device developed for islet study have been focusing on the dynamic intracellular Ca^{2+} and insulin secretion [150,151]. In Chapter 4, a series of "proof-of-concept" experiments have shown the competency of the microfluidic sensing platform as a dual-sensing system for simultaneous monitoring of $[Ca^{2+}]_{ex}$ and insulin in biological samples. The development of this novel sensing platform is likely to substantially advance the understanding of the mechanisms underlying insulin secretion, although several limitations, including the time delay between the signals for $[Ca^{2+}]$ and insulin, temporal resolution for insulin quantification and the potential diffusion of insulin out of the flow, remain to be optimised.

In summary, this thesis has established a novel sensing platform capable of concurrent monitoring of $[Ca^{2+}]_{ex}$ and insulin, which has the potential to advance the understanding of the (patho-)physiology of the pancreatic islets. The possibility of functionalising the microfluidic system into a multiplexed sensor renders the customised applications of the system for a variety of biological research in the future. For example, fluorescent indicators can be introduced into cells of the tissue to track the dynamics of intracellular biomarkers so that the correlation between the intracellular and the extracellular signalling would be established. Moreover, multi-targets measurements can be achieved by the simultaneous loading of fluorescent indicators with different emission wavelengths via inlet 3.

Reference

1 Organization, W. H. *Global report on diabetes*. (World Health Organization, 2016).

2 Seuring, T., Archangelidi, O. & Suhrcke, M. The economic costs of type 2 diabetes: a global systematic review. *Pharmacoeconomics* **33**, 811-831 (2015).

3 Rorsman, P. & Braun, M. Regulation of insulin secretion in human pancreatic islets. *Annual review of physiology* **75**, 155-179 (2013).

4 Newsholme, P., Cruzat, V., Arfuso, F. & Keane, K. Nutrient regulation of insulin secretion and action. *Journal of Endocrinology* **221**, R105-R120 (2014).

5 Fu, Z., R Gilbert, E. & Liu, D. Regulation of insulin synthesis and secretion and pancreatic Beta-cell dysfunction in diabetes. *Current diabetes reviews* **9**, 25-53 (2013).

6 Bertram, R., Sherman, A. & Satin, L. S. Electrical, Calcium, and Metabolic Oscillations in Pancreatic Islets. *Islets of Langerhans, 2. ed.*, 1-20 (2013).

7 Colella, M., Gerbino, A., Hofer, A. M. & Curci, S. Recent advances in understanding the extracellular calcium-sensing receptor. *F1000Research* **5** (2016).

8 Squires, P. E., Jones, P. M., Younis, M. Y. & Hills, C. E. in *Vitamins & Hormones* Vol. 95 249-267 (Elsevier, 2014).

9 Townsend, C. M., Beauchamp, R. D., Evers, B. M. & Mattox, K. L. *Sabiston Textbook of Surgery E-Book*. (Elsevier Health Sciences, 2016).

10 Cabrera, O. *et al.* The unique cytoarchitecture of human pancreatic islets has implications for islet cell function. *Proceedings of the National Academy of Sciences of the United States of America* **103**, 2334-2339 (2006).

11 Caicedo, A. in *Seminars in cell & developmental biology.* 11-21 (Elsevier).

12 Chou, H.-F. & Ipp, E. Pulsatile insulin secretion in isolated rat islets. *Diabetes* **39**, 112-117 (1990).

13 Hellman, B. *et al.* Glucose induces oscillatory Ca2+ signalling and insulin release in human pancreatic beta cells. *Diabetologia* **37**, S11-S20, doi:10.1007/BF00400821 (1994).

14 Anderson, G. E., Kologlu, Y. & Papadopoulos, C. Fluctuations in postabsorptive blood glucose in relation to insulin release. *Metabolism* **16**, 586-596 (1967).

15 Lang, D., Matthews, D., Peto, J. & Turner, R. Cyclic oscillations of basal plasma glucose and insulin concentrations in human beings. *The New England journal of medicine* **301**, 1023-1027 (1979).

16 Goodner, C. J., Hom, F. G. & Koerker, D. J. Hepatic glucose production oscillates in synchrony with the islet secretory cycle in fasting rhesus monkeys. *Science* **215**, 1257-1260 (1982).

17 Matthews, D. *et al.* Greater in vivo than in vitro pulsatility of insulin secretion with synchronized insulin and somatostatin secretory pulses. *Endocrinology* **120**, 2272-2278 (1987).

18 Hansen, B. C. *et al.* Neural influences on oscillations in basal plasma levels of insulin in monkeys. *American Journal of Physiology-Endocrinology And Metabolism* **240**, E5-E11 (1981).

19 Chou, H.-F., McGivern, R., Berman, N. & Ipp, E. Oscillations of circulating plasma insulin concentrations in the rat. *Life sciences* **48**, 1463-1469 (1991).

20 Pørksen, N., Munn, S., Steers, J., Veldhuis, J. D. & Butler, P. C. Effects of glucose ingestion versus infusion on pulsatile insulin secretion: the incretin effect is achieved by amplification of insulin secretory burst mass. *Diabetes* **45**, 1317-1323 (1996).

21 Porksen, N., Munn, S., Steers, J., Veldhuis, J. D. & Butler, P. C. Impact of sampling technique on appraisal of pulsatile insulin secretion by deconvolution and cluster analysis. *American Journal of Physiology-Endocrinology And Metabolism* **269**, E1106-E1114 (1995).

22 Pørksen, N. The in vivo regulation of pulsatile insulin secretion. *Diabetologia* **45**, 3-20 (2002).
23 Gumbiner, B. *et al.* Abnormalities of insulin pulsatility and glucose oscillations during meals in obese noninsulin-dependent diabetic patients: effects of weight reduction. *The Journal of Clinical Endocrinology & Metabolism* **81**, 2061-2068 (1996).
24 O'Rahilly, S., Turner, R. C. & Matthews, D. R. Impaired pulsatile secretion of insulin in relatives of patients with non-insulin-dependent diabetes. *New England Journal of Medicine* **318**, 1225-1230 (1988).
25 Lin, J.-M., Fabregat, M. E., Gomis, R. & Bergsten, P. Pulsatile insulin release from islets isolated from three subjects with type 2 diabetes. *Diabetes* **51**, 988-993 (2002).
26 Rutter, G. A. & Hodson, D. J. Minireview: intraislet regulation of insulin secretion in humans. *Molecular endocrinology* **27**, 1984-1995 (2013).
27 Ashcroft, F. M., Harrison, D. E. & Ashcroft, S. J. Glucose induces closure of single potassium channels in isolated rat pancreatic β-cells. *Nature* **312**, 446-448 (1984).
28 Cook, D. L. & Hales, N. Intracellular ATP directly blocks K+ channels in pancreatic B-cells. *Nature* **311**, 271-273 (1984).
29 Henquin, J., Nenquin, M., Ravier, M. & Szollosi, A. Shortcomings of current models of glucose‐induced insulin secretion. *Diabetes, Obesity and Metabolism* **11**, 168-179 (2009).
30 Gilon, P., Chae, H.-Y., Rutter, G. A. & Ravier, M. A. Calcium signaling in pancreatic β-cells in health and in Type 2 diabetes. *Cell Calcium* **56**, 340-361, doi:https://doi.org/10.1016/j.ceca.2014.09.001 (2014).
31 Yang, S.-N. & Berggren, P.-O. The role of voltage-gated calcium channels in pancreatic β-cell physiology and pathophysiology. *Endocrine reviews* **27**, 621-676 (2006).
32 Jahn, R. & Fasshauer, D. Molecular machines governing exocytosis of synaptic vesicles. *Nature* **490**, 201-207 (2012).
33 Henquin, J.-C., Dufrane, D., Kerr-Conte, J. & Nenquin, M. Dynamics of glucose-induced insulin secretion in normal human islets. *American Journal of Physiology-Endocrinology and Metabolism* **309**, E640-E650 (2015).
34 Godsland, I., Jeffs, J. & Johnston, D. Loss of beta cell function as fasting glucose increases in the non-diabetic range. *Diabetologia* **47**, 1157-1166 (2004).
35 Tengholm, A. & Gylfe, E. Oscillatory control of insulin secretion. *Molecular and cellular endocrinology* **297**, 58-72 (2009).
36 Martin, F. & Soria, B. Glucoseminduced [Ca2+] i oscillations in single human pancreatic islets. *Cell calcium* **20**, 409-414 (1996).
37 Bergsten, P., Grapengiesser, E., Gylfe, E., Tengholm, A. & Hellman, B. Synchronous oscillations of cytoplasmic Ca2+ and insulin release in glucose-stimulated pancreatic islets. *Journal of Biological Chemistry* **269**, 8749-8753 (1994).
38 Hellman, B. *et al.* Glucose induces oscillatory Ca 2+ signalling and insulin release in human pancreatic beta cells. *Diabetologia* **37**, S11-S20 (1994).
39 Bergsten, P. Slow and fast oscillations of cytoplasmic Ca2+ in pancreatic islets correspond to pulsatile insulin release. *American Journal of Physiology - Endocrinology And Metabolism* **268**, E282-E287 (1995).
40 Jonas, J.-C., Gilon, P. & Henquin, J.-C. Temporal and quantitative correlations between insulin secretion and stably elevated or oscillatory cytoplasmic Ca2+ in mouse pancreatic β-cells. *Diabetes* **47**, 1266-1273 (1998).
41 Henquin, J.-C. Regulation of insulin secretion: a matter of phase control and amplitude modulation. *Diabetologia* **52**, 739 (2009).
42 AINSCOW, E. K. & RUTTER, G. A. Mitochondrial priming modifies Ca2+ oscillations and insulin secretion in pancreatic islets. *Biochemical Journal* **353**, 175-180, doi:10.1042/bj3530175 (2001).

43 Waldeck-Weiermair, M. *et al.* Spatiotemporal correlations between cytosolic and mitochondrial Ca2+ signals using a novel red-shifted mitochondrial targeted cameleon. *PloS one* **7**, e45917 (2012).
44 Tarasov, A. I. *et al.* The mitochondrial Ca2+ uniporter MCU is essential for glucose-induced ATP increases in pancreatic β-cells. *PloS one* **7**, e39722 (2012).
45 Gilon, P., Arredouani, A., Gailly, P., Gromada, J. & Henquin, J.-C. Uptake and release of Ca2+ by the endoplasmic reticulum contribute to the oscillations of the cytosolic Ca2+ concentration triggered by Ca2+ influx in the electrically excitable pancreatic B-cell. *Journal of Biological Chemistry* **274**, 20197-20205 (1999).
46 Arredouani, A., Henquin, J.-C. & Gilon, P. Contribution of the endoplasmic reticulum to the glucose-induced [Ca 2+] c response in mouse pancreatic islets. *American Journal of Physiology-Endocrinology and Metabolism* **282**, E982-E991 (2002).
47 Pendin, D., Greotti, E. & Pozzan, T. The elusive importance of being a mitochondrial Ca 2+ uniporter. *Cell calcium* **55**, 139-145 (2014).
48 Kindmark, H. *et al.* Glucose-induced oscillations in cytoplasmic free Ca2+ concentration precede oscillations in mitochondrial membrane potential in the pancreatic β-cell. *Journal of Biological Chemistry* **276**, 34530-34536 (2001).
49 Krippeit-Drews, P., Düfer, M. & Drews, G. Parallel oscillations of intracellular calcium activity and mitochondrial membrane potential in mouse pancreatic B-cells. *Biochemical and biophysical research communications* **267**, 179-183 (2000).
50 MacDonald, M. J. *et al.* Citrate oscillates in liver and pancreatic beta cell mitochondria and in INS-1 insulinoma cells. *Journal of Biological Chemistry* **278**, 51894-51900 (2003).
51 CIVELEK, V. N. *et al.* Regulation of pancreatic β-cell mitochondrial metabolism: influence of Ca2+, substrate and ADP. *Biochemical Journal* **318**, 615-621 (1996).
52 Tarasov, A. I. *et al.* Frequency-dependent mitochondrial Ca2+ accumulation regulates ATP synthesis in pancreatic β cells. *Pflügers Archiv - European Journal of Physiology* **465**, 543-554, doi:10.1007/s00424-012-1177-9 (2013).
53 Wiederkehr, A. *et al.* Mitochondrial matrix calcium is an activating signal for hormone secretion. *Cell metabolism* **13**, 601-611 (2011).
54 Ainscow, E. K. & Rutter, G. A. Glucose-stimulated oscillations in free cytosolic ATP concentration imaged in single islet β-cells. *Diabetes* **51**, S162-S170 (2002).
55 Tarasov, A. I. *et al.* Frequency-dependent mitochondrial Ca2+ accumulation regulates ATP synthesis in pancreatic β cells. *Pflügers Archiv-European Journal of Physiology* **465**, 543-554 (2013).
56 Ravier, M. A. *et al.* Mechanisms of Control of the Free Ca2+ Concentration in the Endoplasmic Reticulum of Mouse Pancreatic β-Cells. *Diabetes* **60**, 2533-2545 (2011).
57 Vangheluwe, P. *et al.* Intracellular Ca2+-and Mn2+-transport ATPases. *Chemical reviews* **109**, 4733-4759 (2009).
58 Arredouani, A. *et al.* SERCA3 ablation does not impair insulin secretion but suggests distinct roles of different sarcoendoplasmic reticulum Ca2+ pumps for Ca2+ homeostasis in pancreatic β-cells. *Diabetes* **51**, 3245-3253 (2002).
59 Rocheleau, J. V. *et al.* Critical role of gap junction coupled K ATP channel activity for regulated insulin secretion. *PLoS Biol* **4**, e26 (2006).
60 Calabrese, A. *et al.* Connexin 36 controls synchronization of Ca2+ oscillations and insulin secretion in MIN6 cells. *Diabetes* **52**, 417-424 (2003).
61 Charpantier, E., Cancela, J. & Meda, P. Beta cells preferentially exchange cationic molecules via connexin 36 gap junction channels. *Diabetologia* **50**, 2332-2341 (2007).
62 Gylfe, E. & Tengholm, A. Neurotransmitter control of islet hormone pulsatility. *Diabetes, Obesity and Metabolism* **16**, 102-110 (2014).
63 Zhang, C., Miller, C. L., Brown, E. M. & Yang, J. J. The calcium sensing receptor: from calcium sensing to signaling. *Science China Life Sciences* **58**, 14-27 (2015).

64 Brown, E. M. *et al.* Cloning and characterization of an extracellular Ca2+-sensing receptor from bovine parathyroid. *Nature* **366**, 575-580 (1993).
65 Hofer, A. M., Curci, S., Doble, M. A., Brown, E. M. & Soybel, D. I. Intercellular communication mediated by the extracellular calcium-sensing receptor. *Nature Cell Biology* **2**, 392 (2000).
66 De Luisi, A. & Hofer, A. M. Evidence that Ca2+ cycling by the plasma membrane Ca2+-ATPase increases theexcitability'of the extracellular Ca2+-sensing receptor. *Journal of cell science* **116**, 1527-1538 (2003).
67 Gerbino, A. *et al.* Glucose increases extracellular [Ca 2+] in rat insulinoma (INS-1E) pseudoislets as measured with Ca 2+-sensitive microelectrodes. *Cell calcium* **51**, 393-401 (2012).
68 Squires, P. E. *et al.* The extracellular calcium-sensing receptor on human beta-cells negatively modulates insulin secretion. *Diabetes* **49**, 409-417, doi:10.2337/diabetes.49.3.409 (2000).
69 Gray, E. *et al.* Activation of the extracellular calcium-sensing receptor initiates insulin secretion from human islets of Langerhans: involvement of protein kinases. *Journal of Endocrinology* **190**, 703-710 (2006).
70 Hills, C. E. *et al.* Calcium-Sensing Receptor Activation Increases Cell-Cell Adhesion and β-Cell Function. *Cellular Physiology and Biochemistry* **30**, 575-586 (2012).
71 Rasschaert, J. & Malaisse, W. J. Expression of the calcium-sensing receptor in pancreatic islet B-cells. *Biochemical and biophysical research communications* **264**, 615-618 (1999).
72 Squires, P. E., Hauge-Evans, A. C., Persaud, S. J. & Jones, P. M. Synchronization of Ca2+-signals within insulin-secreting pseudoislets: effects of gap-junctional uncouplers. *Cell Calcium* **27**, 287-296, doi:http://dx.doi.org/10.1054/ceca.2000.0117 (2000).
73 Squires, P. E., Jones, P. M., Younis, M. Y. & Hills, C. E. The Calcium-Sensing Receptor and b-Cell Function. *The Pancreatic Beta Cell* **95**, 249 (2014).
74 Breitwieser, G. E. Extracellular calcium as an integrator of tissue function. *The international journal of biochemistry & cell biology* **40**, 1467-1480 (2008).
75 Milner, R. D. & Hales, C. The role of calcium and magnesium in insulin secretion from rabbit pancreas studied in vitro. *Diabetologia* **3**, 47-49 (1967).
76 Ridgway, E. B. & Ashley, C. C. Calcium transients in single muscle fibers. *Biochemical and biophysical research communications* **29**, 229-234 (1967).
77 Valeur, B. & Berberan-Santos, M. N. *Molecular fluorescence: principles and applications*. (John Wiley & Sons, 2012).
78 Carter, K. P., Young, A. M. & Palmer, A. E. Fluorescent sensors for measuring metal ions in living systems. *Chemical reviews* **114**, 4564-4601 (2014).
79 Spence, M. T. & Johnson, I. D. *The molecular probes handbook: a guide to fluorescent probes and labeling technologies*. (Live Technologies Corporation, 2010).
80 Rorsman, P., Abrahamsson, H., Gylfe, E. & Hellman, B. Dual effects of glucose on the cytosolic Ca2+ activity of mouse pancreatic β - cells. *FEBS letters* **170**, 196-200 (1984).
81 Rorsman, P., Berggren, P.-O., Gylfe, E. & Hellman, B. Reduction of the cytosolic calcium activity in clonal insulin-releasing cells exposed to glucose. *Bioscience reports* **3**, 939-946 (1983).
82 Liu, Y. J., Tengholm, A., Grapengiesser, E., Hellman, B. & Gylfe, E. Origin of slow and fast oscillations of Ca2+ in mouse pancreatic islets. *The Journal of physiology* **508**, 471-481 (1998).
83 Nunemaker, C. S. *et al.* Glucose modulates [Ca 2+] i oscillations in pancreatic islets via ionic and glycolytic mechanisms. *Biophysical journal* **91**, 2082-2096 (2006).
84 Zhang, M., Goforth, P., Bertram, R., Sherman, A. & Satin, L. The Ca 2+ dynamics of isolated mouse β-cells and islets: implications for mathematical models. *Biophysical journal* **84**, 2852-2870 (2003).
85 Kindmark, H. *et al.* Oscillations in cytoplasmic free calcium concentration in human pancreatic islets from subjects with normal and impaired glucose tolerance. *Diabetologia* **37**, 1121-1131 (1994).

86 Valdeolmillos, M., Santos, R. M., Contreras, D., Soria, B. & Rosario, L. M. Glucose-induced oscillations of intracellular Ca2+ concentration resembling bursting electrical activity in single mouse islets of Langerhans. *FEBS letters* **259**, 19-23 (1989).
87 Beauvois, M. C. *et al.* Glucose-induced mixed [Ca2+] c oscillations in mouse β-cells are controlled by the membrane potential and the SERCA3 Ca2+-ATPase of the endoplasmic reticulum. *American Journal of Physiology-Cell Physiology* **290**, C1503-C1511 (2006).
88 Arredouani, A. *et al.* SERCA3 Ablation Does Not Impair Insulin Secretion but Suggests Distinct Roles of Different Sarcoendoplasmic Reticulum Ca²⁺ Pumps for Ca²⁺ Homeostasis in Pancreatic β-cells. *Diabetes* **51**, 3245-3253 (2002).
89 Quesada, I. *et al.* Glucose Induces Opposite Intracellular Ca²⁺ Concentration Oscillatory Patterns in Identified α- and β-Cells Within Intact Human Islets of Langerhans. *Diabetes* **55**, 2463-2469, doi:10.2337/db06-0272 (2006).
90 Luciani, D. S., Misler, S. & Polonsky, K. S. Ca2+ controls slow NAD (P) H oscillations in glucose‐stimulated mouse pancreatic islets. *The Journal of physiology* **572**, 379-392 (2006).
91 Li, J., Shuai, H. Y., Gylfe, E. & Tengholm, A. Oscillations of sub-membrane ATP in glucose-stimulated beta cells depend on negative feedback from Ca2+. *Diabetologia* **56**, 1577-1586, doi:10.1007/s00125-013-2894-0 (2013).
92 Dyachok, O. *et al.* Glucose-induced cyclic AMP oscillations regulate pulsatile insulin secretion. *Cell metabolism* **8**, 26-37 (2008).
93 Miyazaki, J.-I. *et al.* Establishment of a pancreatic β cell line that retains glucose-inducible insulin secretion: special reference to expression of glucose transporter isoforms. *Endocrinology* **127**, 126-132 (1990).
94 Takahashi, A., Camacho, P., Lechleiter, J. D. & Herman, B. Measurement of intracellular calcium. *Physiological reviews* **79**, 1089-1125 (1999).
95 Simpson, A. W. Fluorescent measurement of [Ca 2+] c: basic practical considerations. *Calcium Signaling Protocols*, 3-36 (2013).
96 Vázquez, M. E., Blanco, J. B. & Imperiali, B. Photophysics and biological applications of the environment-sensitive fluorophore 6-N, N-dimethylamino-2, 3-naphthalimide. *Journal of the American Chemical Society* **127**, 1300-1306 (2005).
97 Demchenko, A. P. *Introduction to fluorescence sensing*. (Springer Science & Business Media, 2008).
98 Li, J., Shuai, H., Gylfe, E. & Tengholm, A. Oscillations of sub-membrane ATP in glucose-stimulated beta cells depend on negative feedback from Ca2+. *Diabetologia* **56**, 1577-1586 (2013).
99 Idevall-Hagren, O., Barg, S., Gylfe, E. & Tengholm, A. cAMP mediators of pulsatile insulin secretion from glucose-stimulated single β-cells. *Journal of Biological Chemistry* **285**, 23007-23018 (2010).
100 Thomas, D. *et al.* A comparison of fluorescent Ca2+ indicator properties and their use in measuring elementary and global Ca2+ signals. *Cell calcium* **28**, 213-223 (2000).
101 Bassnett, S., Reinisch, L. & Beebe, D. C. Intracellular pH measurement using single excitation-dual emission fluorescence ratios. *American Journal of Physiology-Cell Physiology* **258**, C171-C178 (1990).
102 Ashley, C. & Ridgway, E. Simultaneous recording of membrane potential, calcium transient and tension in single muscle fibres. *Nature* **219**, 1168-1169 (1968).
103 Llinas, R. & Nicholson, C. Calcium role in depolarization-secretion coupling: an aequorin study in squid giant synapse. *Proceedings of the National Academy of Sciences* **72**, 187-190 (1975).
104 Stinnakre, J. & Tauc, L. Calcium influx in active Aplysia neurones detected by injected aequorin. *Nature* **242**, 113-115 (1973).
105 Rizzuto, R., Simpson, A. W., Brini, M. & Pozzan, T. Rapid changes of mitochondrial Ca2+ revealed by specifically targeted recombinant aequorin. *Nature* **358**, 325-327 (1992).

106 Heim, R. & Tsien, R. Y. Engineering green fluorescent protein for improved brightness, longer wavelengths and fluorescence resonance energy transfer. *Current biology* **6**, 178-182 (1996).
107 McCombs, J. E. & Palmer, A. E. Measuring calcium dynamics in living cells with genetically encodable calcium indicators. *Methods* **46**, 152-159 (2008).
108 Koldenkova, V. P. & Nagai, T. Genetically encoded Ca 2+ indicators: Properties and evaluation. *Biochimica et Biophysica Acta (BBA)-Molecular Cell Research* **1833**, 1787-1797 (2013).
109 Mank, M. & Griesbeck, O. Genetically encoded calcium indicators. *Chemical reviews* **108**, 1550-1564 (2008).
110 Ohmiya, Y. & Hirano, T. Shining the light: the mechanism of the bioluminescence reaction of calcium-binding photoproteins. *Chemistry & biology* **3**, 337-347 (1996).
111 Rudolf, R., Mongillo, M., Rizzuto, R. & Pozzan, T. Looking forward to seeing calcium. *Nature Reviews Molecular Cell Biology* **4**, 579-586 (2003).
112 Miyawaki, A. *et al.* Fluorescent indicators for Ca2+based on green fluorescent proteins and calmodulin. *Nature* **388**, 882-887 (1997).
113 Baubet, V. *et al.* Chimeric green fluorescent protein-aequorin as bioluminescent Ca2+ reporters at the single-cell level. *Proceedings of the National Academy of Sciences* **97**, 7260-7265 (2000).
114 Rogers, K. L. *et al.* Visualization of local Ca2+ dynamics with genetically encoded bioluminescent reporters. *European Journal of Neuroscience* **21**, 597-610 (2005).
115 Bakayan, A., Vaquero, C. F., Picazo, F. & Llopis, J. Red fluorescent protein-aequorin fusions as improved bioluminescent Ca2+ reporters in single cells and mice. *PloS one* **6**, e19520 (2011).
116 Miyata, H. *et al.* Measurement of mitochondrial free Ca2+ concentration in living single rat cardiac myocytes. *American Journal of Physiology-Heart and Circulatory Physiology* **261**, H1123-H1134 (1991).
117 Hajnóczky, G., Robb-Gaspers, L. D., Seitz, M. B. & Thomas, A. P. Decoding of cytosolic calcium oscillations in the mitochondria. *Cell* **82**, 415-424 (1995).
118 Hofer, A. M. & Machen, T. E. Technique for in situ measurement of calcium in intracellular inositol 1, 4, 5-trisphosphate-sensitive stores using the fluorescent indicator mag-fura-2. *Proceedings of the National Academy of Sciences* **90**, 2598-2602 (1993).
119 Nakazaki, M. *et al.* Repetitive mitochondrial Ca2+ signals synchronize with cytosolic Ca2+ oscillations in the pancreatic beta-cell line, MIN6. *Diabetologia* **41**, 279-286 (1998).
120 Ottolini, D., Calì, T. & Brini, M. in *Methods in enzymology* Vol. 543 21-45 (Elsevier, 2014).
121 Palmer, A. E., Qin, Y., Park, J. G. & McCombs, J. E. Design and application of genetically encoded biosensors. *Trends in Biotechnology* **29**, 144-152, doi:https://doi.org/10.1016/j.tibtech.2010.12.004 (2011).
122 Haslett, C. Granulocyte apoptosis and its role in the resolution and control of lung inflammation. *American journal of respiratory and critical care medicine* **160**, S5-S11 (1999).
123 Rutter, G. A. *et al.* Stimulated Ca2+ influx raises mitochondrial free Ca2+ to supramicromolar levels in a pancreatic beta-cell line. Possible role in glucose and agonist-induced insulin secretion. *Journal of Biological Chemistry* **268**, 22385-22390 (1993).
124 Nagai, T., Sawano, A., Park, E. S. & Miyawaki, A. Circularly permuted green fluorescent proteins engineered to sense Ca2+. *Proceedings of the National Academy of Sciences* **98**, 3197-3202 (2001).
125 Miyawaki, A., Llopis, J., Heim, R. & McCaffery, J. M. Fluorescent indicators for Ca2+ based on green fluorescent proteins and calmodulin. *Nature* **388**, 882 (1997).
126 Varadi, A. & Rutter, G. A. Dynamic imaging of endoplasmic reticulum Ca2+ concentration in insulin-secreting MIN6 cells using recombinant targeted cameleons. *Diabetes* **51**, S190-S201 (2002).
127 Palmer, A. E. *et al.* Ca 2+ indicators based on computationally redesigned calmodulin-peptide pairs. *Chemistry & biology* **13**, 521-530 (2006).

128 Ammann, D. *Ion-selective microelectrodes: principles, design and application*. Vol. 50 (Springer Science & Business Media, 2013).
129 Luxardi, G., Reid, B., Ferreira, F., Maillard, P. & Zhao, M. Measurement of Extracellular Ion Fluxes Using the Ion-selective Self-referencing Microelectrode Technique. *Journal of visualized experiments: JoVE* (2015).
130 Whitaker, M. *Calcium in living cells*. Vol. 99 (Academic Press, 2010).
131 Haack, N., Durry, S., Kafitz, K. W., Chesler, M. & Rose, C. R. Double-barreled and concentric microelectrodes for measurement of extracellular ion signals in brain tissue. *Journal of visualized experiments: JoVE* (2015).
132 Young, W., Yen, V. & Blight, A. Extracellular calcium ionic activity in experimental spinal cord contusion. *Brain research* **253**, 105-113 (1982).
133 Silver, I., Murrills, R. & Etherington, D. Microelectrode studies on the acid microenvironment beneath adherent macrophages and osteoclasts. *Experimental cell research* **175**, 266-276 (1988).
134 Bers, D. M. Early transient depletion of extracellular Ca during individual cardiac muscle contractions. *American Journal of Physiology-Heart and Circulatory Physiology* **244**, H462-H468 (1983).
135 Caroppo, R. *et al.* Asymmetrical, agonist‐induced fluctuations in local extracellular [Ca²⁺] in intact polarized epithelia. *The EMBO Journal* **20**, 6316-6326, doi:10.1093/emboj/20.22.6316 (2001).
136 Perez-Armendariz, E. & Atwater, I. in *Biophysics of the Pancreatic β-Cell* 31-51 (Springer, 1986).
137 Moura, A. Membrane potential and intercellular calcium during glucose challenge in mouse islet of Langerhans. *Biochemical and biophysical research communications* **214**, 798-802 (1995).
138 Gerbino, A. *et al.* Glucose increases extracellular [Ca2+] in rat insulinoma (INS-1E) pseudoislets as measured with Ca2+-sensitive microelectrodes. *Cell Calcium* **51**, 393-401, doi:http://dx.doi.org/10.1016/j.ceca.2012.01.002 (2012).
139 Schaafsma, G. in *Calcium in human biology* 241-259 (Springer, 1988).
140 Dresdner, K. P. & Kline, R. P. Extracellular calcium ion depletion in frog cardiac ventricular muscle. *Biophysical journal* **48**, 33-45 (1985).
141 Howl, J., Von Sicard, N., Publicover, S. & Anderson, M. A method for the manufacture of single barrel liquid ion-selective microelectrodes: an in situ study of ant venom pH. *Pflügers Archiv* **411**, 212-215 (1988).
142 Grapengiesser, E., Gylfe, E. & Hellman, B. Glucose-induced oscillations of cytoplasmic Ca2+ in the pancreatic β-cell. *Biochemical and Biophysical Research Communications* **151**, 1299-1304, doi:http://dx.doi.org/10.1016/S0006-291X(88)80503-5 (1988).
143 Misler, S. *et al.* Electrical activity and exocytotic correlates of biphasic insulin secretion from β-cells of canine islets of Langerhans: Contribution of tuning two modes of Ca2+ entry-dependent exocytosis to two modes of glucose-induced electrical activity. *Channels* **3**, 181-193 (2009).
144 Kendall, J. M., Dormer, R. L. & Campbell, A. K. Targeting aequorin to the endoplasmic reticulum of living cells. *Biochemical and biophysical research communications* **189**, 1008-1016 (1992).
145 Brini, M. *et al.* Transfected aequorin in the measurement of cytosolic Ca2+ concentration ([Ca2+] c) A critical evaluation. *Journal of Biological Chemistry* **270**, 9896-9903 (1995).
146 Palmer, A. E. & Tsien, R. Y. Measuring calcium signaling using genetically targetable fluorescent indicators. *Nature protocols* **1**, 1057-1065 (2006).
147 Schefer, U., Ammann, D., Pretsch, E., Oesch, U. & Simon, W. Neutral carrier based calcium (2+)-selective electrode with detection limit in the sub-nanomolar range. *Analytical chemistry* **58**, 2282-2285 (1986).

148 Suzuki, K. *et al.* Design and synthesis of calcium and magnesium ionophores based on double-armed diazacrown ether compounds and their application to an ion sensing component for an ion-selective electrode. *Analytical Chemistry* **67**, 324-334 (1995).
149 Perestrelo, A. R., Águas, A. C., Rainer, A. & Forte, G. Microfluidic organ/body-on-a-chip devices at the convergence of biology and microengineering. *Sensors* **15**, 31142-31170 (2015).
150 Schrell, A. M., Mukhitov, N., Yi, L., Wang, X. & Roper, M. G. Microfluidic Devices for the Measurement of Cellular Secretion. *Annual Review of Analytical Chemistry* **9**, 249-269 (2016).
151 Castiello, F. R., Heileman, K. & Tabrizian, M. Microfluidic perfusion systems for secretion fingerprint analysis of pancreatic islets: applications, challenges and opportunities. *Lab on a Chip* **16**, 409-431 (2016).
152 Luni, C., Serena, E. & Elvassore, N. Human-on-chip for therapy development and fundamental science. *Current opinion in biotechnology* **25**, 45-50 (2014).
153 Adewola, A. F. *et al.* Microfluidic perifusion and imaging device for multi-parametric islet function assessment. *Biomedical microdevices* **12**, 409-417 (2010).
154 Nourmohammadzadeh, M. *et al.* Microfluidic array with integrated oxygenation control for real-time live-cell imaging: effect of hypoxia on physiology of microencapsulated pancreatic islets. *Analytical chemistry* **85**, 11240-11249 (2013).
155 Lo, J. F. *et al.* Islet preconditioning via multimodal microfluidic modulation of intermittent hypoxia. *Analytical chemistry* **84**, 1987-1993 (2012).
156 Dhumpa, R., Truong, T. M., Wang, X. & Roper, M. G. Measurement of the entrainment window of islets of Langerhans by microfluidic delivery of a chirped glucose waveform. *Integrative Biology* **7**, 1061-1067 (2015).
157 Dhumpa, R., Truong, T. M., Wang, X., Bertram, R. & Roper, M. G. Negative feedback synchronizes islets of Langerhans. *Biophysical Journal* **106**, 2275-2282 (2014).
158 Zhang, X., Grimley, A., Bertram, R. & Roper, M. G. Microfluidic system for generation of sinusoidal glucose waveforms for entrainment of islets of Langerhans. *Analytical chemistry* **82**, 6704-6711 (2010).
159 Shackman, J. G., Dahlgren, G. M., Peters, J. L. & Kennedy, R. T. Perfusion and chemical monitoring of living cells on a microfluidic chip. *Lab on a Chip* **5**, 56-63 (2005).
160 Yi, L., Bandak, B., Wang, X., Bertram, R. & Roper, M. G. Dual Detection System for Simultaneous Measurement of Intracellular Fluorescent Markers and Cellular Secretion. *Analytical chemistry* **88**, 10368-10373 (2016).
161 Silva, P. N. *et al.* Highly efficient adenoviral transduction of pancreatic islets using a microfluidic device. *Lab on a Chip* **16**, 2921-2934 (2016).
162 Nourmohammadzadeh, M. *et al.* A microfluidic array for real-time live-cell imaging of human and rodent pancreatic islets. *Lab on a Chip* **16**, 1466-1472 (2016).
163 Schulze, T. *et al.* A 3D microfluidic perfusion system made from glass for multiparametric analysis of stimulus-secretion coupling in pancreatic islets. *Biomedical Microdevices* **19**, 47 (2017).
164 Sankar, K. S. *et al.* Culturing pancreatic islets in microfluidic flow enhances morphology of the associated endothelial cells. *PLoS One* **6**, e24904 (2011).
165 Yi, L. *et al.* Integrated perfusion and separation systems for entrainment of insulin secretion from islets of Langerhans. *Lab on a Chip* **15**, 823-832 (2015).
166 Lomasney, A. R., Yi, L. & Roper, M. G. Simultaneous monitoring of insulin and islet amyloid polypeptide secretion from islets of Langerhans on a microfluidic device. *Analytical chemistry* **85**, 7919-7925 (2013).
167 Roper, M. G., Shackman, J. G., Dahlgren, G. M. & Kennedy, R. T. Microfluidic chip for continuous monitoring of hormone secretion from live cells using an electrophoresis-based immunoassay. *Analytical chemistry* **75**, 4711-4717 (2003).
168 Rocheleau, J. V., Walker, G. M., Head, W. S., McGuinness, O. P. & Piston, D. W. Microfluidic glucose stimulation reveals limited coordination of intracellular Ca2+ activity oscillations in

pancreatic islets. *Proceedings of the National Academy of Sciences of the United States of America* **101**, 12899-12903 (2004).
169 Dishinger, J. F. & Kennedy, R. T. Serial immunoassays in parallel on a microfluidic chip for monitoring hormone secretion from living cells. *Analytical chemistry* **79**, 947-954 (2007).
170 Dishinger, J. F., Reid, K. R. & Kennedy, R. T. Quantitative monitoring of insulin secretion from single islets of Langerhans in parallel on a microfluidic chip. *Analytical chemistry* **81**, 3119-3127 (2009).
171 Reid, K. R. & Kennedy, R. T. Continuous operation of microfabricated electrophoresis devices for 24 hours and application to chemical monitoring of living cells. *Analytical chemistry* **81**, 6837-6842 (2009).
172 Shackman, J. G., Reid, K. R., Dugan, C. E. & Kennedy, R. T. Dynamic monitoring of glucagon secretion from living cells on a microfluidic chip. *Analytical and bioanalytical chemistry* **402**, 2797-2803 (2012).
173 Godwin, L. A. *et al.* Passively operated microfluidic device for stimulation and secretion sampling of single pancreatic islets. *Analytical chemistry* **83**, 7166-7172 (2011).
174 Lee, D. *et al.* Dual microfluidic perifusion networks for concurrent islet perifusion and optical imaging. *Biomedical Microdevices* **14**, 7-16 (2012).
175 Araci, I. E. & Brisk, P. Recent developments in microfluidic large scale integration. *Current opinion in biotechnology* **25**, 60-68 (2014).
176 Wang, Y. *et al.* Application of microfluidic technology to pancreatic islet research: first decade of endeavor. *Bioanalysis* **2**, 1729-1744 (2010).
177 Xing, Y. *et al.* A pumpless microfluidic device driven by surface tension for pancreatic islet analysis. *Biomedical Microdevices* **18**, 80 (2016).
178 Wang, X., Yi, L. & Roper, M. G. Microfluidic device for the measurement of amino acid secretion dynamics from murine and human islets of Langerhans. *Analytical chemistry* **88**, 3369-3375 (2016).
179 He, H., Jenkins, K. & Lin, C. A fluorescent chemosensor for calcium with excellent storage stability in water. *analytica chimica acta* **611**, 197-204 (2008).
180 Sui, B., Liu, X., Wang, M. & Belfield, K. D. A Highly Selective Fluorescence Turn‐On Sensor for Extracellular Calcium Ion Detection. *Chemistry-A European Journal* **22**, 10351-10354 (2016).
181 Ishiwari, F. *et al.* Bioinspired design of a polymer gel sensor for the realization of extracellular Ca2+ imaging. *Scientific reports* **6** (2016).
182 Irving, H. & da Silva, J. J. R. F. 69. The stabilities of complexes of thallium(I) and the alkali metals with uramildiacetic acid. *Journal of the Chemical Society (Resumed)*, 448-457, doi:10.1039/JR9630000448 (1963).
183 Takesako, K., Sasamoto, K., Ohkura, Y., Hirose, K. & Iino, M. Low-affinity fluorescent indicator for intracellular calcium ions. *Analytical Communications* **34**, 391-392 (1997).
184 Zhan, R., Pan, Y., Manghnani, P. N. & Liu, B. AIE Polymers: Synthesis, Properties, and Biological Applications. *Macromolecular bioscience* (2016).
185 Morishima, K., Ishiwari, F., Matsumura, S., Fukushima, T. & Shibayama, M. Mesoscopic Structural Aspects of Ca2+-Triggered Polymer Chain Folding of a Tetraphenylethene-Appended Poly (acrylic acid) in Relation to Its Aggregation-Induced Emission Behavior. *Macromolecules* (2017).
186 Diehl, H. & Ellingboe, J. L. Indicator for Titration of Calcium in Presence of Magnesium Using Disodium Dihydrogen Ethylenediamine Tetraacetate. *Analytical Chemistry* **28**, 882-884, doi:10.1021/ac60113a030 (1956).
187 Bandrowski, J. F. & Benson, C. L. Investigation of the use of calcein in the ultramicro fluorometric determination of calcium in serum. *Clinical chemistry* **18**, 1411-1414 (1972).
188 Kepner, B. L. & Hercules, D. M. Fluorometric determination of calcium in blood serum. *Analytical Chemistry* **35**, 1238-1240 (1963).

189 Bett, I. M. & Fraser, G. A rapid micromethod for determining serum calcium. *Clinica chimica acta* **4**, 346-356 (1959).
190 Furry, J. W. Preparation, properties and applications of Calcein in a highly pure form. (1985).
191 Hefley, A. J. & Jaselskis, B. Fluorometric Determination of Submicrogram Quantities of Cadmium By Reaction with the Metallofluorochromic Reagent, Calcein. *Analytical Chemistry* **46**, 2036-2038, doi:10.1021/ac60349a035 (1974).
192 Wilkins, D. H. Calcein Blue—a new metalfluorechromic indicator for chelatometric titrations. *Talanta* **4**, 182-184 (1960).
193 Nivens, D. A., Zhang, Y. & Angel, S. M. Detection of uranyl ion via fluorescence quenching and photochemical oxidation of calcein. *Journal of Photochemistry and Photobiology A: Chemistry* **152**, 167-173 (2002).
194 Chang, L., Wu, T. & Chen, F. Determination of L-cysteine base on the reversion of fluorescence quenching of calcein by copper (II) ion. *Microchimica Acta* **177**, 295-300 (2012).
195 Ali, A., Zhang, Q., Dai, J. & Huang, X. Calcein as a fluorescent iron chemosensor for the determination of low molecular weight iron in biological fluids. *Biometals* **16**, 285-293 (2003).
196 Berregi, I., Durand, J. S. & Casado, J. A. Simultaneous spectrofluorimetric determination of the rare earths with calcein. *Talanta* **48**, 719-728 (1999).
197 Rusakov, D. & Fine, A. Extracellular Ca2+ depletion contributes to fast activity-dependent modulation of synaptic transmission in the brain. *Neuron* **37**, 287-297 (2003).
198 David, G., Talbot, J. & Barrett, E. F. Quantitative estimate of mitochondrial [Ca2+] in stimulated motor nerve terminals. *Cell calcium* **33**, 197-206 (2003).
199 de la Fuente, S., Fonteriz, R. I., Montero, M. & Alvarez, J. Dynamics of mitochondrial [Ca2+] measured with the low-Ca2+-affinity dye rhod-5N. *Cell calcium* **51**, 65-71 (2012).
200 Ribou, A.-C., Salmon, J.-M., Vigo, J. & Goyet, C. Measurements of calcium with a fluorescent probe Rhod-5N: Influence of high ionic strength and pH. *Talanta* **71**, 437-442 (2007).
201 Rusakov, D. & Fine, A. Extracellular Ca 2+ depletion contributes to fast activity-dependent modulation of synaptic transmission in the brain. *Neuron* **37**, 287-297 (2003).
202 Lakowicz, J. R. *Principles of fluorescence spectroscopy*. (Third edition. New York ; Berlin : Springer, [2006] ©2006, 2006).
203 Davies, C. W. & Shedlovsky, T. Ion association. *Journal of The Electrochemical Society* **111**, 85C-86C (1964).
204 Malmberg, C. & Maryott, A. Dielectric constant of water from 00 to 1000 C. *Journal of research of the National Bureau of Standards* **56**, 1-8 (1956).
205 McGuigan, J. A. S., Kay, J. W. & Elder, H. Y. Ionised concentrations in calcium and magnesium buffers: Standards and precise measurement are mandatory. *Progress in Biophysics and Molecular Biology* **126**, 48-64, doi:https://doi.org/10.1016/j.pbiomolbio.2017.03.001 (2017).
206 Gesztelyi, R. *et al.* The Hill equation and the origin of quantitative pharmacology. *Archive for history of exact sciences* **66**, 427-438 (2012).
207 Lakowicz, J. R. in *Fluorescence Studies on Biological Membranes* 89-126 (Springer, 1988).
208 Andersson, A., Danielsson, J., Gräslund, A. & Mäler, L. Kinetic models for peptide-induced leakage from vesicles and cells. *European Biophysics Journal* **36**, 621-635 (2007).
209 Hashemi, M., Ghavami, S., Eshraghi, M., Booy, E. P. & Los, M. Cytotoxic effects of intra and extracellular zinc chelation on human breast cancer cells. *European journal of pharmacology* **557**, 9-19 (2007).
210 Cai, L., Li, X.-K., Song, Y. & Cherian, M. G. Essentiality, toxicology and chelation therapy of zinc and copper. *Current medicinal chemistry* **12**, 2753-2763 (2005).
211 Sackmann, E. K., Fulton, A. L. & Beebe, D. J. The present and future role of microfluidics in biomedical research. *Nature* **507**, 181 (2014).
212 Beebe, D. J., Mensing, G. A. & Walker, G. M. Physics and applications of microfluidics in biology. *Annual review of biomedical engineering* **4**, 261-286 (2002).

213 Ferry, M. S., Razinkov, I. A. & Hasty, J. Microfluidics for synthetic biology: from design to execution. *Methods in enzymology* **497**, 295-372 (2011).
214 Fay, J. A. *Introduction to fluid mechanics*. (MIT press, 1994).
215 Cengel, Y. A. *Fluid mechanics*. (Tata McGraw-Hill Education, 2010).
216 Munson, B. R., Okiishi, T. H., Huebsch, W. W. & Rothmayer, A. P. *Fluid mechanics*. (Wiley Singapore, 2013).
217 Tabeling, P. *Introduction to microfluidics*. (Oxford University Press on Demand, 2005).
218 Weibel, D. B., DiLuzio, W. R. & Whitesides, G. M. Microfabrication meets microbiology. *Nature Reviews Microbiology* **5**, 209 (2007).
219 Xia, Y. & Whitesides, G. M. Soft lithography. *Angewandte Chemie International Edition* **37**, 550-575 (1998).
220 Tong, Z. *et al.* Crossed flow microfluidics for high throughput screening of bioactive chemical–cell interactions. *Lab on a Chip* **17**, 501-510 (2017).
221 Kotova, S., Follink, B., Del Castillo, L. & Priest, C. Leaching gold by reactive flow of ammonium thiosulfate solution in high aspect ratio channels: Rate, passivation, and profile. *Hydrometallurgy* **169**, 207-212 (2017).
222 Haynes, W. M. *CRC handbook of chemistry and physics*. (CRC press, 2014).
223 Samson, E., Marchand, J. & Snyder, K. A. Calculation of ionic diffusion coefficients on the basis of migration test results. *Materials and structures* **36**, 156-165 (2003).
224 Sober, H. A. *CRC Handbook of Biochemistry: Selected data for molecular biology*. (1973).
225 Gendron, P. O., Avaltroni, F. & Wilkinson, K. J. Diffusion Coefficients of Several Rhodamine Derivatives as Determined by Pulsed Field Gradient–Nuclear Magnetic Resonance and Fluorescence Correlation Spectroscopy. *Journal of Fluorescence* **18**, 1093, doi:10.1007/s10895-008-0357-7 (2008).
226 Clark, J., Kaufman, M. & Fodor, P. S. Mixing Enhancement in Serpentine Micromixers with a Non-Rectangular Cross-Section. *Micromachines* **9**, 107 (2018).
227 Park, C.-s., Joo, K.-I., Kang, S.-W. & Kim, H.-R. A PDMS-coated optical fiber Bragg grating sensor for enhancing temperature sensitivity. *Journal of the Optical Society of Korea* **15**, 329-334 (2011).
228 Kim, A. *et al.* Islet architecture: A comparative study. *Islets* **1**, 129-136 (2009).
229 Lequin, R. M. Enzyme immunoassay (EIA)/enzyme-linked immunosorbent assay (ELISA). *Clinical chemistry* **51**, 2415-2418 (2005).
230 Aydin, S. A short history, principles, and types of ELISA, and our laboratory experience with peptide/protein analyses using ELISA. *Peptides* **72**, 4-15 (2015).
231 Stroock, A. D. *et al.* Chaotic mixer for microchannels. *Science* **295**, 647-651 (2002).
232 Lee, C.-Y., Chang, C.-L., Wang, Y.-N. & Fu, L.-M. Microfluidic mixing: a review. *International journal of molecular sciences* **12**, 3263-3287 (2011).
233 Bandak, B., Yi, L. & Roper, M. G. Microfluidic-enabled quantitative measurements of insulin release dynamics from single islets of Langerhans in response to 5-palmitic acid hydroxy stearic acid. *Lab on a Chip* **18**, 2873-2882 (2018).
234 Silva, P. N., Green, B. J., Altamentova, S. M. & Rocheleau, J. V. A microfluidic device designed to induce media flow throughout pancreatic islets while limiting shear-induced damage. *Lab on a Chip* **13**, 4374-4384 (2013).